


Mechanical energy harvesters with tensile efficiency of 17.4% and torsional efficiency of 22.4% based on homochirally plied carbon nanotube yarns

Received: 7 July 2022

Accepted: 15 December 2022

Published online: 26 January 2023

 Check for updates

Mengmeng Zhang^{1,7}, Wenting Cai^{1,2,7}, Zhong Wang¹, Shaoli Fang¹, Runyu Zhang³, Hongbing Lu³, Ali E. Aliev⁴, Anvar A. Zakhidov¹, Chi Huynh⁴, Enlai Gao⁵, Jiyoung Oh¹, Ji Hwan Moon⁶, Jong Woo Park⁶, Seon Jeong Kim⁶ & Ray H. Baughman¹✉

Improved methods are needed for harvesting mechanical energy. Coiled carbon nanotube yarns, termed twistrans, use stretch-induced changes in electrochemical capacitance to convert mechanical energy to electricity. Elongation of the yarn produces such large lateral Poisson's ratios that the yarns are highly stretch densified, which contributes to harvesting. Here we report plied twistrans, instead of coiled, which increase the energy conversion efficiency of the yarns from 7.6% to 17.4% for stretch and to 22.4% for twist. This is attributed to additional harvesting mechanisms by yarn stretch and lateral deformations. For harvesting between 2 and 120 Hz, our plied twistran has higher gravimetric peak power and average power than has been reported for non-twistran, material-based mechanical energy harvesters. We sew the twistrans into textiles for sensing and harvesting human motion, deploy them in salt water for harvesting ocean wave energy and use them to charge supercapacitors.

The world's energy needs are so great and the consequences of excessive fossil fuel use are so damaging that improved technologies are increasingly sought for harvesting solar, waste chemical, thermal and mechanical energies. While various new technologies are being developed for harvesting mechanical energy, the centuries-old technology of electromagnetic generators is principally deployed for large-scale energy harvesting. However, while electromagnetic harvesters perform wonderfully in hydropower stations and large windmills, their gravimetric performance degrades when downsized for smaller-scale needs^{1,2}. New or radically improved technologies^{3,4} for harvesting mechanical

energy use triboelectric⁵⁻⁷, piezoelectric^{8,9}, dielectric elastomer^{10,11}, electrochemical capacitance¹²⁻¹⁷, electrostatic induction¹⁸ or moving ionic liquid¹⁹⁻²³ effects.

One of the newest types of harvester is the twistran—so called because electricity is generated by the twist changes that result from either stretching a coiled carbon nanotube (CNT) yarn or twist insertion into a twisted CNT yarn^{13,24}. Stretch or twist insertion increases the yarn density, which decreases the electrochemically accessible surface area of a CNT yarn as electrochemical double layers are temporarily decreased by interlayer contact. These twistrans are automatically

¹Alan G. MacDiarmid NanoTech Institute, University of Texas at Dallas, Richardson, TX, USA. ²School of Chemistry, Xi'an Jiaotong University, Xi'an, China.

³Department of Mechanical Engineering, University of Texas at Dallas, Richardson, TX, USA. ⁴Nano-Science & Technology Center, Lintec of America, Plano, TX, USA. ⁵Department of Engineering Mechanics, School of Civil Engineering, Wuhan University, Wuhan, China. ⁶Center for Self-Powered Actuation, Department of Biomedical Engineering, Hanyang University, Seoul, South Korea. ⁷These authors contributed equally: Mengmeng Zhang, Wenting Cai. ✉e-mail: ray.baughman@utdallas.edu

charge injected by electron or hole donation from the electrolyte, due to the electrochemical potential difference between the CNT yarn and the surrounding electrolyte. Consequently, a twistron output voltage is generated by the mechanically induced capacitance changes resulting from this decrease in the electrochemically accessible surface area. As the electrochemical double-layer capacitance (C) decreases because of yarn densification, voltages (V) that enable energy harvesting are generated according to the equation $Q = CV$ (where Q is the equilibrium injected charge).

Like for dielectric elastomer harvesters^{10,11}, mechanical deformation causes capacitance changes that generate voltage changes that enable energy harvesting. However, while thousand-volt applied bias voltages are typically used to obtain charge injection for dielectric elastomer harvesters, no external power source is needed for this charge injection for electrochemical twistrons¹³. While no other material-based harvesting technology provided a higher reported peak power than twistron harvesters for stretch frequencies between 0.1 and 30 Hz, the first-reported twistrons had an energy conversion efficiency of -1.1%¹³ and the recently reported twistrons provide an energy conversion efficiency of no higher than 7.6%²⁴. The goals are to dramatically increase the twistron energy conversion efficiency, demonstrate energy harvesting by lateral yarn deformation and better understand the origin of twistron harvesting.

The present advances result from transitioning from the previously used coiled twistrons to homochirally plied twistrons. While the plied yarns used in textiles largely deploy opposite handedness of twist and plying to provide stability against untwist²⁵, our highest-performance plied yarns have the same handedness of twist and plying. Hence, they are homochiral rather than heterochiral. We used these plied twistrons to demonstrate a tensile energy conversion efficiency of up to 17.4%, which is 16.6 and 2.3 times that of the first-reported¹³ and recently reported coiled twistrons²⁴, respectively. The presently obtained energy conversion efficiency for torsional energy harvesting was even higher: 22.4%. While trying to understand the origin of the high performance of plied twistrons, we discovered that lateral compression of various kinds of twistron yarns can generate electricity. Surprisingly, both stretching and laterally compressing a twistron harvester causes the capacitance to decrease. These plied twistrons can be uniaxially stretched by 40% at 50 Hz to generate a peak electrical power of 1,475 W kg⁻¹ and an average power of 438 W kg⁻¹. To obtain comparable performance at this frequency for previous coiled twistrons required either expensive thermal annealing at -2,500 °C under tensile stress or the addition of reduced graphene oxide as a yarn guest²⁴. The maximum energy per cycle during continuous cycling of these plied twistrons is 315 J kg⁻¹ at 0.1 Hz, which is 2.5-fold that of previous guest-free, non-thermally treated twistrons at this frequency²⁴. The energy per cycle for the plied twistrons is 80 J kg⁻¹ at 2 Hz, which is 6.7-fold that previously reported²⁶ for non-twistron, material-based harvesters for this or higher frequencies.

Plied twistron fabrication

Plied twistrons were made from twisted CNT yarns of -90 μm diameter that were fabricated by our cone-spinning process¹³. This involves drawing CNT sheets from a chemical-vapour-synthesized 220-μm-high CNT forest²⁷, forming a cylinder from a stack of length-oriented sheet ribbons and twisting this cylinder under 42 MPa stress until just below the twist that initiates yarn coiling (Supplementary Figs. 1–4). Tensile stresses are normalized to the yarn's cross-sectional area before the onset of coiling, or to n times this area when n yarns are plied (Supplementary Fig. 5). Changing the inserted twist from the maximum pre-coiling twist or changing the applied stress for this twist insertion for the precursor yarns from -42 MPa degrades harvesting for three-ply twistrons (Supplementary Fig. 6). For this stress, the Herman's orientation factor (HOF)²⁸ for CNTs on the yarn surface was 0.63 (Supplementary Fig. 7). Harvesting optimization for this high HOF is

understandable, since increasing the HOF increases the interaction between the electrochemical double layers on neighbouring nanotube bundles¹². The energy per cycle decreases for a higher HOF yarn, probably because of an increase in bundling, which decreases the observed capacitance.

Before plying, this yarn underwent stretch cycles that increased the yarn strength (from 0.27–0.90 GPa), yarn modulus (from 2.8–9.0 GPa) and CNT alignment and helped to stabilize the yarn against untwist (Supplementary Fig. 8). The highest harvester performance was obtained by plying, under a 22 MPa load, the three above yarns in the same twist direction as the initial yarn twist until immediately before the onset of plied yarn coiling (Supplementary Figs. 9 and 10). Coiled yarns were fabricated from the same CNT yarns that were plied, by applying a 42 MPa tensile stress during the entire twist insertion process.

Figure 1a compares scanning electron microscope (SEM) images of a three-ply yarn and a coiled yarn. The yarn spring index is important for harvesting, which is $(D - d)/d$, where D is the outer yarn diameter and d is the diameter of an individual yarn when viewed on the yarn surface (Fig. 1a and Supplementary Fig. 11). Unless otherwise noted, performance-optimized three-ply yarn harvesters, having a spring index of -1.1 and a coil bias angle of 47°, were used. These harvesters are called optimized ply structure (OPS) harvesters. The investigated performance-optimized coiled twistrons have a smaller spring index (0.4) and a larger coil bias angle (68°) than for OPS harvesters.

While an external inter-electrode bias voltage increases the injected charge that enables energy harvesting, there is no need to apply this external voltage for twistrons, since the required charge injection is automatically provided by the chemical potential difference between the electrolyte and the CNTs. The measured self-bias voltage for twistrons in 0.1 M aqueous HCl electrolyte (507 mV) is independent of twistron geometry. To characterize twistron performance, an electrochemical cell consisting of a twistron working electrode, a high-surface-area buckypaper counter electrode and an Ag/AgCl reference electrode are used (inset of Fig. 1b).

Effects of plied yarn chirality on harvesting

Without using a mandrel to prevent cancellation of oppositely directed twist, it is impossible to make a coiled guest-free heterochiral CNT yarn^{13,24}. Contrastingly, a mandrel-free heterochiral plied yarn can be made, since the plied yarns act as a mandrel for each other after a critical degree of plying twist insertion. This is demonstrated by comparing the twist density dependencies of open-circuit potential (OCP) and capacitance for homochiral and heterochiral plying. While the OCP and capacitance of a homochiral yarn monotonically change with increasing or decreasing plying twist during homochiral plied yarn fabrication (Supplementary Fig. 12), the OCP for a heterochiral plied yarn first decreases with increasing plying twist density, due to partial cancellation of yarn twist with plying twist (Fig. 1e). Thereafter, the plied yarns are in such close contact that this contact serves as a mandrel to prevent further yarn untwist, thereby enabling the OCP to reach a minimum and thereafter increase (Fig. 1e). Since the OCP is the ratio of the injected charge to yarn capacitance, OCP and capacitance changes are oppositely directed. Unless otherwise mentioned, the applied tensile deformation of a twistron is sinusoidal.

Since heterochiral plying untwists the component yarns, this untwist decreases the capacitance change during harvesting and increases the maximum reversible tensile strain for the harvester. As a result of this decreased capacitance change, the open-circuit voltage (OCV) (102 mV) for a heterochiral plied harvester is much lower than for a homochiral plied harvester (265 mV) for a 40%, 1 Hz deformation (Fig. 1f and Supplementary Figs. 13 and 14). The OCV, average power and energy per cycle at maximum reversible deformation of a heterochiral plied twistron are much smaller than for a homochiral plied twistron for any applied stretch and frequency (Supplementary Fig. 14c,d).

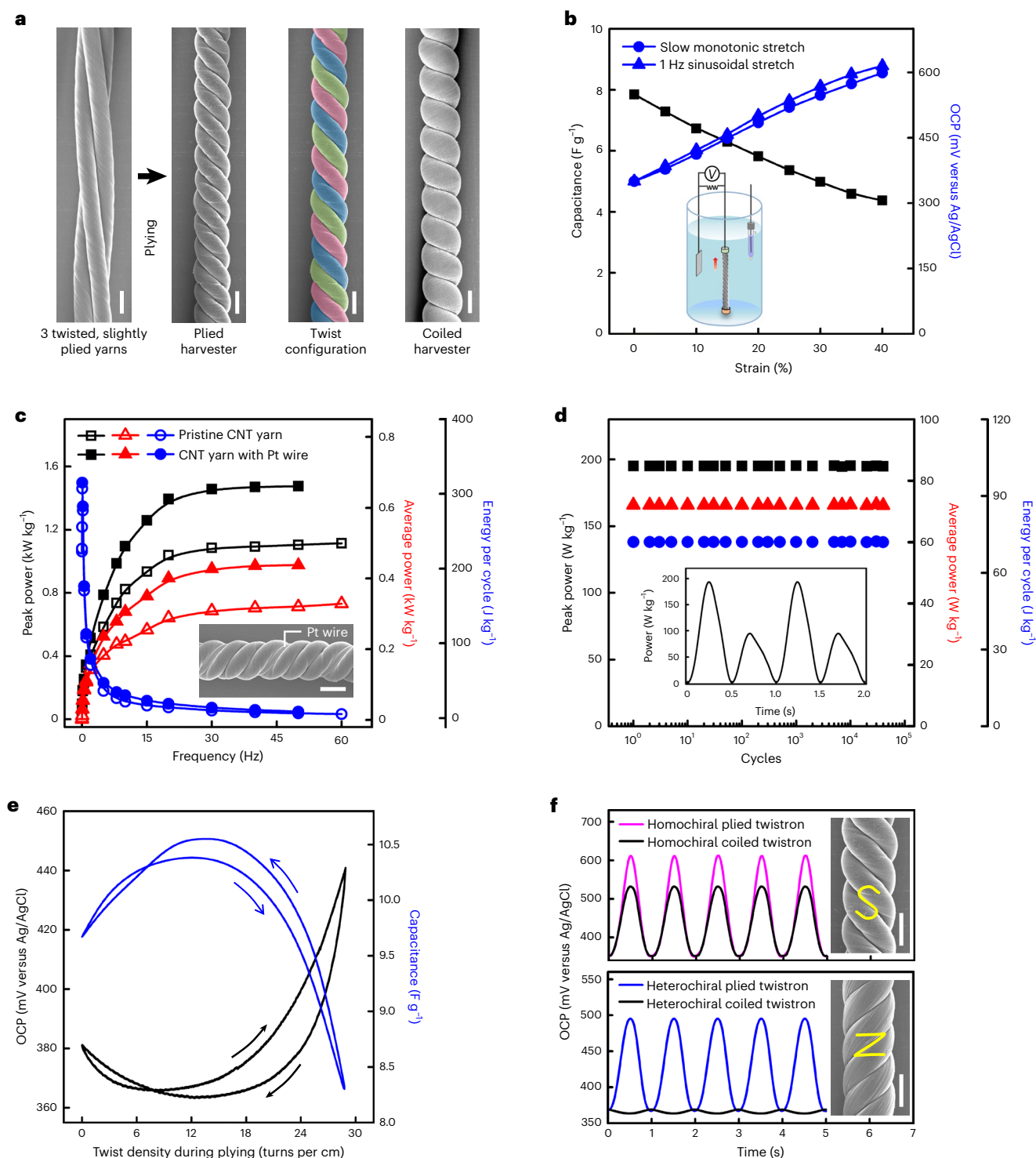


Fig. 1 | Fabrication, SEM images and sinusoidal tensile deformation characterization of homochiral three-ply twisted yarn harvesters in 0.1 M aqueous HCl electrolyte.

a, Fabrication of a three-ply twisted yarn harvester involves cone spinning a CNT sheet, twist insertion to form a single twisted yarn whose strength and modulus are increased by dynamic stretch, and plying three twisted yarns. From left to right, for yarns having a yarn twist of 28 turns per cm and a plying twist density of four and 16 turns per cm, respectively, SEM images of slightly plied yarn, fully plied yarn (with and without colours to identify individual plies) and a self-coiled harvester are shown. Scale bars, 100 μm . **b**, Capacitance and OCP versus applied strain for the pictured three-ply yarn harvester. Inset, illustration of the electrochemical cell used for twistron characterization. **c**, Frequency dependencies of peak power, average power and energy per cycle for 40% stretch of the three-ply yarn harvester, with and

without a coiled 25- μm -diameter Pt wire current collector. Inset, SEM image of a three-ply yarn harvester with incorporated Pt wire (scale bar, 100 μm). **d**, Peak power, average power and electrical energy per cycle during 40,000 sinusoidal, 1 Hz cycles to 25% strain in 0.1 M HCl. Inset, output power versus time during stretch cycling for a 65Ω load resistor. **e**, Plying twist dependencies of OCP and capacitance during heterochiral plied harvester fabrication. The arrows show the direction of twist density change. **f**, Time dependence of OCP for (top) the homochiral plied harvester (40% strain) compared with that for a homochiral self-coiled yarn for the same tensile deformation, and (bottom) the heterochiral three-ply yarn (50% strain) compared with that of a heterochiral rubber mandrel-supported coiled yarn (80% strain; 0.5-cm-diameter rubber core mandrel). Inset, SEM images of a homochiral plied harvester (S twist) and a heterochiral plied harvester (Z twist) (scale bars, 100 μm).

Quasi-homochiral yarns, in which not all component yarns have the same chirality as the chirality of plying, have lower harvesting than do fully homochiral plied yarns. For example, a quasi-homochiral three-ply harvester, in which one yarn has a different chirality, produced an OCV of 180 mV and a peak power of 128 W kg⁻¹ when stretched to 40% strain at 1 Hz— values much lower than for a homochiral three-ply yarn harvester (Supplementary Fig. 15). This results in the poor performance of the quasi-homochiral harvester, since a stretch-induced decrease in the twist of plying increases the capacitance of yarn components having different handedness than the twist of plying. Unless otherwise mentioned, the described yarns are fully homochiral.

The harvesting of a three-ply homochiral yarn is higher than for homochiral plied yarns containing either higher or lower numbers of plied yarns (Supplementary Fig. 16). This optimized three-ply homochiral yarn performance probably results from two effects. First, the capacitance decrease from lateral compression is larger for three-ply yarns than for two-ply yarns. Second, the spring index due to plying increases when larger numbers of yarns are plied together, reducing harvesting by reducing the capacitance contribution from coil twist to yarn twist conversion.

Energy and power generation by OPS harvesters

The OCV, output power and energy per cycle for an OPS harvester were measured from 0.01–60 Hz in 0.1 M HCl electrolyte (Fig. 1c and Supplementary Fig. 17). For 40% stretch at 60 Hz, the peak and average power for the OPS harvester were 1,115 and 329 W kg⁻¹, respectively, while the maximum output energy per cycle at 0.1 Hz reached 307 J kg⁻¹ (Fig. 1c). To increase the output power and energy by decreasing the internal resistance, a 25- μ m-diameter Pt wire was incorporated into the OPS harvester during plying (inset of Fig. 1c). This increased the peak and average power to 1,475 and 438 W kg⁻¹, respectively, for a 40% strain at 50 Hz. Moreover, the energy per cycle reached 315 J kg⁻¹ for 0.1 Hz deformation, which is 2.5-fold that of previous guest-free, non-thermally treated twistrans at this frequency²⁴. For a 0.1 Hz deformation, replacing the sinusoidal mechanical input with a square-wave input for a Pt wire-plied OPS harvester increased the load resistance-optimized peak power from 98–1,032 W kg⁻¹ (Supplementary Fig. 18).

Energy harvesting in 0.1 M alkali metal chloride electrolytes is lower than for the HCl electrolyte for all investigated frequencies, due to the lower self-bias voltage and ionic conductivity of these electrolytes²⁹ (Supplementary Figs. 19, 20 and 40). Nevertheless, a 922 W kg⁻¹ peak power and a 298 W kg⁻¹ average power were obtained for an optimized LiCl electrolyte for sinusoidal deformation at 60 Hz (Supplementary Figs. 21 and 22). When a Pt wire was incorporated, the peak power, average power and energy per cycle for the OPS harvester in 0.1 M LiCl electrolyte were 1,340 W kg⁻¹, 415 W kg⁻¹ (at 50 Hz) and 120.4 J kg⁻¹ (at 0.5 Hz), respectively (Supplementary Fig. 22d). Since solution-spun CNT yarns have an almost identical conductivity to Pt wire³⁰ and a very small capacitance, these yarns could replace expensive Pt wire for decreasing twistran resistance.

Due to insufficient time for energy collection and yarn structure equilibration, the peak power and average power decrease with increasing sinusoidal deformation frequencies above 60 Hz for harvesters stretched to 40% strain in 0.1 M HCl or 0.1 M LiCl electrolyte (Supplementary Fig. 22c and 23). Since electrolyte extrusion during stretch-induced densification is faster than electrolyte absorption during stretch–release, the ratio of energy harvested in 0.1 M HCl during stretch to that harvested during stretch–release approximately linearly increases with deformation frequency from 1.38 at 2 Hz to 23.1 at 30 Hz, but is constant (about 1.38) below 0.1 Hz (Supplementary Fig. 24). Nevertheless, the peak power and average power for an OPS harvester in 0.1 M HCl reached 956 and 226 W kg⁻¹ at 120 Hz, respectively. For comparison, the highest previously reported peak powers for material-based harvesters at very high frequencies were 54 W kg⁻¹ at 60 Hz for a piezoelectric harvester³¹ and 0.84 W kg⁻¹ at 34 Hz for a

triboelectric harvester³². Harvester performance and morphology were maintained for the investigated 40,000 sinusoidal stretch cycles at 1 Hz to 25% strain in both aqueous HCl and LiCl electrolytes (Fig. 1d and Supplementary Figs. 25–27).

The maximum peak power and average power for our OPS harvester (328 and 108 W kg⁻¹, respectively, for a 1 Hz, 40% strain) were about twice that for a coiled three-ply yarn harvester (168 and 54 W kg⁻¹, respectively, for a 1 Hz, 60% strain) obtained by overtwisting a three-ply yarn (Supplementary Fig. 28). For comparison, a three-ply homochiral harvester, in which each of the plies are coiled CNT yarns, provided an average power of only 30 W kg⁻¹ for a 1 Hz, 75% stretch (Supplementary Fig. 29).

Energy conversion efficiency of OPS harvesters

From the ratio of the per-cycle output electrical energy to the per-cycle input mechanical energy, the mechanical-to-electrical energy conversion efficiencies for the OPS harvesters were obtained for frequencies from 0.01–2 Hz. No differences were found in the input mechanical energies required for 0.1 M aqueous electrolytes of HCl, LiCl and NaCl, since these electrolytes have similar viscosities, which are relevant for electrolyte extrusion during stretch and reabsorption during stretch–release. However, due to the higher ionic conductivity²⁹ and OCV for the HCl electrolyte, the maximum energy conversion efficiency was much higher for the HCl electrolyte (14.0% at 0.1 Hz) than for the LiCl (4.8% at 0.5 Hz) and NaCl (2.0% at 1 Hz) electrolytes (Fig. 2a and Supplementary Fig. 30). This 14.0% efficiency is much higher than was first reported¹³ and recently reported²⁴ for coiled twistrans (1.05 and 4.66%, respectively). The input mechanical energy per cycle for the three-ply yarn harvester was much lower than for the coiled three-ply yarn harvester for sinusoidal deformation at any frequency to 40% strain (Fig. 2b and Supplementary Fig. 31). As a result, the maximum energy conversion efficiency (14.0% at 0.1 Hz) for the non-coiled three-ply yarn harvester was 5.8 times that for the coiled three-ply yarn harvester (2.4% at 0.02 Hz).

The energy conversion efficiency and output energy were increased by using our interrupted deformation harvesting (IDH) method, in which time intervals are inserted where harvesting is conducted at one or more strain extremes, while the harvester is not being deformed. If IDH is applied for both strain extremes or only at the zero strain or maximum strain extremes, this is called the IDH_{om}, IDH₀ or IDH_m method, respectively. The time interval of IDH for the presently used sinusoidal deformations in 0.1 M HCl electrolyte is the measured interval for capturing nearly all of the electricity. By inserting a 15 s IDH_{om} during 0.1 Hz, 40% deformation of a Pt wire-plied OPS harvester, the harvested energy per cycle and the energy conversion efficiency were increased to 401 J kg⁻¹ and 17.1%, respectively, compared with 315 J kg⁻¹ and 14.3% for continuous deformation (Fig. 2c and Supplementary Fig. 32). Use of a 15 s IDH_{om} during a 0.1 Hz, 35% deformation increased the electrical energy per cycle to 356 J kg⁻¹ and the energy conversion efficiency to 17.4%. Shorter interruption times (5 s) for IDH_{om} provided nearly the same harvested energy per cycle and energy conversion efficiency (Supplementary Fig. 33). Using a 2 s IDH₀ at this frequency and strain eliminated the need for state latching, but the output energy per cycle and the energy conversion efficiency were decreased to 320 J kg⁻¹ and 16.1%, respectively (Supplementary Figs. 34 and 35).

The energy conversion efficiency was further increased for our three-ply OPS twistrans by replacing tensile energy harvesting with torsional energy harvesting. Isometrically uptwisting a 9.2-mm-long OPS harvester (having a plying twist of 16 turns per cm) by ten turns (10.8 turns per cm) generated an OCV of 184 mV and a corresponding capacitance decrease of 36.4%, which are much higher than for uptwisting the plying twist of a three-ply heterochiral harvester (Supplementary Figs. 36a and 37). The OCV rapidly increases and the average power-optimizing load resistance rapidly decreases with increasing

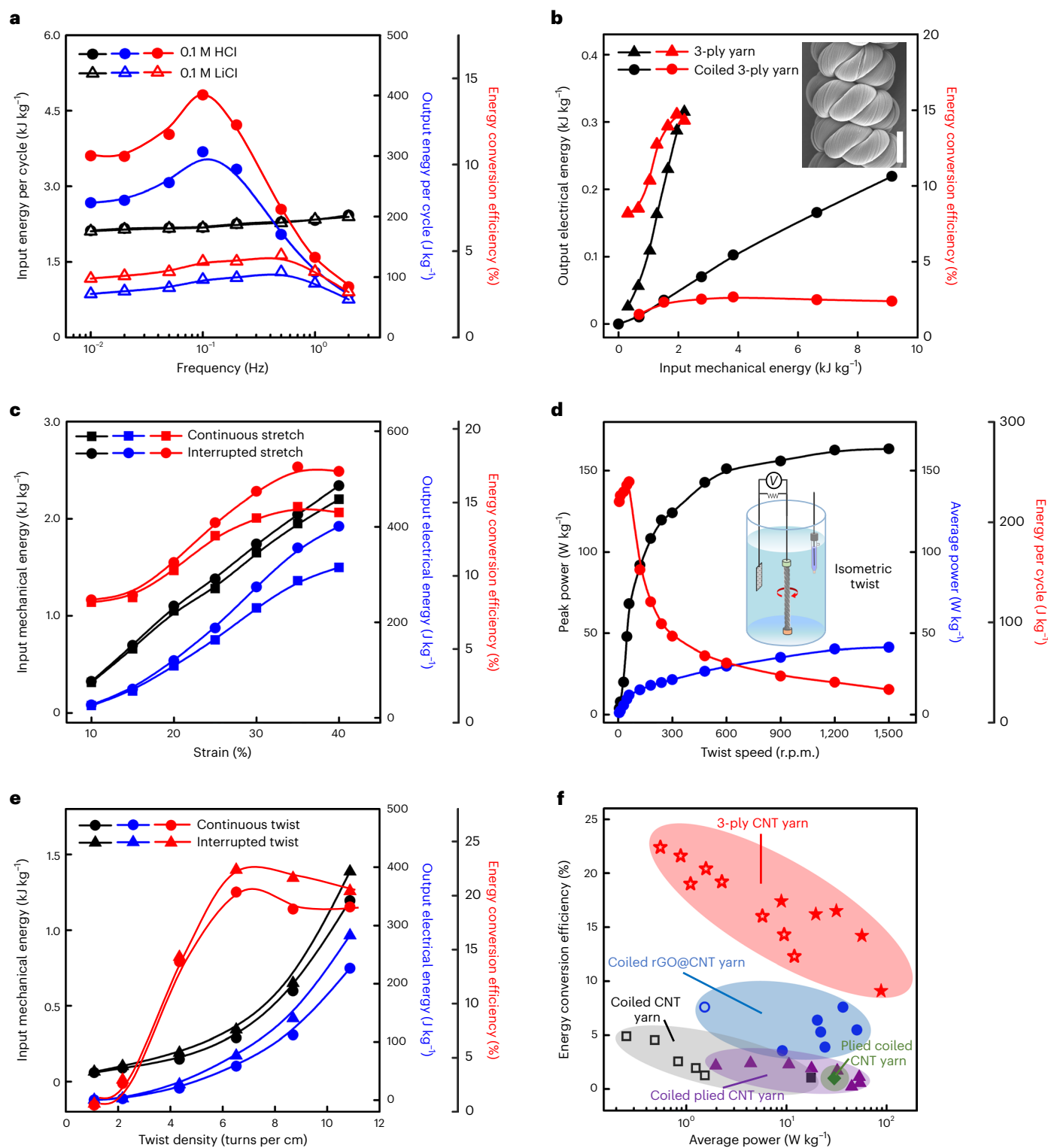


Fig. 2 | Characterization of the tensile and torsional energy conversion efficiencies of three-ply yarn twistrons. **a**, Frequency dependencies of the per-cycle input mechanical energy and output electrical energy, and the thereby derived energy conversion efficiency, for a 40% sinusoidal tensile deformation of a three-ply yarn harvester in HCl and LiCl electrolytes. **b**, Dependence of the output energy and energy conversion efficiency of a three-ply yarn at 0.1 Hz and a coiled three-ply yarn at 0.02 Hz on the input mechanical energy during sinusoidal stretch. The used frequencies maximize the output electrical energy and energy conversion efficiency. Inset, SEM image of a coiled three-ply yarn harvester (scale bar, 100 μm). **c**, Strain dependencies of per-cycle input mechanical energy and output electrical energy, and the energy conversion efficiency, of a three-ply yarn harvester sinusoidally stretched at 0.1 Hz in 0.1 M HCl electrolyte. **d**, Twist

speed dependencies of peak power, average power and energy per cycle of a three-ply yarn harvester during isometric twist in 0.1 M HCl electrolyte. Inset, illustration of a three-ply yarn harvester during isometric twist. **e**, Dependencies of the per-cycle input mechanical energy, output electrical energy and energy conversion efficiency on the twist density used for torsional mechanical energy harvesting for a three-ply yarn harvester twisted isometrically at 12 r.p.m. The twistron length in **d** and **e** was 9.2 mm. **f**, Tensile energy conversion efficiency for the frequency of a sinusoidal twistron tensile deformation that maximizes this efficiency versus the average power at this frequency (solid symbols) and the torsional energy conversion efficiency for the twist speed of an isometric twist that maximizes this efficiency versus the average power at this twist speed (open symbols). rGO, reduced graphene oxide.

twist speed until approximate plateaus at -60 r.p.m. (Supplementary Fig. 36c). While the energy per cycle reaches a peak of 240 J kg^{-1} for a 60 r.p.m. twist speed, the peak power and average power monotonically increase with twist speed until they reach maximum values of 163 and 41 W kg^{-1} , respectively, at the highest twist speed investigated, $1,500$ r.p.m. (Fig. 2d). The peak power, average power and energy per cycle for the OPS harvester were maintained for the investigated $5,000$ isometric twist cycles to 10.8 turns per cm at 120 r.p.m. (Supplementary Fig. 36d).

Most importantly, the torsional energy conversion efficiency for the OPS harvester reached 19.0% for twist insertion at 12 r.p.m. (Supplementary Fig. 36e). This efficiency was increased to 20.4% by applying our interrupted deformation method to torsional energy harvesting. By extending harvesting for an optimized time of 40 s after twist insertion was completed and after twist removal ended, the per-cycle energy harvested was increased from 226 – 283 J kg^{-1} when using a 12 r.p.m. twist speed for 10.8 turns per cm of twist insertion and removal (Supplementary Fig. 38). The maximum efficiency for torsional energy harvesting, which is for a twist density change of 6.5 turns per cm, increased from 20.4 – 22.4% (Fig. 2e). The Fig. 2f comparison of three-ply twistrons with prior-art twistrons^{13,24} shows that the simultaneously obtained combination of high-energy conversion efficiency and high average power makes the three-ply twistrons very attractive for applications. However, our presently realized maximum energy conversion efficiency is lower than has been reported at low frequencies for more mature technologies. For example, dielectric elastomer generators¹¹ have a demonstrated energy conversion efficiency of $\sim 27\%$ at low frequencies for an applied voltage of ~ 3 kV, and triboelectric harvesters³³ have a demonstrated energy conversion efficiency of up to 85% at low frequencies.

Poisson's ratio, density and lateral compression effects

Previous descriptions of stretch-induced twistrion capacitance changes only considered the stretch-induced transfer of coiling twist to yarn twist, which cannot fully explain the capacitance changes that enable harvesting. However, Supplementary Fig. 39a shows that stretching a twisted yarn increases the yarn density and decreases the yarn capacitance, even though this stretch decreases the yarn's bias angle. The yarn's Poisson's ratio (ν) for a yarn direction stretch (dL/L) enables reliable calculation of stretch-induced yarn density changes, since the fractional change in yarn volume is $(1-2\nu)dL/L$. Hence, when this Poisson's ratio exceeds 0.5 , the yarn becomes stretch densified^{34,35}, while most materials are stretch rarified.

Figure 3a shows the strain dependence of the OCV, the average Poisson's ratio up to the indicated strain and the yarn's density for a twisted CNT yarn having an initial bias angle of 33.3° and a twist density of 28 turns per cm. These results show that the average Poisson's ratio increases from 1.18 for 1% strain to 1.40 for 5% strain, which causes 10.1% stretch-induced densification in going from 0 – 5% strain. This Poisson's ratio effect causes the yarn density to increase from 1.19 g cm^{-3} at 0% strain to 1.31 g cm^{-3} at 5% strain, which produces an OCV of 45 mV. Using an identically made twistrion, about the same yarn density change (from 1.18 – 1.31 g cm^{-3}) and OCV (46 mV) are produced by isometrically increasing the twist by 2.7 turns per cm (Fig. 3a and Supplementary Fig. 39). Hence, these very different deformations of almost identical twisted yarns, up to their maximum reversible deformation, provide essentially the same OCV and density changes for stretch frequencies and twist rates at which OCV is shown to be rate insensitive (Fig. 3a and Supplementary Fig. 41).

In contrast with the large stretch-induced increase in Poisson's ratio of twisted yarns, the Poisson's ratios of a three-ply yarn and a coiled yarn only weakly depend on strain and remain 1.01 and 0.92 , respectively, for elongations of up to 15% (Supplementary Fig. 42). This large Poisson's ratio of the three-ply yarn harvester causes a

density increase from 1.78 g cm^{-3} at 0% strain to 2.10 g cm^{-3} at 15% strain (Fig. 3b). This density increase for the three-ply yarn was larger than for the coiled yarn, whose density was 1.91 g cm^{-3} at 0% strain, resulting in a higher OCV for three-ply yarns than coiled yarns for either a given strain or a given percentage density change (Supplementary Fig. 42).

Published work on twistrons has only considered harvesting by mechanically elongating a yarn or changing the yarn twist¹³. We now show that lateral compression of either a twisted, plied or coiled CNT yarn produces capacitance changes and resulting OCVs that generate electricity. These yarns were subjected to yarn thickness direction compression while under constant yarn direction tensile strain. Figure 3c shows that such uniaxial compression, using up to ~ 7 MPa pressure (normalized to the midpoint cross-sectional area of a parallel array of undeformed twistrion yarns), produces reversible capacitance decreases that generate OCVs of 48 , 37 and 20 mV for three-ply, twisted and coiled yarn, respectively.

The lateral inter-ply compression that results from yarn stretch is sufficiently high to eliminate the interior inter-ply void space when the tensile strain is increased to 15% (Fig. 3e and Supplementary Figs. 43 and 44). This compression contributes to the surprisingly higher energy harvesting for a given stretch for a homochiral plied yarn than for a homochiral coiled yarn (Fig. 1f and Supplementary Figs. 45–47). When slowly stretched from 0 – 40% strain, the capacitance of an OPS harvester decreased from 7.9 to 4.4 F g^{-1} and the OCP increased from 350 – 615 mV (Fig. 1b and Supplementary Fig. 48). In contrast, this slow stretch of a comparable homochiral coiled twistrion decreased the capacitance from 5.1 to 3.3 F g^{-1} and increased the OCP from 372 – 552 mV (Supplementary Fig. 45).

Also, density increases due to inter-ply compression can contribute to the following differences between heterochiral yarns that are coiled or plied. Stretching a heterochiral coiled yarn decreases the twist of coiling, which produces a decrease in the yarn twist and a corresponding increase in the capacitance and decrease in the OCP¹³ (Fig. 1f). While stretching a heterochiral plied yarn also provides the same transfer of the coiling twist to oppositely directed yarn twist, a heterochiral plied yarn decreases in capacitance and increases in OCP (Fig. 1f). This can be explained if stretch-induced inter-ply compression for the plied yarn is overwhelming the stretch-induced density decrease due to transfer of coil twist to component yarns with opposite yarn twist.

For a coiled yarn, stretch deformation only induces an increase in the twist of coiling, which produces an increase in the yarn twist and a corresponding decrease in the capacitance and increase in the OCV. In contrast, stretching a three-ply yarn not only provides transfer of coiling twist to yarn twist, but also provides high lateral inter-ply compression (as evidenced by the X-ray tomography images of Fig. 3e), thereby further decreasing the capacitance and resulting in a higher increase in OCV. Therefore, the inter-ply compression and large Poisson's ratio of a three-ply yarn contribute a higher density increase for a given strain than for a coiled yarn. This enables the three-ply yarn harvesters to provide a larger capacitance decrease, and to therefore provide higher energy harvesting and higher energy conversion efficiency compared with the coiled yarn harvesters.

For various types of deformation-induced capacitance changes, a simple equation predicts the open-circuit voltage at strain ϵ , OCV_ϵ , when only the harvesting electrode (with charge Q) changes potential and the OCV_ϵ is zero for zero deformation. This expression is $\text{OCV}_\epsilon = Q(C_\epsilon^{-1} - C_0^{-1}) = -(Q/C_0)(\Delta C/C_\epsilon)$, where C_0 and C_ϵ are the capacitances at zero and ϵ deformations, respectively, and $\Delta C = C_0 - C_\epsilon$. The equilibrium Q/C_0 should equal the self-bias voltage, which Supplementary Fig. 49a shows to be about the same for twisted, coiled and plied CNT yarns after 40 min of exposure to the 0.1 M HCl electrolyte that is needed for bias voltage equilibration. Consequently, it is not surprising that the OCV_ϵ values for torsional, tensile or lateral deformation of twisted, coiled or plied yarns roughly coincide when plotted versus $\Delta C/C_\epsilon$ (Fig. 3d and Supplementary Fig. 49b). Supplementary Fig. 49c

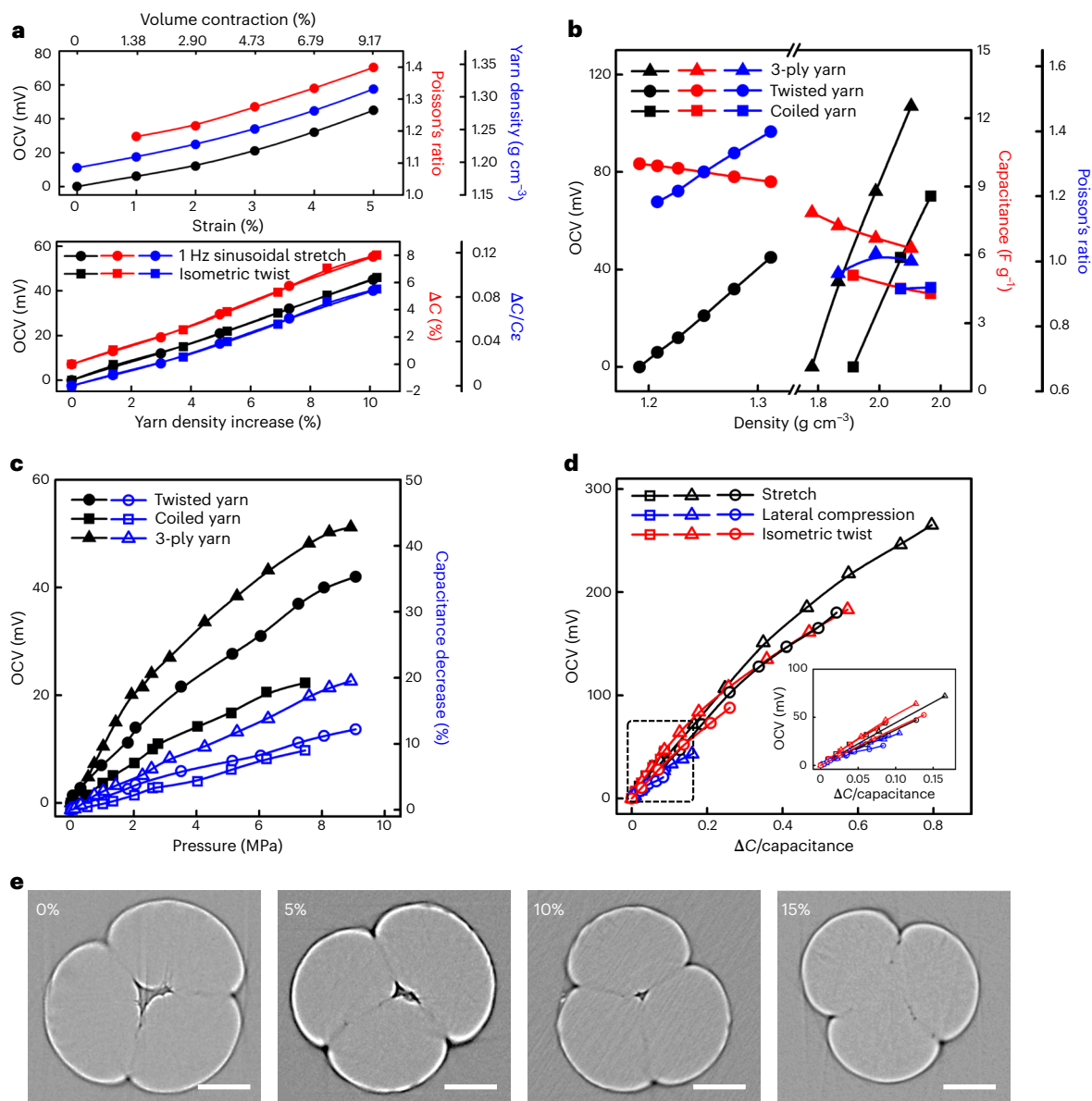


Fig. 3 | Dependencies of OCV on strain, yarn density, lateral pressure and the ratio of capacitance change to the capacitance for a given deformation.

a, Top, strain dependencies of OCV, Poisson's ratio and yarn density when continuously stretching a twisted yarn at a lower strain rate (1% per second) than is required for the OCV to become rate insensitive. The Poisson's ratio at a particular strain is the average value of Poisson's ratio up to that strain. Bottom, for tensile stretch at 1 Hz and isometric twist at $161^\circ \text{ cm}^{-1} \text{ s}^{-1}$, the dependencies of the peak OCV, percentage capacitance decrease and ratio of capacitance change to capacitance for a given deformation on the percentage yarn density increase of twisted yarns are shown. **b**, Dependencies of OCV (for a sinusoidal stretch at a frequency (1 Hz) that is sufficiently low that the OCV is strain rate insensitive), static capacitances and Poisson's ratios for twisted, coiled and three-ply yarn

harvesters on the static density. **c**, Dependencies of OCV and capacitance decrease for twisted, coiled and three-ply yarn harvesters on the applied lateral pressure. The harvesters were wrapped on a ceramic plate with a pore diameter of $\sim 10 \mu\text{m}$, and an identical porous plate was used to apply pressure. **d**, Dependence of OCV for twisted (squares), coiled (circles) and plied yarn (triangles) twistrons on the ratio of capacitance change to capacitance for a given deformation. The applied twistron deformations included tensile stretch, lateral compression and isometric twist insertion to increase the initial twist. Inset, magnified-scale results for the congested data region within the dashed-line box. **e**, X-ray tomography images of the cross-sections of nearly identical three-ply yarn harvesters for 0, 5, 10 and 15% stretch (scale bars, $50 \mu\text{m}$). The interior inter-ply void space disappeared when the three-ply harvester was stretched to 15%.

illustrates the origin of the capacitance decrease and potential magnitude increase for a stretched homochiral plied harvester.

Applications of three-ply yarn harvesters

For potential use for harvesting ocean wave energy, an OPS harvester was characterized between -4 and 60°C in 0.6 M aqueous NaCl, which is similar to seawater¹². While the generated OCV and the potential of zero charge for the OPS harvester changed negligibly with temperature (Supplementary Fig. 50), the energy per cycle for a 1 Hz, 40% sinusoidal

deformation varied by 25.6%, probably due to the temperature dependence of ionic conductivity³⁶ (Fig. 4a). For a common ocean surface temperature of -15°C , the OPS harvester provided an average power of 27 W kg^{-1} for a 1 Hz, 40% tensile strain. To further demonstrate wave energy harvesting, an OPS harvester weighing 0.15 mg and a counter electrode were immersed in 0.6 M aqueous NaCl electrolyte in an aquarium. The OPS harvester was attached between a balloon and the aquarium bottom. By simulating waves of $\sim 0.85 \text{ Hz}$, the OPS harvester electrode provided an average power of 16.9 W kg^{-1} for approximately

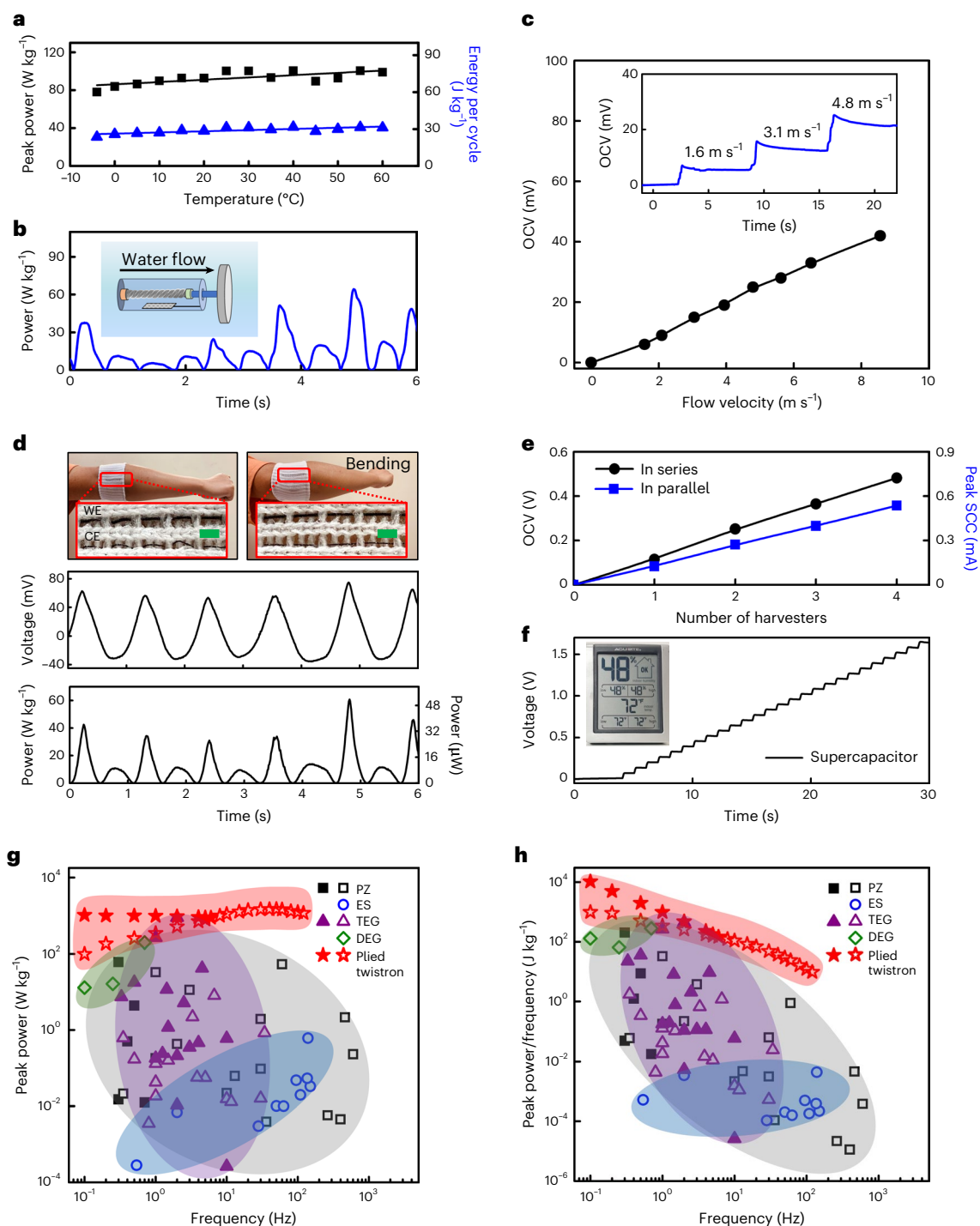


Fig. 4 | Applications and comparisons of performance with literature

results. **a**, Least squares linear fits of the temperature dependencies of peak power and energy per cycle for 1 Hz, 40% sinusoidal strain of a three-ply yarn harvester in 0.6 M NaCl electrolyte. **b**, Time dependence of harvested power for the experiment in the inset to simulate the harvesting of turbulent water flow. The output power is for a 0.15-mg, three-ply yarn harvester when the water flow velocity was switched from 0.21–0.62 m s^{-1} at -1.4 Hz. **c**, Flow velocity dependence of the generated plateau OCV for a 31.6-mm-long three-ply yarn harvester when used as a self-powered air-flow velocity sensor in 0.6 M NaCl/10 wt% poly(vinyl alcohol) gel electrolyte. The device configuration is shown in Supplementary Fig. S2. Inset, time dependence of the generated OCV for different air-flow velocities. **d**, Time dependence of the generated voltage (middle) and output power (bottom) of a 35-mm-long, three-ply yarn harvester working electrode (WE) and a 40-mm-long counter electrode (CE) when sewn into a cotton textile

as an elbow support for arm bending. Both electrodes used a 0.1 M LiCl/10 wt% poly(vinyl alcohol) gel electrolyte. Top, photographs taken before (left) and after arm bending (right) from 0–90°. The green lines are scale bars (2 mm). **e**, OCV and peak short circuit current (SCC) for a 1 Hz, 15% sinusoidal strain when three-ply yarn harvesters are connected in series or in parallel in 0.1 M LiCl electrolyte. **f**, Voltage versus time profile when charging a 220 μF supercapacitor to 1.6 V by stretching a 3.2 mg harvester array to 30% strain at 1 Hz when using the passive boost converter circuit shown in Supplementary Fig. S7. Inset, photograph of a 1.5 V digital temperature/humidity monitor (with a 2.8 inch liquid-crystal display) powered by the energy in the supercapacitor. **g, h**, Comparison of gravimetric peak power (**g**) and peak power/frequency (**h**) versus frequency for our plied harvesters and for piezoelectric (PZ), electrostatic (ES), triboelectric (TEG) and dielectric elastomer (DEG) harvesters, where the solid and open symbols are for pulsed and non-pulsed deformation, respectively.

20% strain (Supplementary Fig. 51). In addition, the plied twistron was used to harvest turbulent water flow energy and provided a comparable average power (15.2 W kg^{-1}) as for wave energy harvesting (Fig. 4b). Figure 4c shows that the OCV generated by a 31.6-mm-long, three-ply yarn harvester increased linearly with increasing air-flow velocity when this harvester was used as a self-powered air-flow sensor (Supplementary Fig. 52).

Figure 4d and Supplementary Fig. 54 show the application of textile-sewn, solid-state plied twistrons (Supplementary Fig. 53) as a harvester and a self-powered sensor for arm bending. When the arm was bent from 0 – 130° , which increased the length of the 3.5-cm-long twistron in the arm patch by $\sim 28\%$, the voltage generated across a load resistance (108Ω) was $\sim 63 \text{ mV}$. Each bending cycle generated a gravimetric peak power of 38 W kg^{-1} and a gravimetric average power of 11.3 W kg^{-1} when normalized to the CNT weight in the twistron harvester (Fig. 4d). Supplementary Fig. 55 shows the dependencies of OCV and the ratio of OCV to tensile stress or tensile strain on tensile stress or tensile strain.

Figure 4e shows the scalability of twistron output to provide increased voltages or currents by placing plied twistrons in series or in parallel, respectively. The gravimetric power and energy output are barely affected by upscaling twistron harvesters into a harvesting array (Supplementary Fig. 56). The use of a 3.20-mg harvester array to charge a supercapacitor for powering a digital temperature/humidity monitor, an electronic watch and five parallel LEDs (Fig. 4f and Supplementary Fig. 57) was demonstrated. When using a harvester with a seesaw structure, in which two identical three-ply yarns were used as the working electrode and counter electrode, almost the same peak power and average power were obtained as for a single plied yarn twistron, when normalized to the total weight of these two electrodes (Supplementary Fig. 58). This demonstration is important, since it shows that we can obtain roughly the same gravimetric output power and energy when this energy is based on either the weight of a single harvesting electrode or the weight of two harvesting electrodes. Also relevant for applications, the ionic conductivity of the HCl electrolyte is sufficiently high that the peak power and average power for an OPS harvester is insensitive to the separation between harvesting electrode and counter electrode in at least the range of between 9 and 112 mm for a deformation frequency of 1 Hz (Supplementary Fig. 59). Also, our plied twistrons can be used in strong base electrolytes, which means that the sign of the injected charge and the OCV can be reversed by changing the pH of the electrolyte (Supplementary Fig. 60).

Conclusions

For harvesting between 2 and 120 Hz, our OPS harvesters have higher gravimetric peak power and average power and higher frequency-normalized peak power and average power compared with previously reported non-twistron, materials-based harvesters (Fig. 4g,h, Supplementary Fig. 61 and Supplementary Tables 1 and 2). However, at lower frequencies, the reported average power of a triboelectric harvester³⁷ exceeds that of the twistron by 16% at a frequency of 1 Hz and the reported average power of a dielectric elastomer harvester¹¹ exceeds that of a twistron by up to 217% for frequencies below 0.5 Hz. Our OPS harvesters generated a peak power of $1,475 \text{ W kg}^{-1}$ and an average power of 438 W kg^{-1} when cycled at 50 Hz, and provided a maximum energy per cycle of 401 J kg^{-1} . More importantly, the OPS harvesters provide an energy conversion efficiency of up to 17.4% for tensile energy harvesting and up to 22.4% for torsional energy harvesting, compared with the previously reported twistron record of 7.6% for both tensile and torsional energy harvesting, which was for thermally treated, reduced graphene oxide-incorporated coiled twistrons. While previous work has shown harvesting by yarn stretch and yarn twist, we show that energy harvesting also results for lateral yarn compression, and provide evidence that stretch-induced lateral compression contributes to the outstanding performance of plied twistrons. However, a problem remains.

Until twistron harvesters can be upscaled commercially (using either CNTs or a less expensive high-strength, high-capacitance material) twistrons are not commercially competitive on a cost-per-watt-hour basis for large-scale applications requiring high-power output per application.

Methods

Fabrication of plied harvesters

Precursor twisted CNT yarns were fabricated by cone spinning¹³. This involves drawing sheets of highly oriented CNTs from a 220- μm -high CNT forest, forming an approximately 6.6-mm-diameter cylinder from a stack of 15–20 layers of ~ 20 -mm-wide sheet ribbons, so that the CNTs are oriented in the cylinder direction, and inserting twist under a constant tensile load. For this selected cylinder diameter, the mass per length of the cylinder was $\sim 44 \mu\text{g cm}^{-1}$, which corresponds to 20 sheet layers having an areal sheet density of $\sim 22 \mu\text{g cm}^{-2}$. The precursor twisted yarns were twisted under a 42 MPa load until just below the onset of coiling. This stress and the inserted pre-plying twist of 28 turns per cm for the used $\sim 90 \mu\text{m}$ yarn diameter produces a yarn with a HOF of 0.63, as measured by CNT orientation on the yarn surface. Before plying, this yarn was cycled ~ 30 times from the pre-coiling strain up to a final strain that was eventually 10% longer than the initial length, which increased the CNT alignment to a HOF of 0.69, increased the yarn's strength from ~ 0.27 – 0.90 GPa and increased yarn stability against untwist (Supplementary Information). The twist applied during plying (16 turns per cm relative to the non-plied yarn length) was the maximum twist that could be inserted under the applied 22 MPa load before the plied yarns began to coil. The same plying stress per ply was used, independent of the number of plies. The investigated coiled yarns were fabricated using the same forest type used for making plied yarns and the same cone-spinning method. However, these coiled yarns were fabricated using the 42 MPa stress for both twist insertion and coiling. Unless otherwise mentioned, the described yarns were homochiral.

Electrochemical characterization of harvester performance

To characterize twistron performance, a three-electrode electrochemical system was used, with a twistron as the working electrode and an Ag/AgCl reference electrode (inset of Fig. 1b). Unless otherwise noted, the counter electrode was a high-surface-area buckypaper wrapped Pt mesh, the electrolyte used was 0.1 M aqueous HCl and the applied tensile deformation was sinusoidal. The OCP, OCV, short-circuit current (SCC) and harvester's capacitance were measured using an electrochemical workstation (Model 3000; Gamry Instruments). Unless otherwise noted, the OCV and SCC during a cyclic deformation are the peak inter-electrode voltage and peak inter-electrode current, respectively, during this deformation. The OCP of the twistron harvester electrode is the OCP relative to the reference electrode in the electrochemical cell and the OCV is the open-circuit voltage between the working and counter electrode. The OCP is of fundamental importance for understanding, while the OCV is of more practical importance. A small potential range (0.3–0.6 V versus Ag/AgCl) was used for cyclic voltammetry measurements of electrode capacitance to avoid a redox reaction. The potential scan rate was 50 mV s^{-1} . Unless otherwise noted, the peak power, average power and per-cycle energy were measured using an external load resistor that maximized the average power. These metrics were normalized with respect to the weight of the energy-harvesting CNTs in the harvester. The 0% strain for length direction harvesting is defined as the minimum strain that prevents yarn snarling. The potential of zero charge was measured using piezoelectrochemical spectroscopy¹³.

Data availability

All of the data generated in this study are included in the published Article and its Supplementary Information.

References

- Zi, Y. et al. Harvesting low-frequency (<5 Hz) irregular mechanical energy: a possible killer application of triboelectric nanogenerator. *ACS Nano* **10**, 4797–4805 (2016).
- Zhang, C., Tang, W., Han, C., Fan, F. & Wang, Z. L. Theoretical comparison, equivalent transformation, and conjunction operations of electromagnetic induction generator and triboelectric nanogenerator for harvesting mechanical energy. *Adv. Mater.* **26**, 3580–3591 (2014).
- Gabris, M. A. & Ping, J. Carbon nanomaterial-based nanogenerators for harvesting energy from environment. *Nano Energy* **90**, 106494 (2021).
- Xu, C., Song, Y., Han, M. & Zhang, H. Portable and wearable self-powered systems based on emerging energy harvesting technology. *Microsyst. Nanoeng.* **7**, 25 (2021).
- Li, Y. et al. Improved output performance of triboelectric nanogenerator by fast accumulation process of surface charges. *Adv. Energy Mater.* **11**, 2100050 (2021).
- Salaudin, M. et al. A novel MXene/Ecoflex nanocomposite-coated fabric as a highly negative and stable friction layer for high-output triboelectric nanogenerators. *Adv. Energy Mater.* **11**, 2002832 (2021).
- Gong, W. et al. Continuous and scalable manufacture of amphibious energy yarns and textiles. *Nat. Commun.* **10**, 868 (2019).
- Espinosa, H. D., Bernal, R. A. & Minary-Jolandan, M. A review of mechanical and electromechanical properties of piezoelectric nanowires. *Adv. Mater.* **24**, 4656–4675 (2012).
- Cha, S. et al. Porous PVDF as effective sonic wave driven nanogenerators. *Nano Lett.* **11**, 5142–5147 (2011).
- Jiang, Y. et al. Optimizing energy harvesting performance of cone dielectric elastomer generator based on VHB elastomer. *Nano Energy* **71**, 104606 (2020).
- Huang, J., Shian, S., Suo, Z. & Clarke, D. R. Maximizing the energy density of dielectric elastomer generators using equi-biaxial loading. *Adv. Funct. Mater.* **23**, 5056–5061 (2013).
- Zhang, M. et al. Self-powered, electrochemical carbon nanotube pressure sensors for wave monitoring. *Adv. Funct. Mater.* **30**, 2004564 (2020).
- Kim, S. H. et al. Harvesting electrical energy from carbon nanotube yarn twist. *Science* **357**, 773–778 (2017).
- Mun, T. J. et al. Wearable energy generating and storing textile based on carbon nanotube yarns. *Adv. Funct. Mater.* **30**, 2000411 (2020).
- Jang, Y. et al. Self-powered coiled carbon-nanotube yarn sensor for gastric electronics. *ACS Sens.* **4**, 2893–2899 (2019).
- Kim, S. et al. Electrochemically driven mechanical energy harvesting. *Nat. Commun.* **7**, 10146 (2016).
- Moon, J. K., Jeong, J., Lee, D. & Pak, H. K. Electrical power generation by mechanically modulating electrical double layers. *Nat. Commun.* **4**, 1487 (2013).
- Zhang, Y. et al. Micro electrostatic energy harvester with both broad bandwidth and high normalized power density. *Appl. Energy* **212**, 362–371 (2018).
- Xu, Y. et al. A one-dimensional fluidic nanogenerator with a high power conversion efficiency. *Angew. Chem. Int. Ed.* **56**, 12940–12945 (2017).
- Liu, J., Dai, L. & Baur, J. W. Multiwalled carbon nanotubes for flow-induced voltage generation. *J. Appl. Phys.* **101**, 64312 (2007).
- Zhang, Z. et al. Emerging hydrovoltaic technology. *Nat. Nanotechnol.* **13**, 1109–1119 (2018).
- Xue, G. et al. Water-evaporation-induced electricity with nanostructured carbon materials. *Nat. Nanotechnol.* **12**, 317–321 (2017).
- Li, M. et al. Gel-electrolyte-coated carbon nanotube yarns for self-powered and knittable piezoelectric sensors. *ACS Appl. Electron. Mater.* **3**, 944–954 (2021).
- Wang, Z. et al. More powerful twistron carbon nanotube yarn mechanical energy harvesters. *Adv. Mater.* **34**, 2201826 (2022).
- Nurazzi, N. M. et al. Treatments of natural fiber as reinforcement in polymer composites—a short review. *Funct. Compos. Struct.* **3**, 24002 (2021).
- Jung, W. et al. High output piezo/triboelectric hybrid generator. *Sci. Rep.* **5**, 9309 (2015).
- Inoue, H. et al. The critical role of the forest morphology for dry drawability of few-walled carbon nanotubes. *Carbon* **158**, 662–671 (2020).
- Xu, M., Futaba, D. N., Yumura, M. & Hata, K. Alignment control of carbon nanotube forest from random to nearly perfectly aligned by utilizing the crowding effect. *ACS Nano* **6**, 5837–5844 (2012).
- Zhu, J. et al. The effect of various electrolyte cations on electrochemical performance of polypyrrole/RGO based supercapacitors. *Phys. Chem. Chem. Phys.* **17**, 28666–28673 (2015).
- Taylor, L. W. et al. Improved properties, increased production, and the path to broad adoption of carbon nanotube fibers. *Carbon* **171**, 689–694 (2021).
- Kang, M. G. et al. High power magnetic field energy harvesting through amplified magneto-mechanical vibration. *Adv. Energy Mater.* **8**, 1703313 (2018).
- Ye, C. et al. A triboelectric–electromagnetic hybrid nanogenerator with broadband working range for wind energy harvesting and a self-powered wind speed sensor. *ACS Energy Lett.* **6**, 1443–1452 (2021).
- Xie, Y. et al. Grating-structured freestanding triboelectric-layer nanogenerator for harvesting mechanical energy at 85% total conversion efficiency. *Adv. Mater.* **26**, 6599–6607 (2014).
- Zhang, M., Atkinson, K. R. & Baughman, R. H. Multifunctional carbon nanotube yarns by downsizing an ancient technology. *Science* **306**, 1358–1361 (2004).
- Baughman, R. H., Stafstrom, S., Cui, C. & Dantas, S. O. Materials with negative compressibilities in one or more dimensions. *Science* **279**, 1522–1524 (1998).
- Kong, J. et al. Temperature dependence of ion diffusion coefficients in NaCl electrolyte confined within graphene nanochannels. *Phys. Chem. Chem. Phys.* **19**, 7678–7688 (2017).
- Kim, D. et al. High-performance nanopattern triboelectric generator by block copolymer lithography. *Nano Energy* **12**, 331–338 (2015).

Acknowledgements

Support in the United States was from Navy grants ONR/STTR N68335-18-C-0368 (R.H.B.) and ONR N00014-22-1-2569 (R.H.B.), Air Force Office of Scientific Research grants N68335-19C-0303 (R.H.B.) and FA9550-21-1-0455 (R.H.B.), Robert A. Welch Foundation grant AT-0029 (R.H.B.), National Science Foundation grant CMMI-1636306 (H.L.) and Department of Energy grant DE-NA0003962 (H.L.).

Author contributions

M.Z. and R.H.B. conceived of and initiated the project. C.H. synthesized the CNT forests. M.Z., W.C., Z.W., S.F., A.E.A., A.A.Z., J.O., J.H.M., J.W.P. and S.J.K. fabricated the CNT yarns and measured their performance. M.Z., W.C., S.F. and C.H. characterized the microstructure of the CNT yarns. M.Z., W.C., S.F., R.Z., H.L., E.G. and R.H.B. conducted the X-ray tomography characterization. M.Z., W.C., Z.W., S.F., A.E.A. and R.H.B. demonstrated the applications of CNT

yarns. All authors conducted the data analysis and prepared the manuscript.

Competing interests

Z.W., R.H.B., M.Z., W.C., S.F., S.J.K. and J.H.M. are among the inventors of provisional US patent application number 63/235,023, submitted jointly by the Board of Regents, University of Texas System (for the University of Texas at Dallas) and Industry-University Cooperation Foundation of Hanyang University, which covers the design, fabrication, performance and applications of twistron mechanical energy harvesters. The remaining authors declare no competing interests.

Additional information

Supplementary information The online version contains supplementary material available at <https://doi.org/10.1038/s41560-022-01191-7>.

Correspondence and requests for materials should be addressed to Ray H. Baughman.

Peer review information *Nature Energy* thanks Soo Jin Adrian Koh and the other, anonymous, reviewer(s) for their contribution to the peer review of this work.

Reprints and permissions information is available at www.nature.com/reprints.

Publisher's note Springer Nature remains neutral with regard to jurisdictional claims in published maps and institutional affiliations.

Springer Nature or its licensor (e.g. a society or other partner) holds exclusive rights to this article under a publishing agreement with the author(s) or other rightsholder(s); author self-archiving of the accepted manuscript version of this article is solely governed by the terms of such publishing agreement and applicable law.

© The Author(s), under exclusive licence to Springer Nature Limited 2023

Mechanical energy harvesters with tensile efficiency of 17.4% and torsional efficiency of 22.4% based on homochirally plied carbon nanotube yarns

In the format provided by the authors and unedited

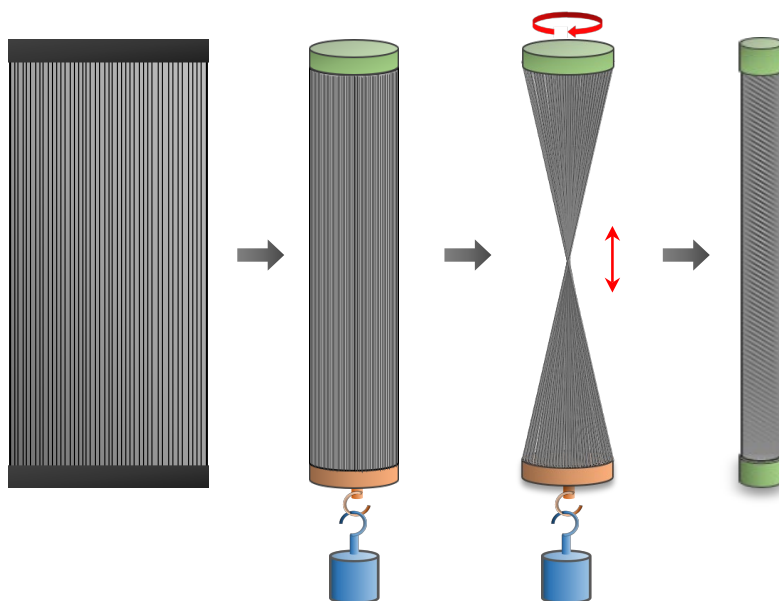
Supporting Information

This PDF file includes:

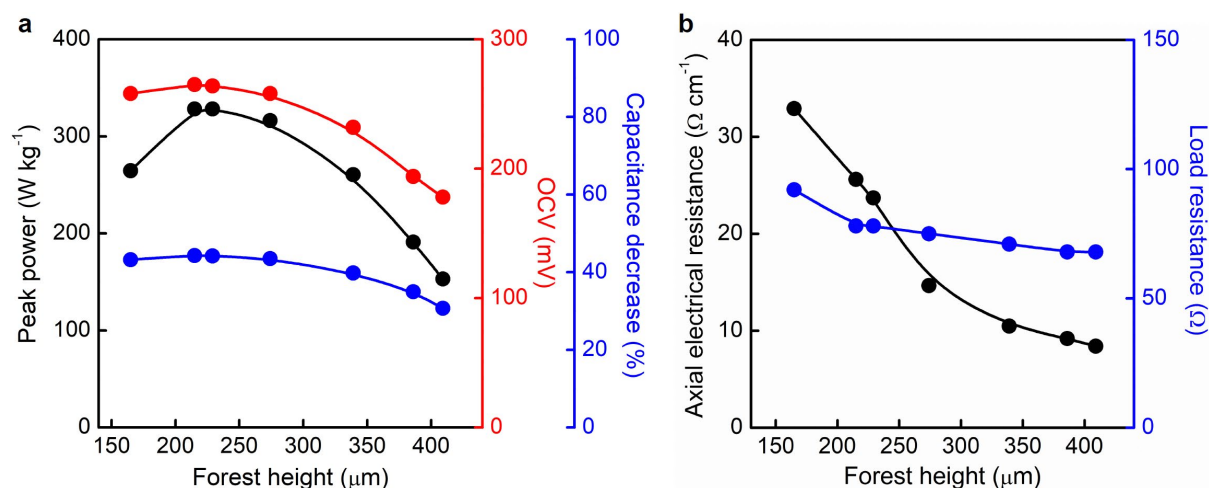
Figures S1 to S61

Tables S1 and S2

References (S1 to S90)

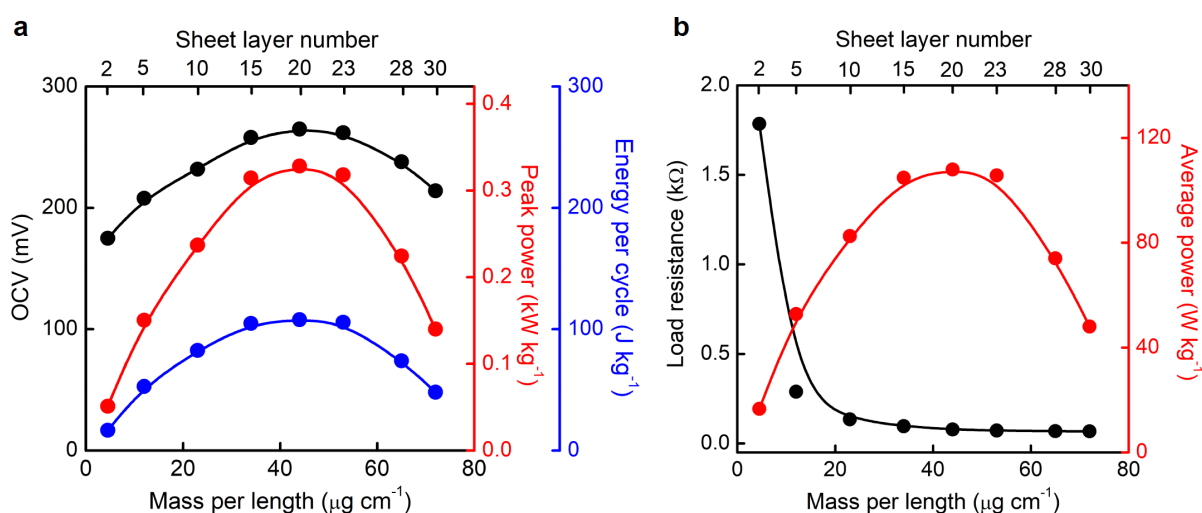


Supplementary Figure 1. The cone spinning method for fabricating twisted yarns. Illustration of carbon nanotube (CNT) yarn twist insertion by cone spinning¹.



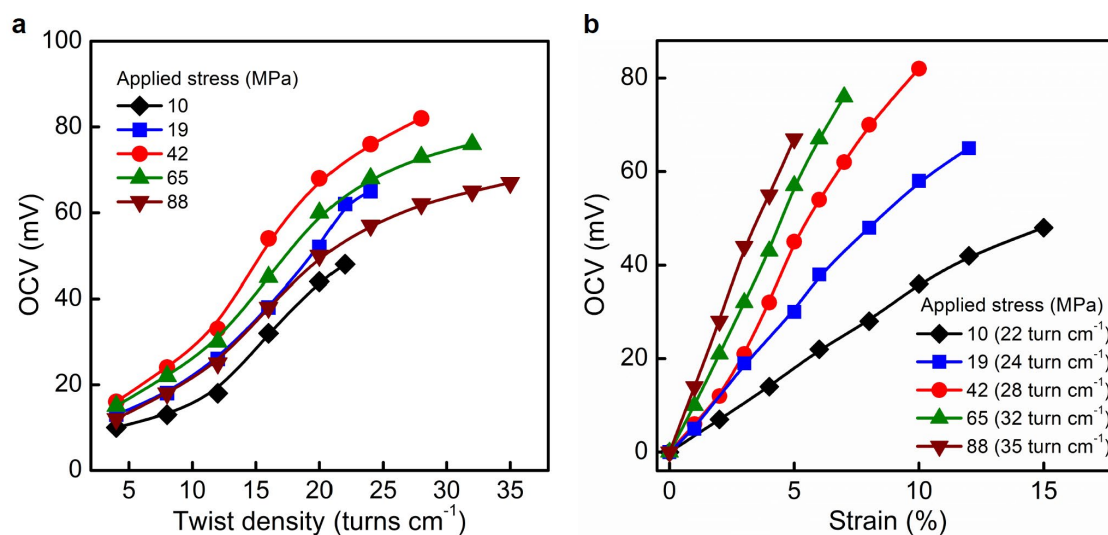
Supplementary Figure 2. The dependence of 3-ply, homochiral yarn harvesting on the height of the CNT forest used for fabricating the precursor twisted CNT yarns. **a**, The dependence of peak power, open-circuit voltage (OCV), and capacitance decrease for 3-ply yarn harvesters on the height of the CNT forest used for fabricating the precursor twisted CNT yarns that are plied. **b**, The forest-height dependence of yarn-direction electrical resistance and the load resistance that maximizes the average output power for 3-ply yarn harvesters. The harvesters were sinusoidally stretched to 40% strain at 1 Hz in 0.1 M aqueous HCl electrolyte. Supplementary Fig. 2 shows that the performance of 3-ply twistron harvesters depends on the height of the forest used for making the precursor twisted yarns. This dependence results from the method used for varying forest height, which is by changing the forest growth time. The forest height should not be too high, since the number of propagating CNTs decreases with increasing forest growth time and this decreases forest density and forest alignment^{2,3}. These effects should decrease the Herman's orientation

factor (HOF) of the forest-drawn sheets and derived CNT yarns, thereby decreasing the inter-bundle double layer interactions that provide harvesting⁴. This height should also not be too low, since Supplementary Fig. 2b shows that the harvester's resistance increases for forest heights below about 200 μm . Because of these considerations, a forest height of 220 μm was used for harvester fabrication. In this work, the described twistrans used forests of approximately 9-nm-diameter MWNTs that had about 6 layers, which were grown by using the referenced chemical vapor deposition (CVD) method. Since use of few-walled nanotubes (FWNTs) increased nanotube bundling, which decreased capacitance and mechanically-induced capacitance changes, we found no benefit in transiting from these MWNTs to the more difficulty produced FWNT forests. As an alternative to CVD, we also investigated the floating catalyst CVD method of Windle (FCCVD) for the production of coiled MWNT yarns. Without synthesis or process optimization, these FCCVD yarns drawn from a FCCVD aerogel provided a gravimetric peak power and average power of about 1/3 that of those obtained by mechanical drawn from a CVD produced forest. This result, when improved by yarn density and alignment optimization, might be commercially important, since the FCCVD CNTs might be cheaper to produce than CVD-grown CNT forests. We also investigated for twistrans harvesting a CNT yarn made by the solution spinning method of Pasquali. While these solution-spun yarns provided extremely high strength and conductivity due to their high CNT alignment, CNT bundling that resulted from this high alignment dramatically reduced electrochemical capacitance to about 50 mF g^{-1} . Hence, very low twistrans harvesting resulted.

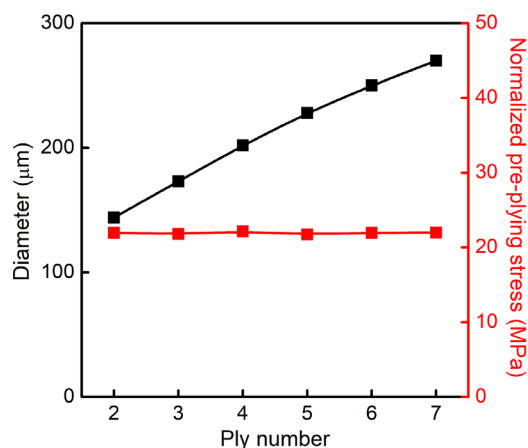


Supplementary Figure 3. The dependence of harvesting performance of 3-ply yarn harvesters on the mass per length of stacked sheets drawn from forests. (a) The dependencies of OCV, peak power, and energy per cycle and (b) the average power optimizing load resistance and the average power for 3-ply yarn harvesters on the mass per length of the forest-drawn CNT sheets stack and the number of CNT sheets in the stack that were used for fabricating the plied yarns. These results, which are for twistrans prepared using optimized conditions for pre-plying twist insertion and plying, were obtained by stretching the 3-ply harvesters by 40% at 1 Hz in 0.1 M HCl electrolyte. The number of CNT sheet layers and the width of the component forest-drawn CNT sheets used for cone spinning were chosen to maximize the output power and

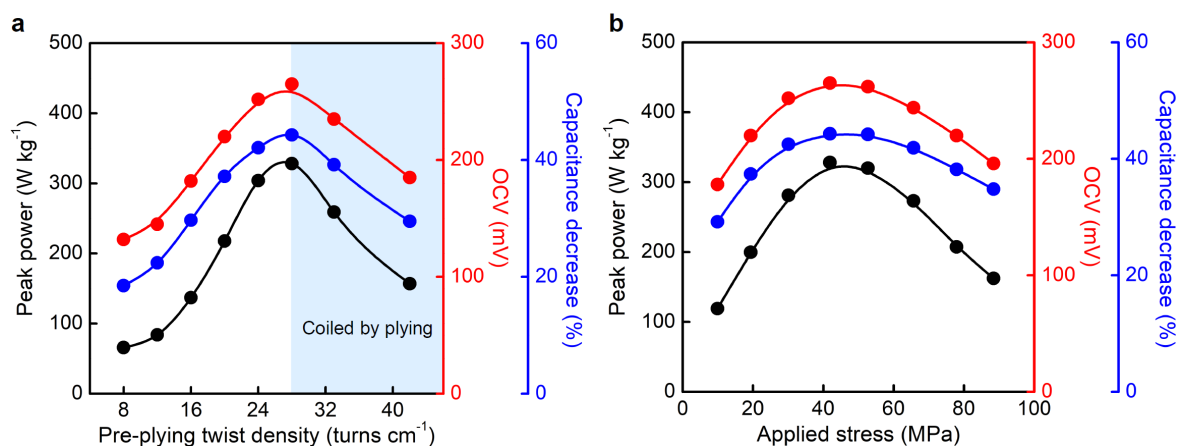
energy per cycle for the 3-ply yarn harvesters. For optimizing performance, a stack of 15 to 20 layers of about 20-mm-wide sheet ribbons (having a mass-per-length of about $44 \mu\text{g cm}^{-1}$) was formed into an approximately 6.6-mm-diameter cylinder for cone-spinning of the twisted yarns.



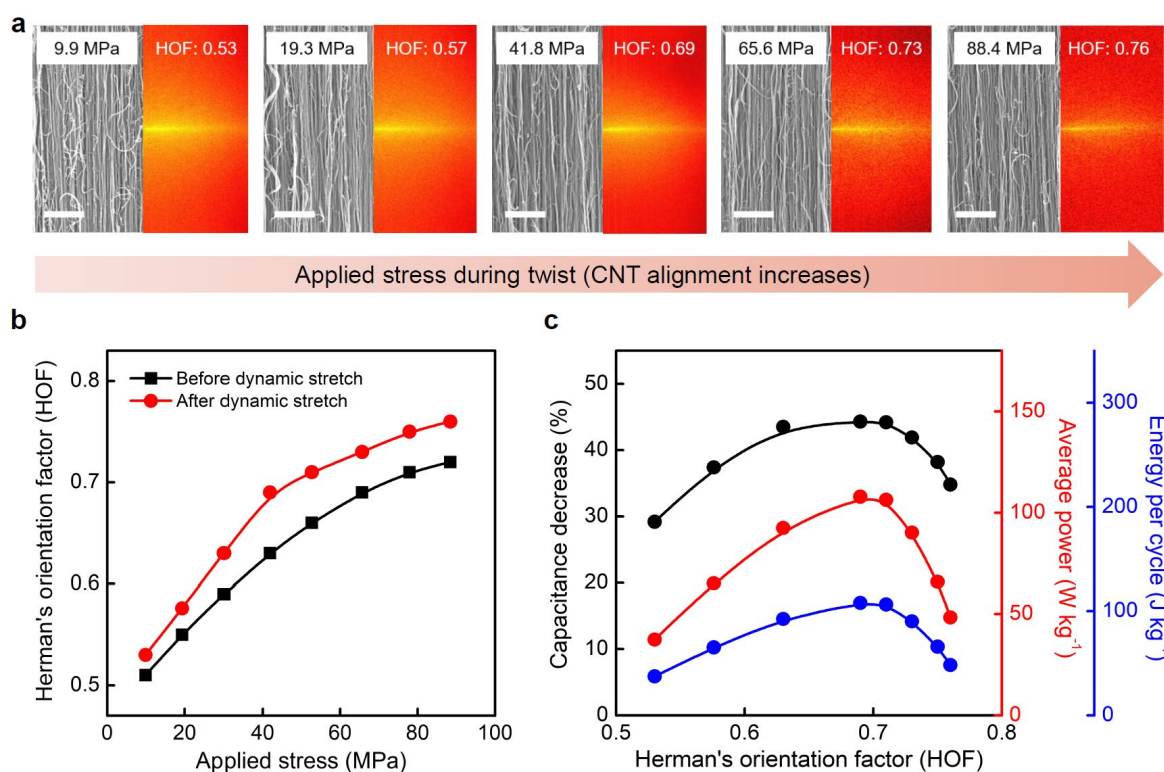
Supplementary Figure 4. The dependence of the OCV of non-plyed, non-coiled twisted yarns on twist density and stretch strain. a, The OCV obtained by stretching twisted, non-plyed, non-coiled twistrans to the maximum pre-failure strain, as a function of the twist density and stress used for fabricating the twisted yarn. The last data point in each curve corresponds to the maximum pre-coiling twist density. **b,** The tensile strain dependence of the OCV obtained by stretching the twistrans of (a) that had the maximum pre-coiling inserted twist for different applied stresses. Supplementary Fig. 4a shows the OCV reached the maximum when the yarn twist density was just below the onset of coiling for each applied stress during yarn twist. By using an applied stress of 42 MPa during yarn twist, the resulting yarn with a twist density of 28 turns cm^{-1} provided the highest OCV when stretched to maximum strain. Supplementary Fig. 4b shows the tensile strain dependence of OCV for yarns that were twist inserted to immediately below the onset of coiling, while different stresses were applied. When the applied stress during yarn twist increased from 10 to 88 MPa, the maximum stretch of the twisted yarns decreased from 15% to 5%. The OCV was maximized for a yarn that was twisted by 28 turns cm^{-1} , while under an applied stress of 42 MPa. For maximizing the OCV of 3-ply yarn harvesters, twisted yarns with 28 turns cm^{-1} were plied for the fabrication of optimized-ply-structure (OPS) twistrans.



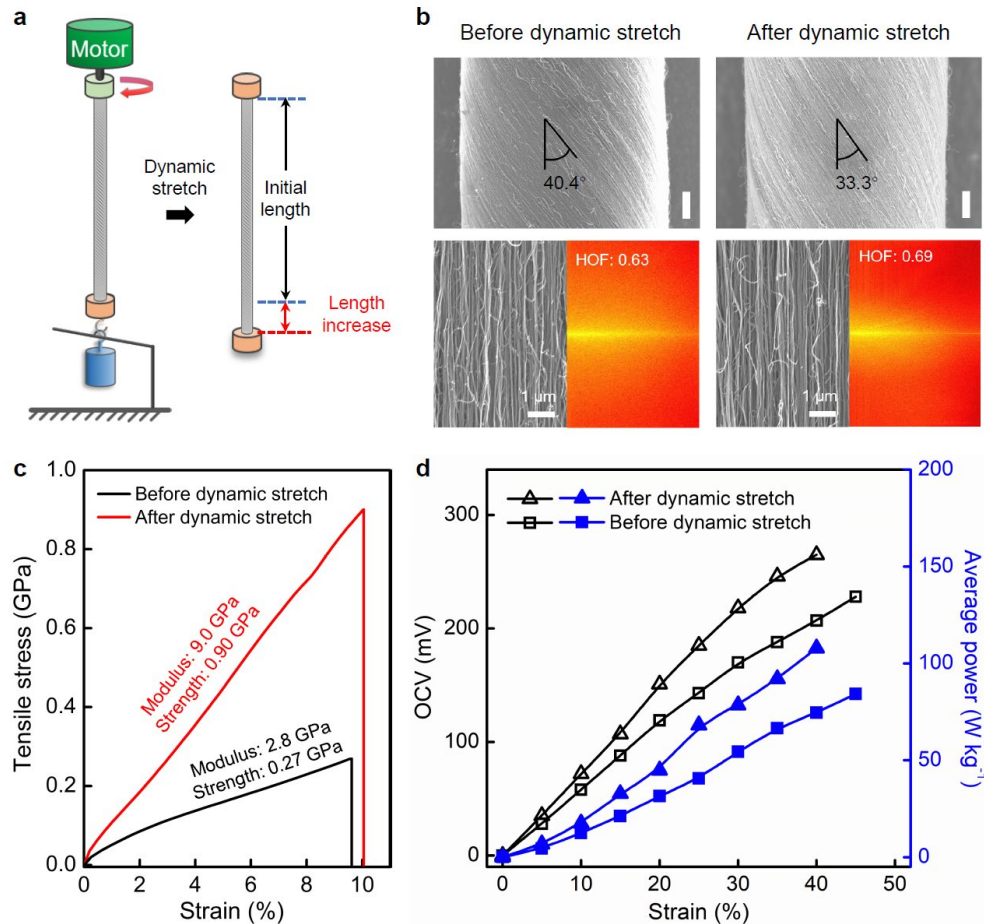
Supplementary Figure 5. For homochiral plied yarn fabrication, the dependence of the isobaric tensile stress used for plying and the final plied yarn outer diameter on the number of plied yarns. For all experiments, the same pre-plying stress was applied during isobaric twist insertion to make the yarns that are plied (about 22 MPa, when normalized using the area calculated from the final twisted yarn diameter, 90 µm).



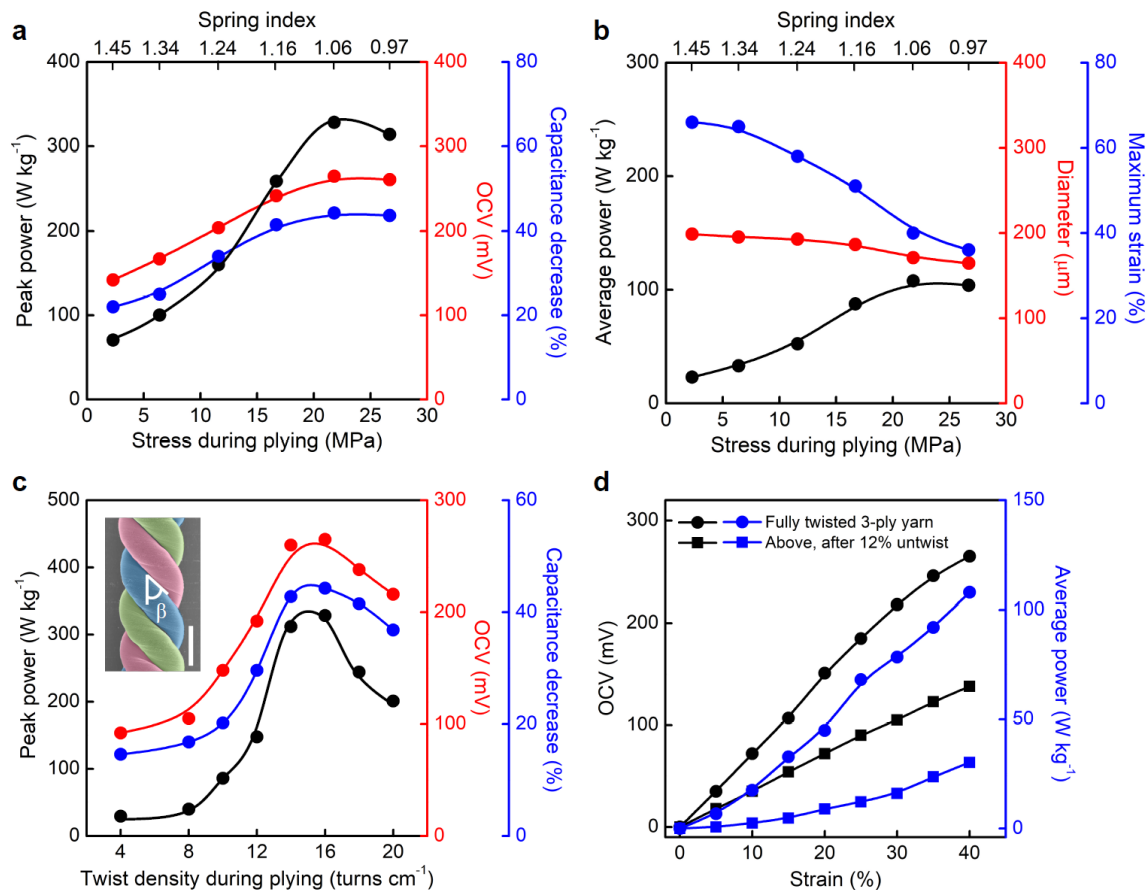
Supplementary Figure 6. The dependence of the harvesting performance of 3-ply yarn harvesters on pre-plying twist density and applied stress during twist (before plying). For a 1 Hz sinusoidal stretch to the maximum reversible strain, the dependencies of peak power, OCV, and capacitance decrease of 3-ply yarn harvesters on (a) the twist density of the yarns being plied and (b) the applied stress during pre-plying twist insertion. The 3-ply yarns were made by using the optimized conditions for plying: an applied stress of 22 MPa and a twist of plying that was just below the twist required for coiling the plied yarn. Supplementary Fig. 6 shows that the OCV and peak power of 3-ply yarn harvesters in 0.1 M HCl aqueous electrolyte were optimized when an applied stress of 42 MPa and a corresponding pre-coiling twist density of 28 turns cm⁻¹ were used for making the precursor twisted yarns.



Supplementary Figure 7. The optimization of CNT alignment (Herman's orientation factor) during individual yarn twist. **a**, Relevant for understanding the effects of the stress used for precursor twisted yarn preparation on the structure and performance of 3-ply twistrans, scanning electron microscope (SEM) images (scale bar: 2 μm) and corresponding fast Fourier transforms (FFT) of twisted yarns made using different applied stress during twist insertion. **b**, The HOF of the precursor yarns made using different applied stresses, when measured before and after dynamic stretching. **c**, The capacitance decrease, output average power, and energy per cycle for 3-ply yarn harvesters that were sinusoidally stretched at 1 Hz to maximum reversible strain, as a function of the HOF of the precursor dynamically cycled twisted yarn. Supplementary Fig. 7 shows that the performance of 3-ply twistrans depends upon the HOF of the precursor twisted yarns, which increases after the dynamic stretch process. While the capacitance decrease, average power, and energy per cycle are maximized for a HOF of about 0.69, these performance metrics dramatically decrease for a higher HOF. This decrease is due to increased CNT bundling, which decreases the accessible electrochemical surface area and capacitance⁴.

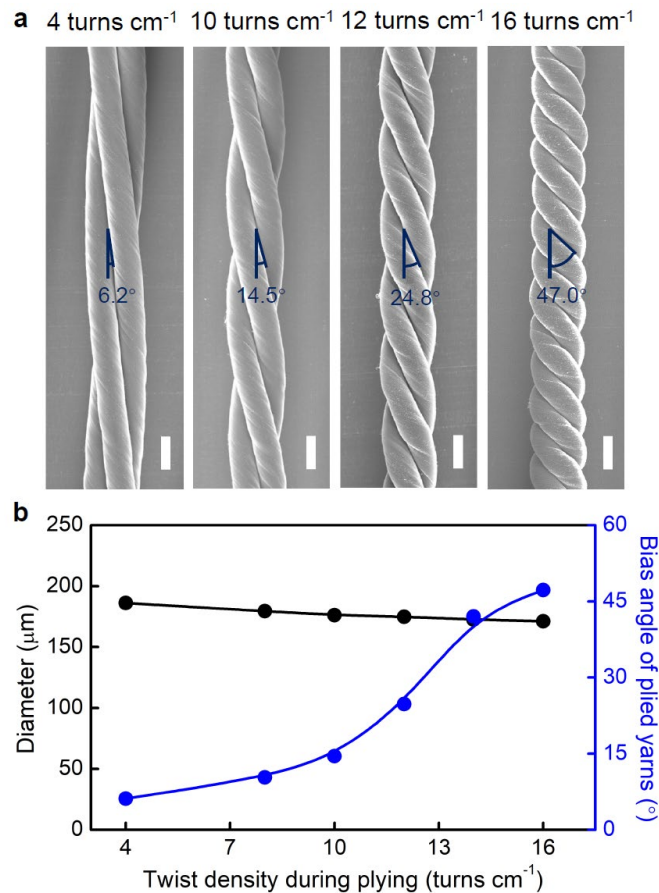


Supplementary Figure 8. The illustration, microstructures, and mechanical properties of twisted yarns before and after dynamic stretch, and the resulting harvester performance of plied yarns containing these twisted yarns. **a**, Illustration of the dynamic stretch process. **b**, Low-magnification SEM images (scale bars: 10 μm), high-magnification SEM images, and corresponding FFT images of a twisted yarn before and after dynamic stretch. **c**, Tensile stress-strain curves for a twisted yarn before and after the dynamic stretch process. **d**, The tensile strain dependence of OCV and average power for a 1 Hz, sinusoidal deformation of 3-ply yarn harvesters made by plying yarns that were either dynamically stretched or not dynamically stretched. Supplementary Fig. 8 provides information on the dynamic stretch process and its effect on the precursor twisted yarns used for making harvesters. During the dynamic stretch process, a twisted yarn was stretched at 1 Hz to near the maximum pre-failure strain for about 30 cycles, during which the pre-failure strain increased to about 10%. This process increased tensile strength and modulus (Supplementary Fig. 8c), increased CNT alignment (Supplementary Fig. 8b), and partially stabilized the yarn against untwist. More specifically, this process increased the failure stress to 0.90 GPa and the modulus to 9.0 GPa, compared to the initial 0.27 and 2.8 GPa, respectively, but caused little change in the failure strain. In addition, the harvesting performance for 3-ply yarn harvester was increased when the precursor twisted yarns underwent dynamic stretch (Supplementary Fig. 8d).

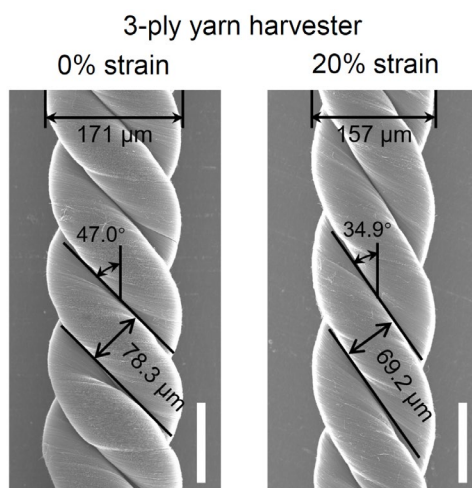


Supplementary Figure 9. Using optimized pre-plying fabrication, the dependence of harvester performance on plying conditions and resulting spring index when sinusoidally stretching 3-ply yarn harvesters at 1 Hz to the maximum reversible strain, or to an indicated strain, in 0.1 M HCl electrolyte. a, The dependencies of peak power, OCV, and capacitance decrease on the stress during plying and the resulting SEM-measured spring index. b, The dependencies of average power, plied yarn outer diameter, and maximum reversible strain on the stress applied during plying. c, The dependencies of peak power, OCV, and capacitance decrease on the twist density during plying using a 22 MPa stress. Inset: SEM image of a 3-ply yarn with a twist density of 16 turns cm^{-1} and a helix bias angle (β) of 47.0°, which is colored to show individual plies (scale bar, 100 μm). d, The tensile-strain dependence of the OCV and the average power for a 3-ply yarn harvester that had a twist of plying that was just below the plying twist that caused coiling, compared with that for a 3-ply yarn harvester in which 12% of plying twist was removed. The results for (a, b, d) are for plied yarns that were twisted to just below the plying twist that causes coiling and the results of (c), up to the peak in performance, were for non-coiled plied yarns. Thereafter, for higher twist that produced coiling, the performance metrics decreased. Supplementary Fig. 9a shows that 3-ply harvester performance was maximized when the stress applied during plying was 22 MPa and the inserted plying twist was just below the plying twist that initiates coiling. Using these optimized parameters, the 3-ply yarn harvester has a spring index of 1.06, a helix bias angle of 47.0°, and an outer diameter of 171 μm (Supplementary Fig. 9b). The data in Supplementary Fig. 9c shows that a lower or higher plying twist than the maximum pre-coiling twist decreases harvesting. Similarly, 5%, 8%, or 12% (Supplementary Fig. 9d) untwist of the plying twist

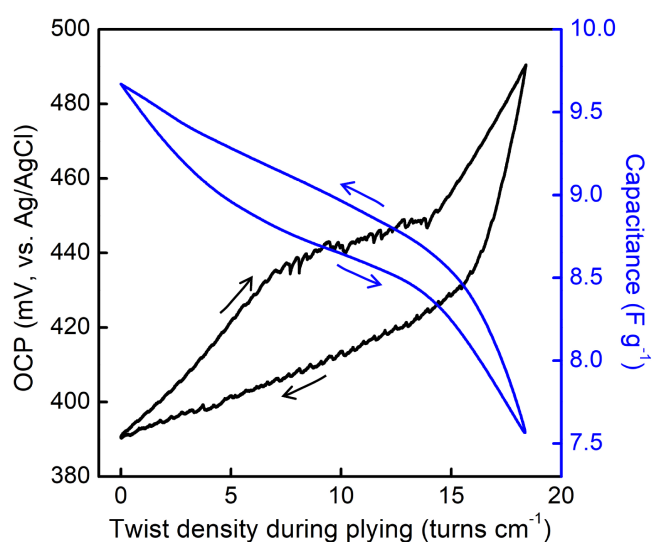
for a 3-ply yarn also degrades harvesting to an extent that increases with increasing untwist. These results contrast with those obtained by untwisting a fully coiled harvester, where partial removal of the twist of coiling results in an OCV and average power that are 1.4 times values obtained for the fully twisted coiled yarn¹.



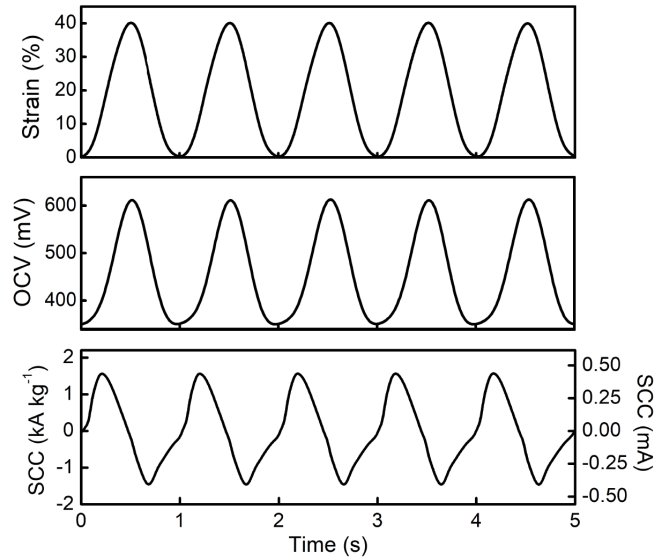
Supplementary Figure 10. The dependence of outer diameter and bias angle of 3-ply yarn harvesters on twist density during plying. **a**, SEM images during 3-ply homochiral plying to produce twist densities of plying of 4, 10, 12 and 16 turns cm⁻¹ (scale bar: 100 μm). **b**, The plied yarn outer diameter and helix bias angle as a function of the twist density of plying, for plying twist densities up to the twist density that initiates coiling of the plied yarn. The precursor twisted yarns had a diameter of 90 μm, a bias angle of 33.3°, and a twist density of 28 turns cm⁻¹. The SEM images and data of Supplementary Fig. 10 show that increasing the twist of plying decreases the diameter of a 3-ply yarn and increases the bias angle that component yarns make with the length direction of the plied yarn. When the twist density of plying was increased from 4 to 16 turns cm⁻¹, the outer diameter for the 3-ply yarn harvesters approximately linearly decreased from 186 to 171 μm and the helix bias angle increased from 6.2 to 47.0°.



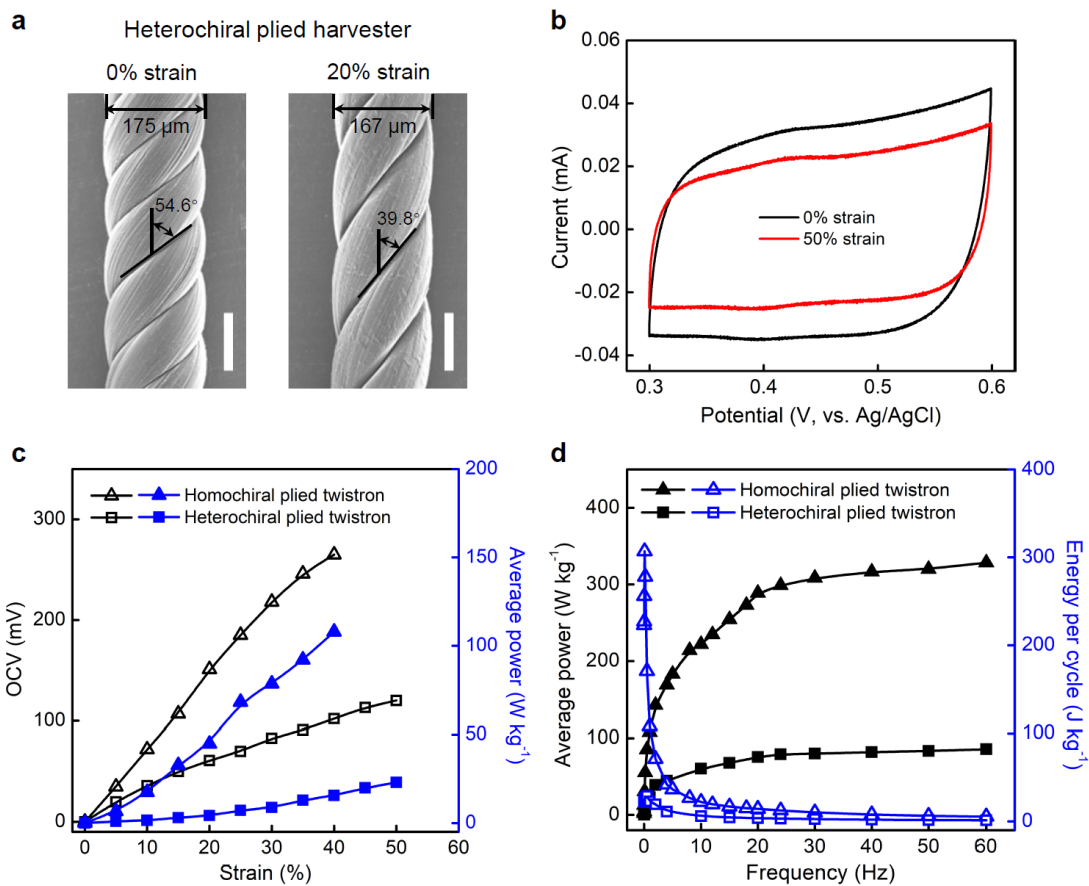
Supplementary Figure 11. Structure of an OPS harvester before and after stretch. SEM images of an OPS harvester that was either stretched only to the extent that yarn snarling was avoided (left) or stretched to a 20% higher strain (right). As a consequence of this stretch, the outer diameter of the plied yarn decreased from 171 to 157 μm (scale bar: 100 μm).



Supplementary Figure 12. The dependencies of the open-circuit potential (OCP) and capacitance on the twist inserted during homochirally plying three 90- μm -diameter twisted CNT yarns in 0.1 M aqueous HCl. The isobaric tensile stress applied during plying was 22 MPa and the speed of twist insertion and removal from the 4-cm-long yarn was 60 revolutions per minute (rpm).

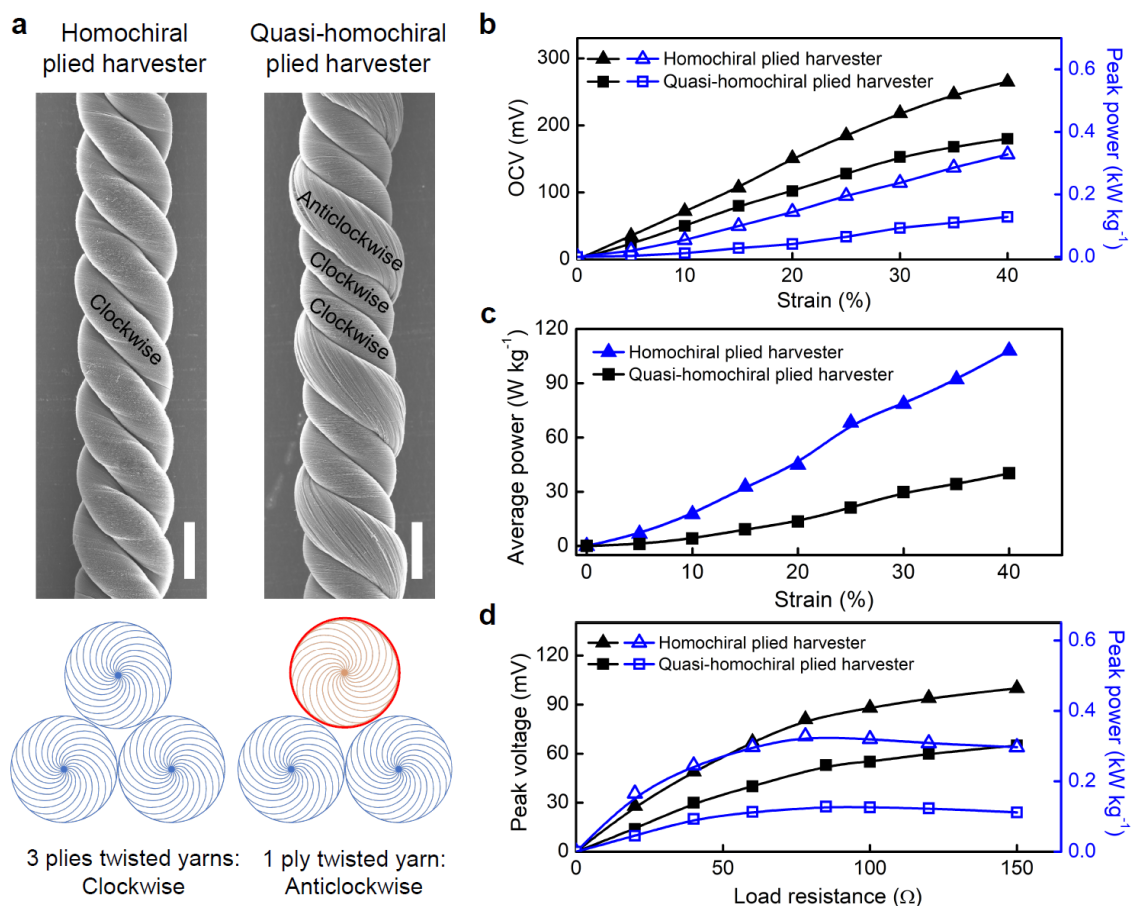


Supplementary Figure 13. The electrical response of an OPS harvester during sinusoidal tensile deformation. The time-dependencies of the tensile strain, the OCV, and the short-circuit current (SCC) of an OPS harvester when stretched sinusoidally to 40% strain at 1 Hz in 0.1 M HCl electrolyte.

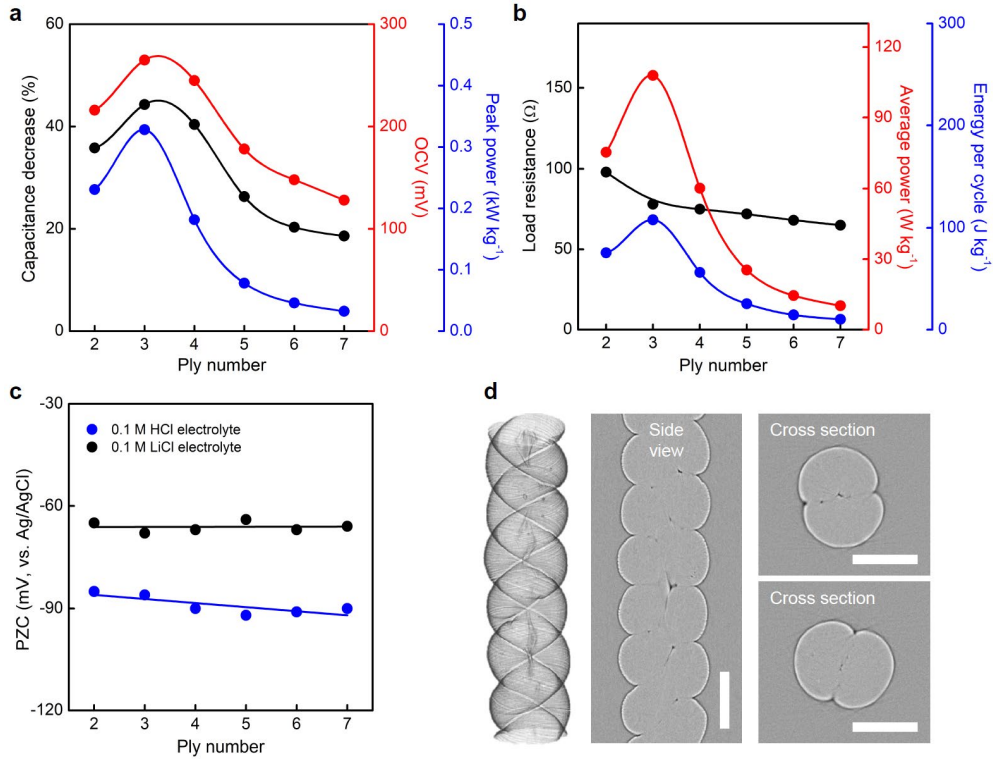


Supplementary Figure 14. The dependencies of structure, OCV, and average power on yarn chirality for 3-ply yarn harvesters. a, SEM images of a non-stretched and a 20% stretched heterochiral 3-ply yarn harvester (scale bar: 100 μm). Non-stretched means that only the strain needed to avoid snarling was applied.

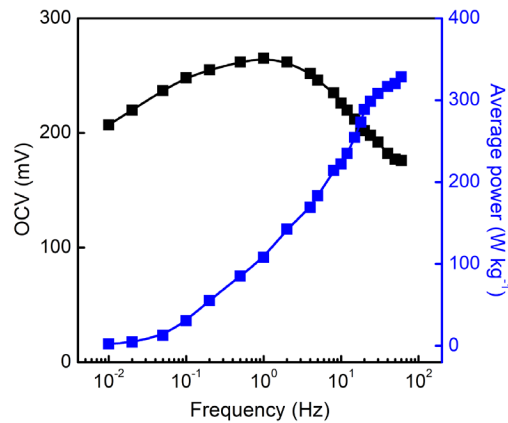
b, The capacitance curves of the heterochiral 3-ply yarn harvester for 0% and 50% tensile strain. **c**, The strain dependencies of OCV and average power for the homochiral plied harvester and the heterochiral plied harvester for a 1 Hz sinusoidal deformation. **d**, The dependencies of average power and energy per cycle on stretch frequency for 3-ply homochiral and heterochiral harvesters that were stretched to the maximum reversible strain. The electrolyte used was 0.1 M aqueous HCl. The results of Supplementary Fig. 14 show that, for any tensile strain or deformation frequency, 3-ply yarn harvesters provide much higher performance when they are homochiral than when they are heterochiral.



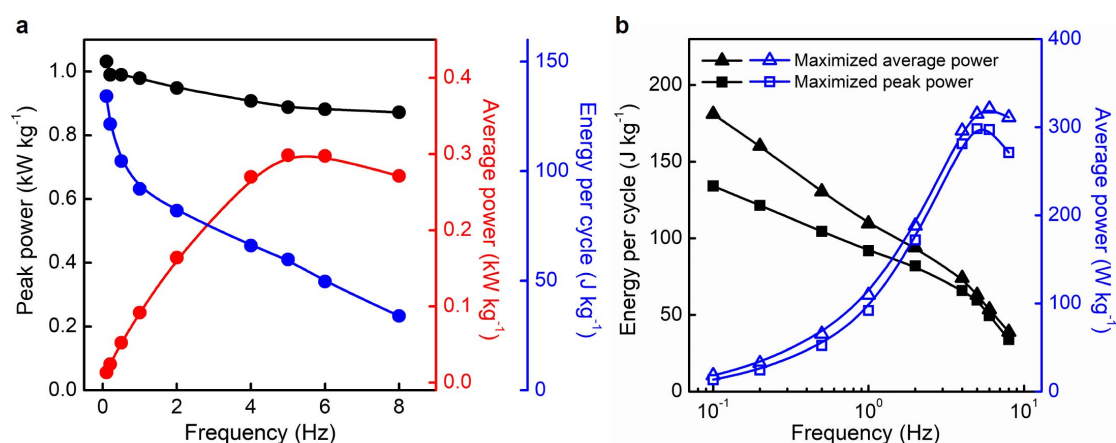
Supplementary Figure 15. The dependence of harvester performance on the relative chirality of plied yarns in a 3-ply yarn harvester that is operated in 0.1 M HCl electrolyte. a, SEM images (top, scale bar: 100 μm) and the twist configurations (bottom) for a homochiral plied harvester and a quasi-homochiral plied harvester in which one of the plied yarns has a different chirality than the other two plied yarns and the chirality of plying. Note that the surface-measured diameter of the anticlockwise twisted yarn is much larger than for the two yarns having the same twist direction as the plying twist. For the homochiral harvester and the quasi-homochiral harvester, the tensile strain dependence for a 1-Hz sinusoidal stretch, of **(b)** OCV and peak power and **(c)** average power. **d**, The peak voltage and peak power versus load resistance for the homochiral harvester and the quasi-homochiral harvester for a 40% sinusoidal stretch at 1 Hz.



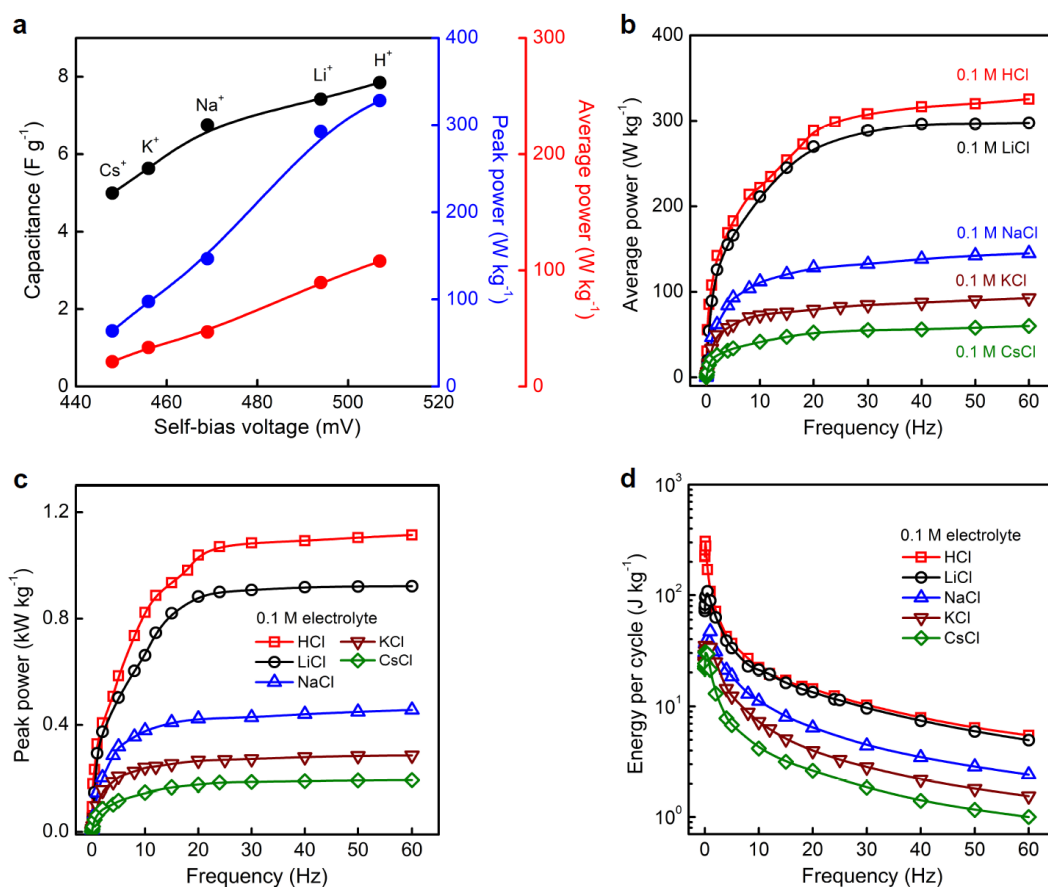
Supplementary Figure 16. Ply number optimization for maximizing harvesting performance. The ply number dependence of (a) the capacitance decrease, OCV, and peak power; (b) the average power, energy per cycle, and load resistance for maximizing average power and energy per cycle; and (c) the potential of zero charge (PZC). The harvesting was for sinusoidal stretch to maximum reversible strain at 1 Hz in a 0.1 M aqueous HCl electrolyte and the PZC measurements were in both 0.1 M aqueous HCl and 0.1 M LiCl electrolytes. d, X-ray tomography images (scale bar: 100 μm) for a non-stretched two-ply yarn harvester. The lateral compression is smaller when two yarns are plied than when three yarns are plied, which results in a smaller capacitance decrease and a lower power and energy output for the two-ply yarn harvester than the 3-ply yarn harvester (Supplementary Fig. 43).



Supplementary Figure 17. The frequency dependencies of OCV and average power for 40% sinusoidal strain of an OPS harvester in 0.1 M aqueous HCl electrolyte.

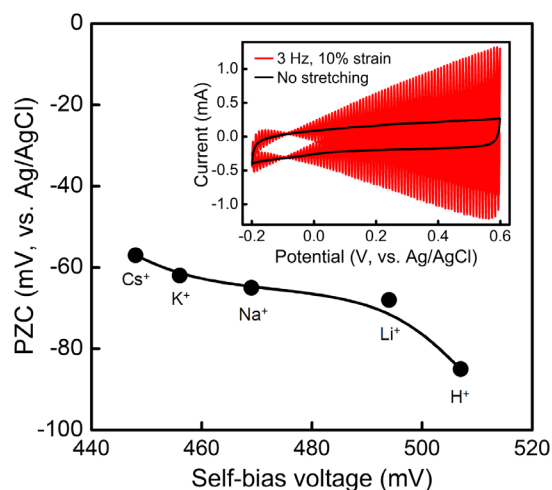


Supplementary Figure 18. The frequency dependencies of peak and average output power and energy per cycle for 40% strain of a Pt-wire-plied OPS harvester when stretched in 0.1 M aqueous HCl electrolyte using a square-wave deformation. **a**, The frequency dependencies of peak power, average power, and energy per cycle for an OPS harvester. The used load resistance maximized the peak power at the chosen frequency. **b**, The frequency dependencies of the energy per cycle and the average power for an OPS harvester when the used load resistance at each frequency maximized these quantities.

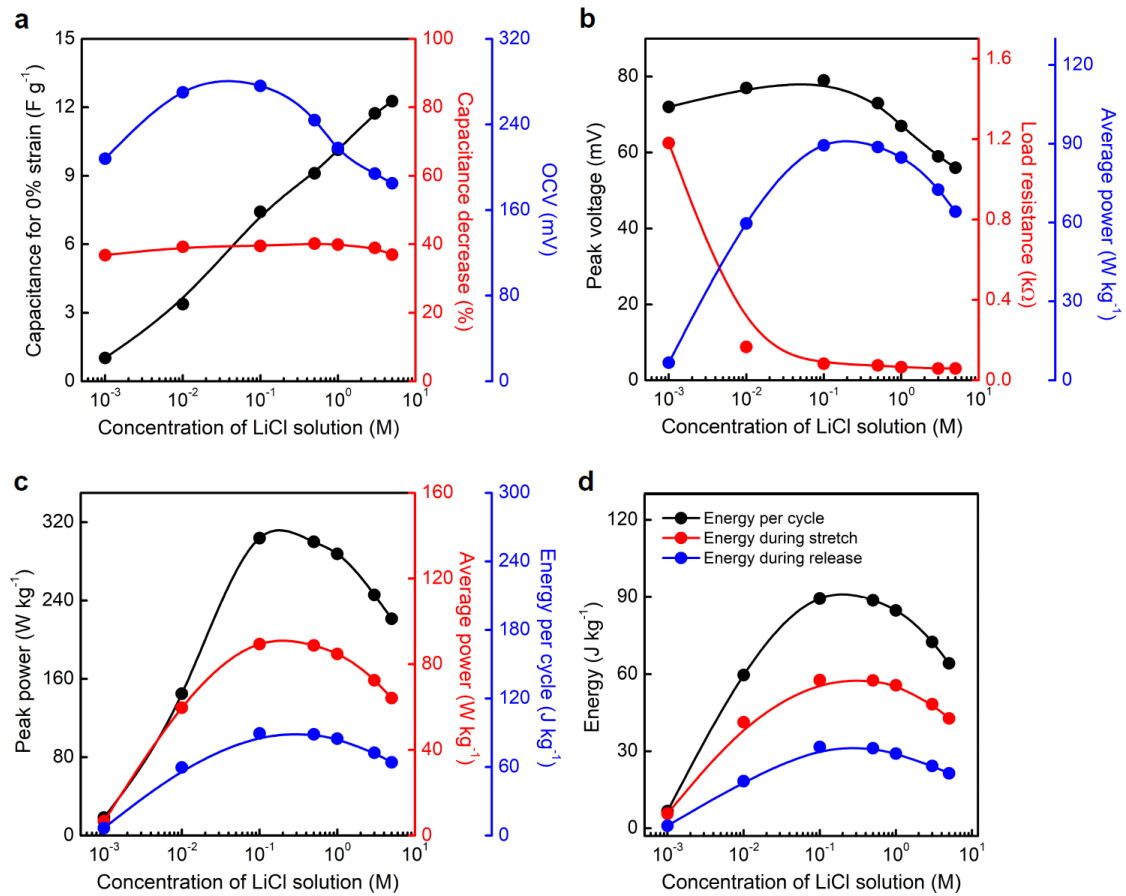


Supplementary Figure 19. The capacitance, peak power, and average power for OPS harvesters when sinusoidally stretched to 40% strain in aqueous chloride electrolytes having differing cation ionic radii.

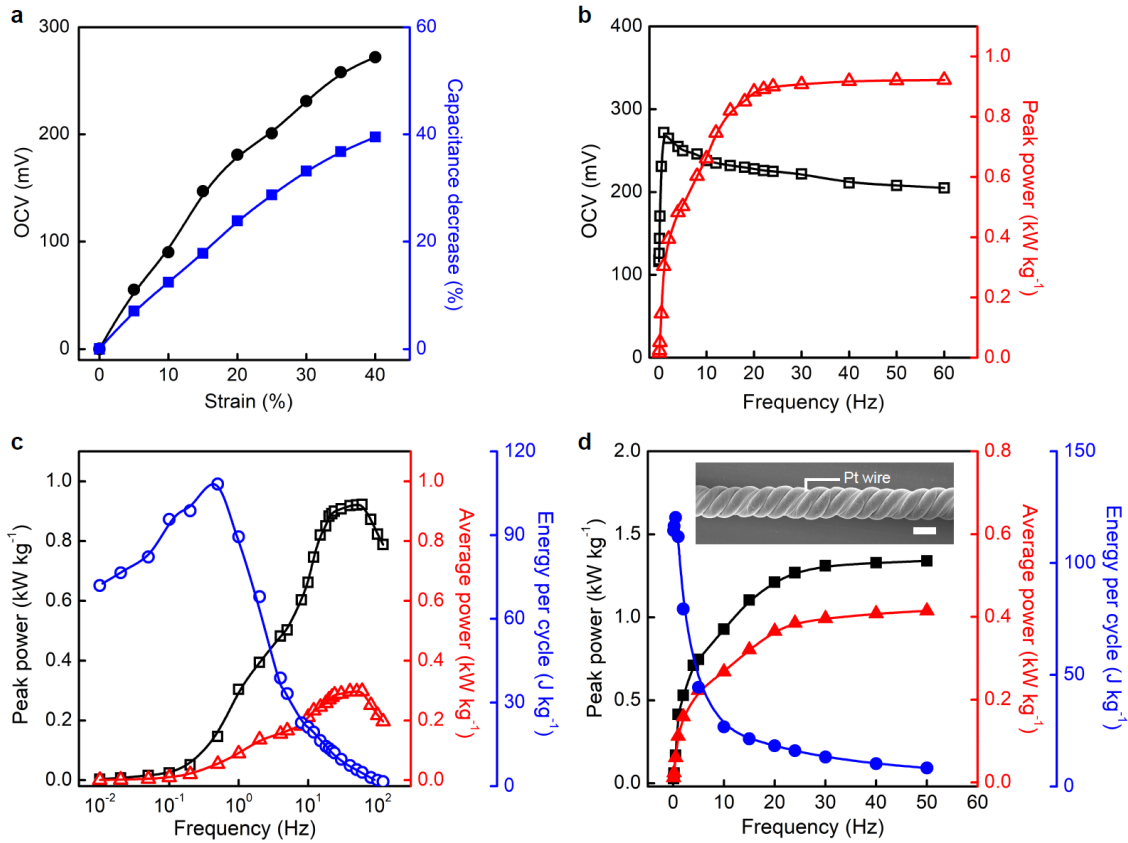
a, The self-bias voltage dependence of the capacitance for 0% strain and the peak power and average power for a 1 Hz deformation. The frequency dependencies of (b) average power, (c) peak power, and (d) energy per cycle for the OPS harvesters in 0.1 M aqueous electrolytes of HCl, LiCl, NaCl, KCl and CsCl.



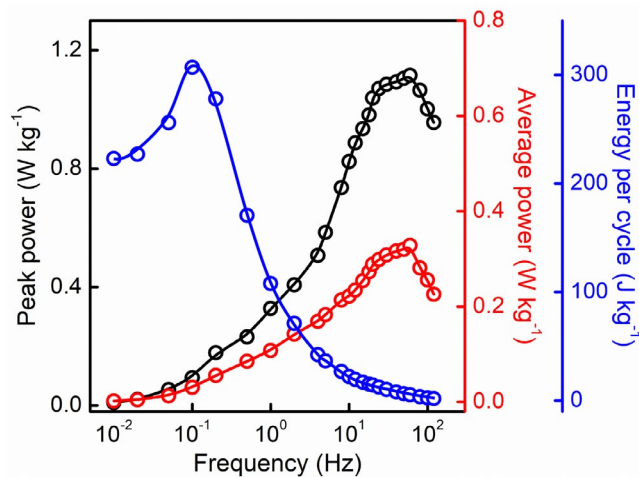
Supplementary Figure 20. PZC characterization for a 3-ply yarn harvester in aqueous chloride electrolytes having different ionic radii cations. The self-bias voltage dependence of the PZC of a 3-ply yarn harvester. Inset: Cyclic voltammograms (scan rate: 30 mV s⁻¹) with (red) and without (black) a 3-Hz applied sinusoidal stretch of 10% strain in 0.1 M HCl electrolyte. The values of PZC were measured using piezoelectrochemical spectroscopy¹.



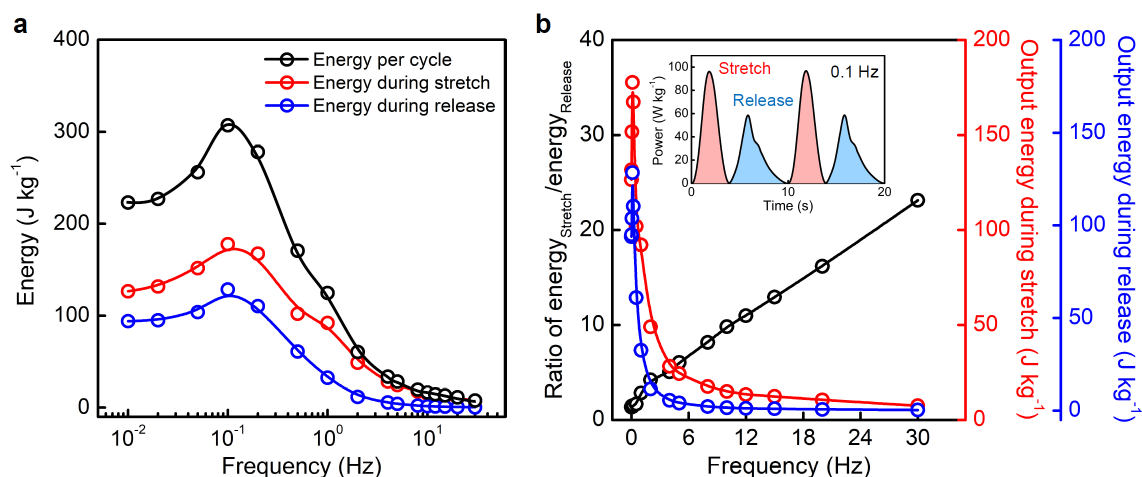
Supplementary Figure 21. The dependence of harvester performance on electrolyte concentration for a 1 Hz, 40% deformation of an OPS harvester in aqueous LiCl electrolyte. a, The concentration dependence of the capacitance for 0% strain, the stretch-produced capacitance decrease (%), and the OCV for the OPS harvester. **b,** The concentration dependencies of the peak voltage, the load resistance that maximizes the average power, and the average power. **c,** The concentration dependencies of the peak power, average power, and energy per cycle. **d,** The concentration dependencies of the energy per cycle, energy during stretch, and energy during release.



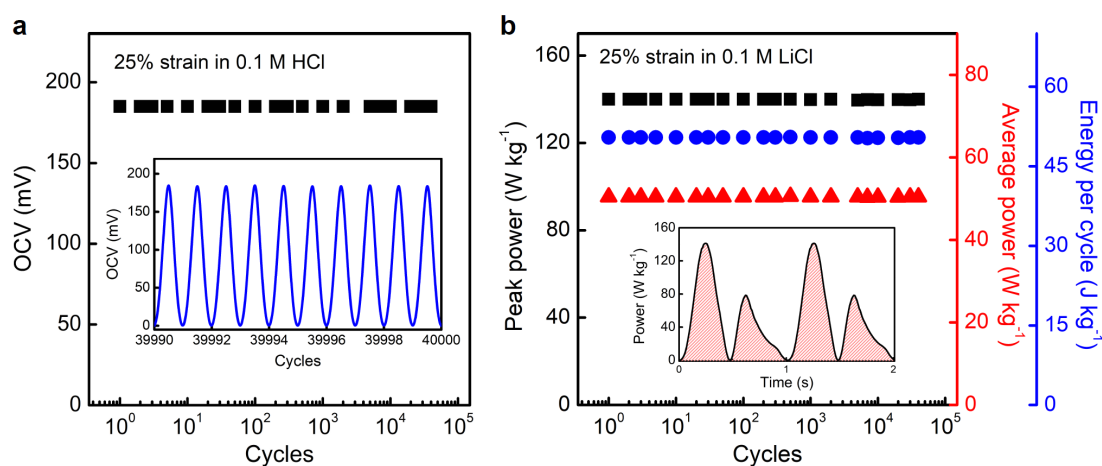
Supplementary Figure 22. The performance of an OPS harvester when sinusoidally stretched in 0.1 M aqueous LiCl electrolyte. a, The strain dependence of OCV and percent capacitance decrease for an OPS harvester stretched at 1 Hz. **b,** The frequency dependencies of OCV and peak power for 40% deformation. **c,** The log-scale frequency dependencies of peak power, average power, and energy per cycle for 40% deformation. **d,** The frequency dependencies of peak power, average power and energy per cycle for 40% sinusoidal strain of an OPS harvester containing a plied Pt wire. Inset: SEM image of a 3-ply yarn harvester with an incorporated 25- μm -diameter Pt wire (scale bar: 100 μm).



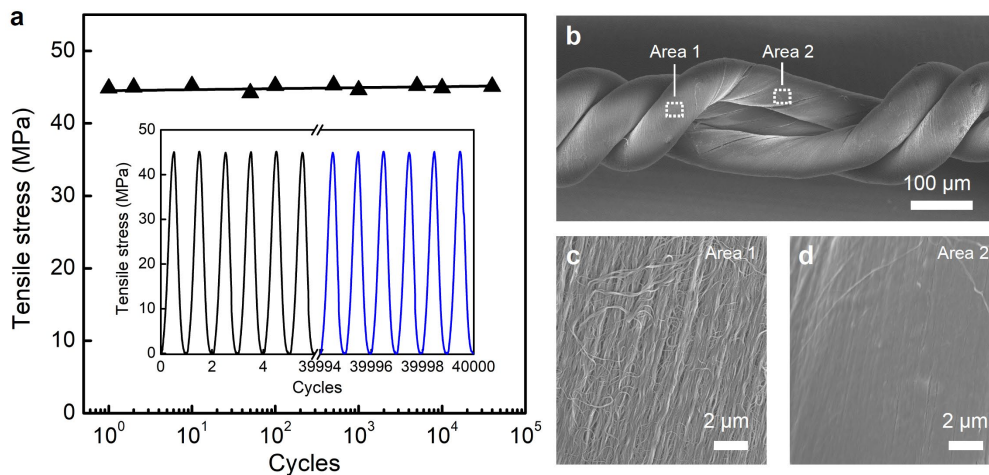
Supplementary Figure 23. The frequency dependencies of peak power, average power, and energy per cycle for an OPS harvester when stretched in 0.1 M aqueous HCl electrolyte to 40% strain.



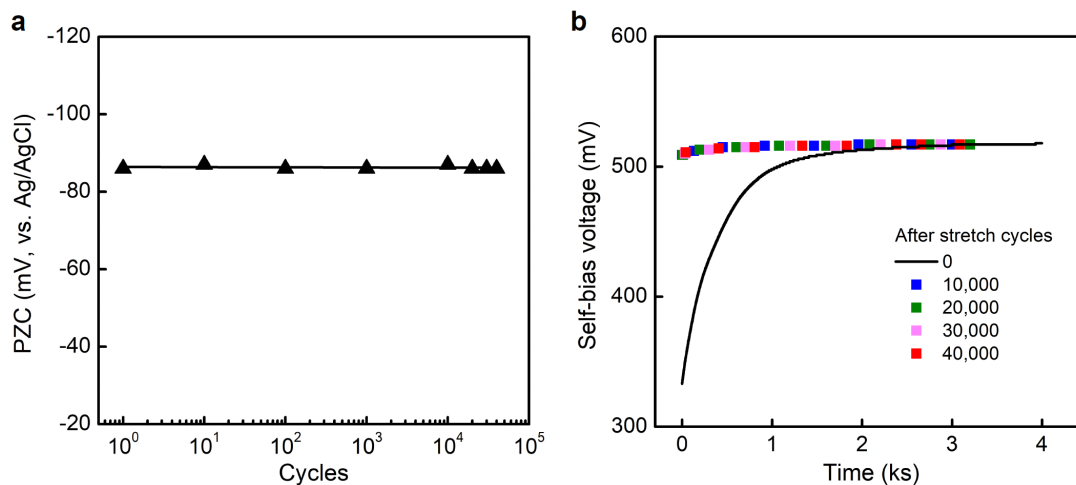
Supplementary Figure 24. The energy harvested during stretch and during stretch release for a 40% sinusoidal deformation of an OPS twistrion in 0.1 M HCl electrolyte. a, The log-scale frequency dependence of the total energy harvested per cycle, the harvested energy during stretch, and the harvested energy during stretch release. **b,** The frequency dependencies of the ratio of the output energy during stretch to the output energy during stretch release, the output energy during stretch, and the output energy during stretch release. Inset: The time dependence of the gravimetric power for an OPS harvester for a sinusoidal stretch at 0.1 Hz. The red areas and blue areas under the power curves are the energy output during stretch and stretch release, respectively.



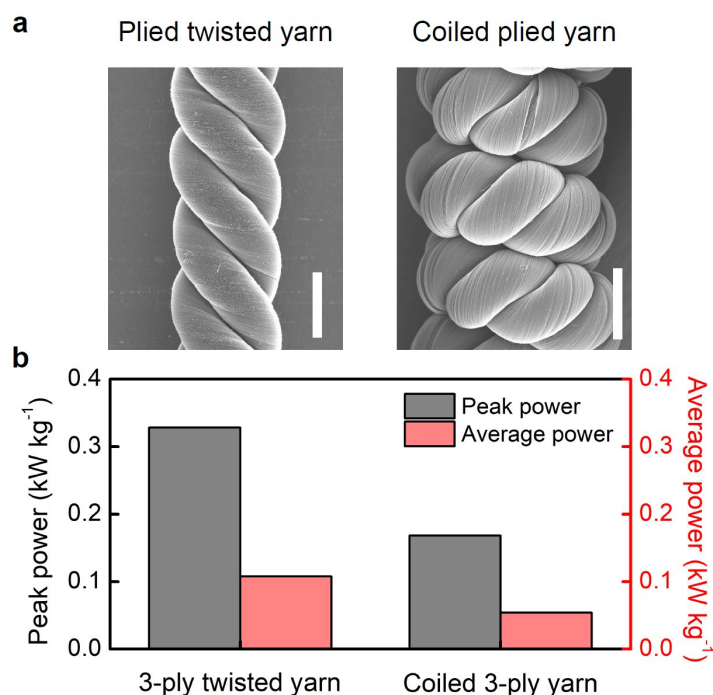
Supplementary Figure 25. The long-term stability of OPS harvester performance during cycling in HCl and LiCl aqueous electrolytes. a, The stability during cycling of the generated OCV of an OPS harvester in 0.1 M HCl electrolyte during over 40,000 sinusoidal stretch cycles to 25% strain at 1 Hz. Inset: The generated OCV of the OPS harvester during the final 10 stretch cycles. **b,** The peak power, average power, and electrical energy per cycle for the OPS harvester in 0.1 M LiCl during 40,000 sinusoidal 1 Hz cycles to 25% strain. Inset: The time dependence of output power during stretch cycling for a 94 Ω load resistance.



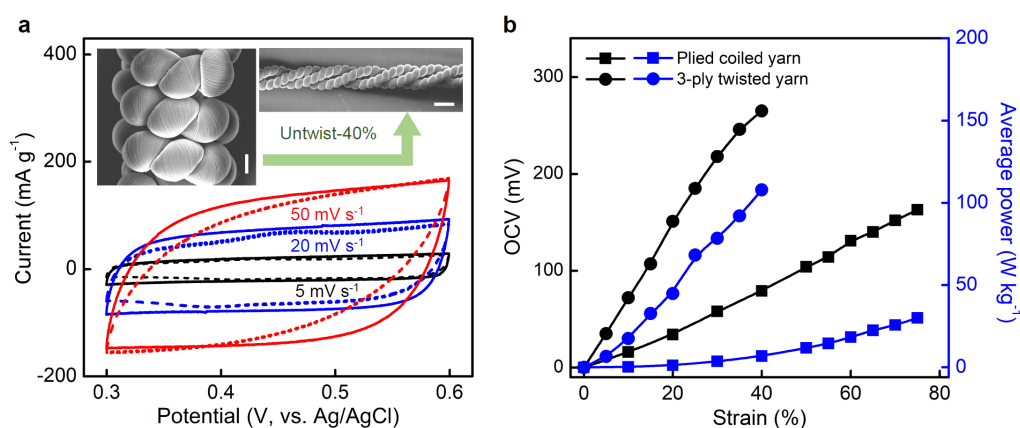
Supplementary Figure 26. The stability of tensile stress and structure of OPS harvesters during cycling in an aqueous HCl electrolyte. **a**, Mechanical stability is indicated by the reproducibility of the peak tensile stress of a 3-ply yarn harvester during 40,000 sinusoidal stretch-release cycles to 25% strain at 1 Hz in 0.1 M HCl aqueous electrolyte. Inset: The stretch cycle dependence of tensile stress for the 3-ply yarn harvester during initial and final stretch cycles. **b**, SEM image of a 3-ply yarn harvester after applying 5 turns of unplying after the above 40,000 cycles. Panels (c) and (d) are high magnification images of the areas shown in (b). Area 1 and area 2 are the outer and inner surfaces of the yarn for regions without and with inter-ply contact, respectively.



Supplementary Figure 27. The stability of PZC and self-bias voltage during cycling of OPS harvesters in an aqueous HCl electrolyte. **a**, The potential of zero charge (PZC) of the 3-ply yarn harvester after the investigated sinusoidal stretch-release cycles, measured using piezoelectrochemical spectroscopy for a sinusoidal 3 Hz stretch to 10%. **b**, The self-bias voltage of the 3-ply yarn harvester after the end of 0, 10,000, 20,000, 30,000, and 40,000 sinusoidal stretch-release cycles in which the 3-ply yarn harvester was stretched to 20% strain at 3 Hz in 0.1 M HCl electrolyte. The result for the non-cycled yarn shows the charging time from initial insertion into the electrolyte.

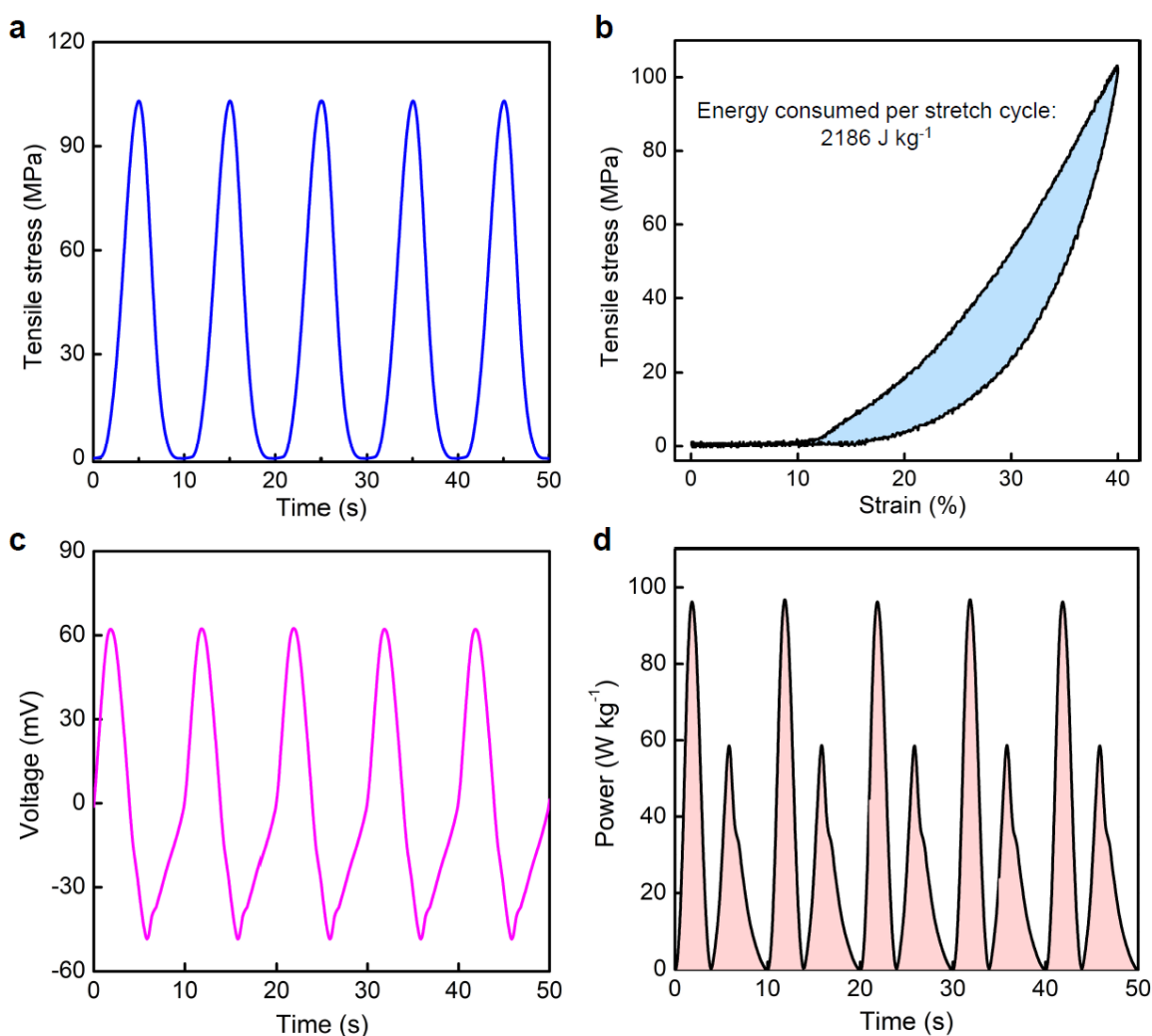


Supplementary Figure 28. Comparison of the structure and output power of a 3-ply twisted yarn harvester and a coiled 3-ply yarn harvester. a, SEM images of a 3-ply twisted yarn harvester (left) and a coiled 3-ply yarn harvester (right) (scale bar: 100 μm). **b,** The peak power and average power for the 3-ply twisted yarn harvester and the coiled 3-ply yarn harvester. The output power was obtained by stretching the harvesters to maximum reversible strain at 1 Hz in 0.1 M HCl electrolyte.

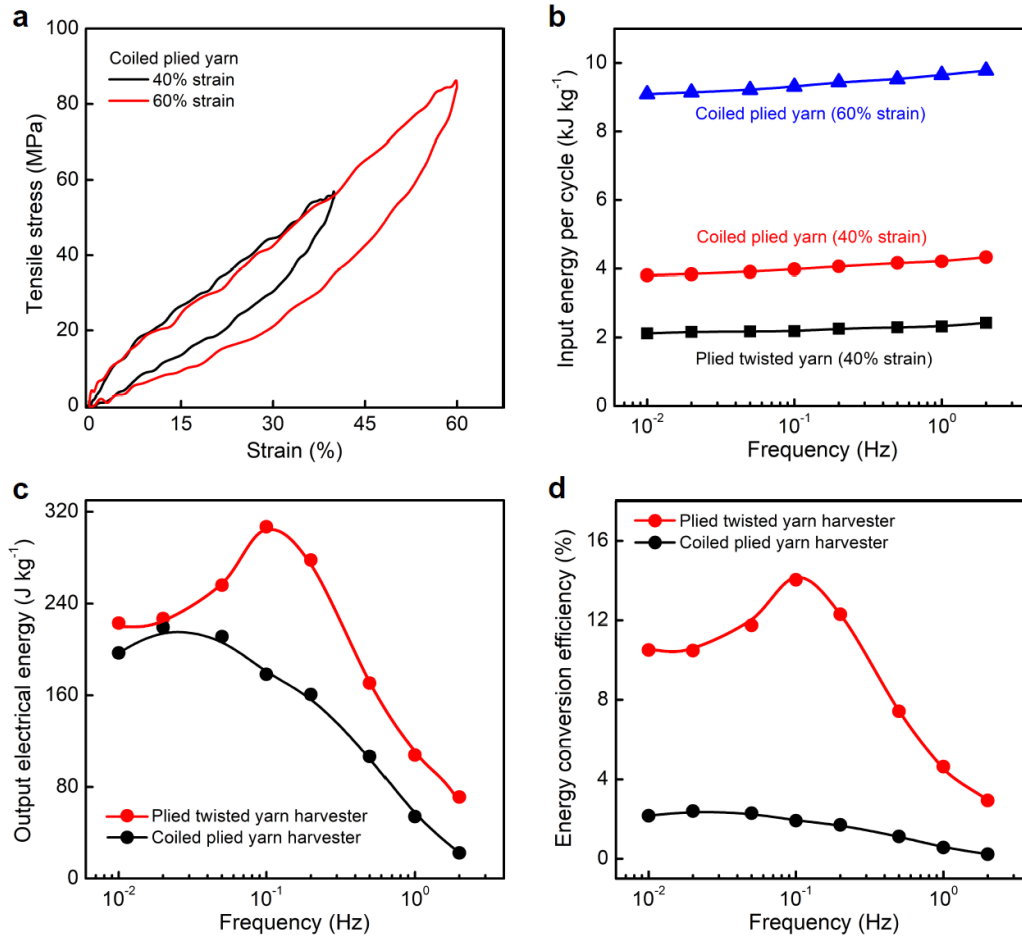


Supplementary Figure 29. Comparison of harvester performance for a plied twisted yarn and a plied coiled yarn, wherein the same diameter precursor twisted yarns were used, so the outer diameter of the plied coiled yarn (330 μm) was much larger than for the plied twisted yarn (171 μm). a, Cyclic voltammetry curves at 5 mV s^{-1} , 20 mV s^{-1} , and 50 mV s^{-1} scan rate for 0% strain of a 3-ply coiled yarn harvester (dash line) and a 3-ply twisted yarn harvester (solid line) in 0.1 M aqueous HCl electrolyte. Inset: SEM images of a plied coiled yarn (left, scale bar: 50 μm) and this yarn after removing 40% of the plying twist (right, scale bar: 200 μm), so that the plies become easier to see. **b,** The OCV and average power versus

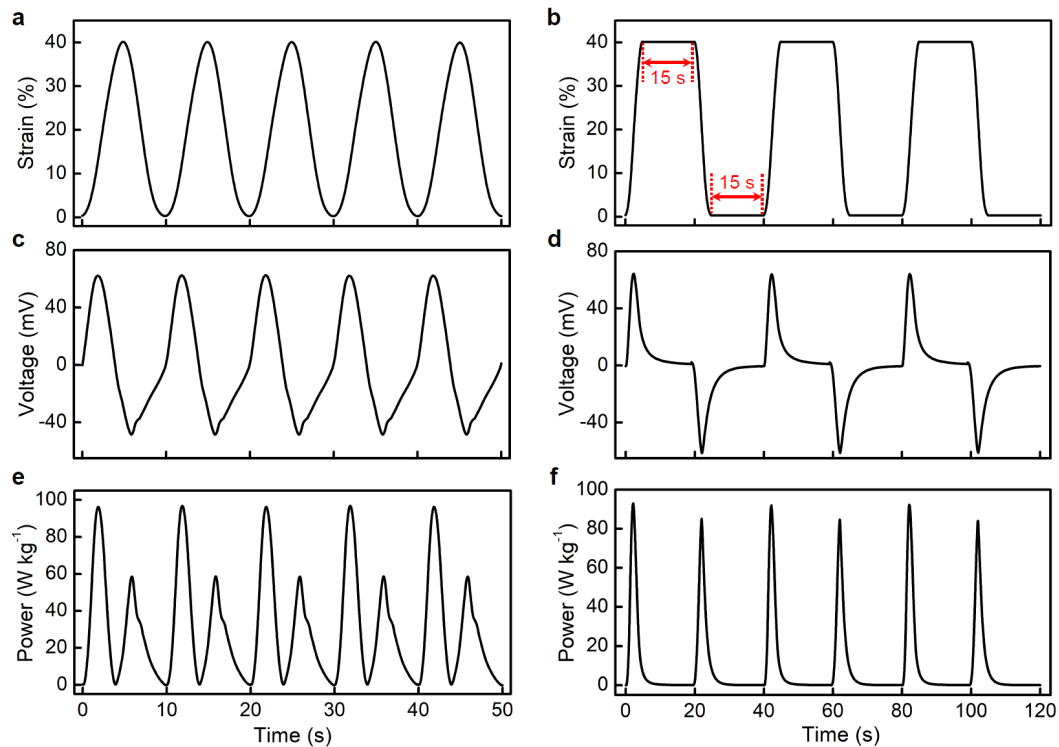
tensile strain for the 3-ply coiled yarn harvester and the 3-ply twisted yarn harvester in 0.1 M aqueous HCl electrolyte.



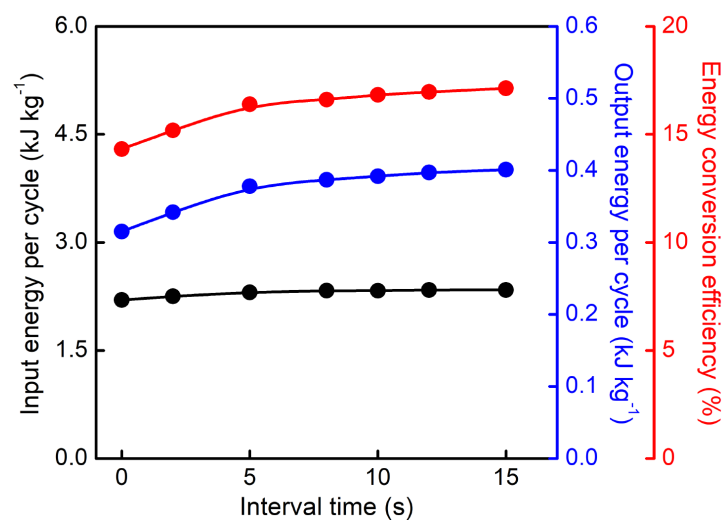
Supplementary Figure 30. The applied tensile stress and stress-strain curves during sinusoidal-wave harvesting, the thereby generated voltage across an external load resistance that optimizes average power, and the output power for an OPS harvester in 0.1 M HCl electrolyte during this 0.1 Hz sinusoidal deformation. a, The time dependence of tensile stress for 40% sinusoidal strain of an OPS harvester. **b,** The stress-strain curves for the above deformation of the OPS harvester. The mechanical energy inputted (the blue area) in one stretch cycle is 2186 J kg⁻¹. **c,** The time dependence of the generated voltage across an external load resistance of 196 Ω when the OPS harvester was sinusoidally stretched to 40% strain at 0.1 Hz. **d,** The output electrical power versus time for the deformation and load resistance used for (c). The red areas under the power curves are the energy output during the deformation cycles. The output energy per stretch cycle is 307 J kg⁻¹, and resulting energy conversion efficiency for the OPS harvester is 14.0%.



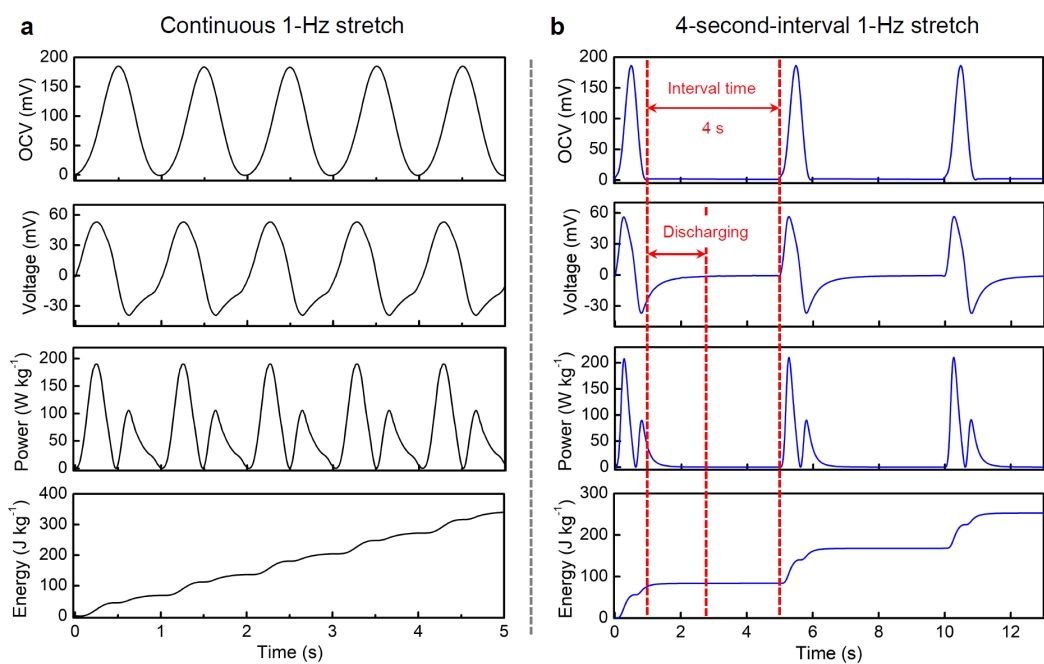
Supplementary Figure 31. The input mechanical energy, output electrical energy, and energy conversion efficiency of a 3-ply yarn harvester and a coiled 3-ply yarn harvester for a wide frequency range. a, Stress-strain curves for 40% strain and 60% strain of a coiled 3-ply yarn harvester in 0.1 M HCl electrolyte during a 1-Hz-sinusoidal-stretch cycle. **b,** The input mechanical energy per cycle versus stretch frequency for a coiled 3-ply yarn harvester (40% strain and 60% strain) and a 3-ply twisted yarn harvester (40% strain) in 0.1 M HCl electrolyte. **c,** The output electrical energy versus stretch frequency for the maximum reversible strain of a coiled 3-ply yarn harvester and a 3-ply twisted yarn harvester in 0.1 M HCl electrolyte. **d,** The energy conversion efficiency versus frequency for the maximum reversible strain of a coiled 3-ply yarn harvester and a 3-ply twisted yarn harvester.



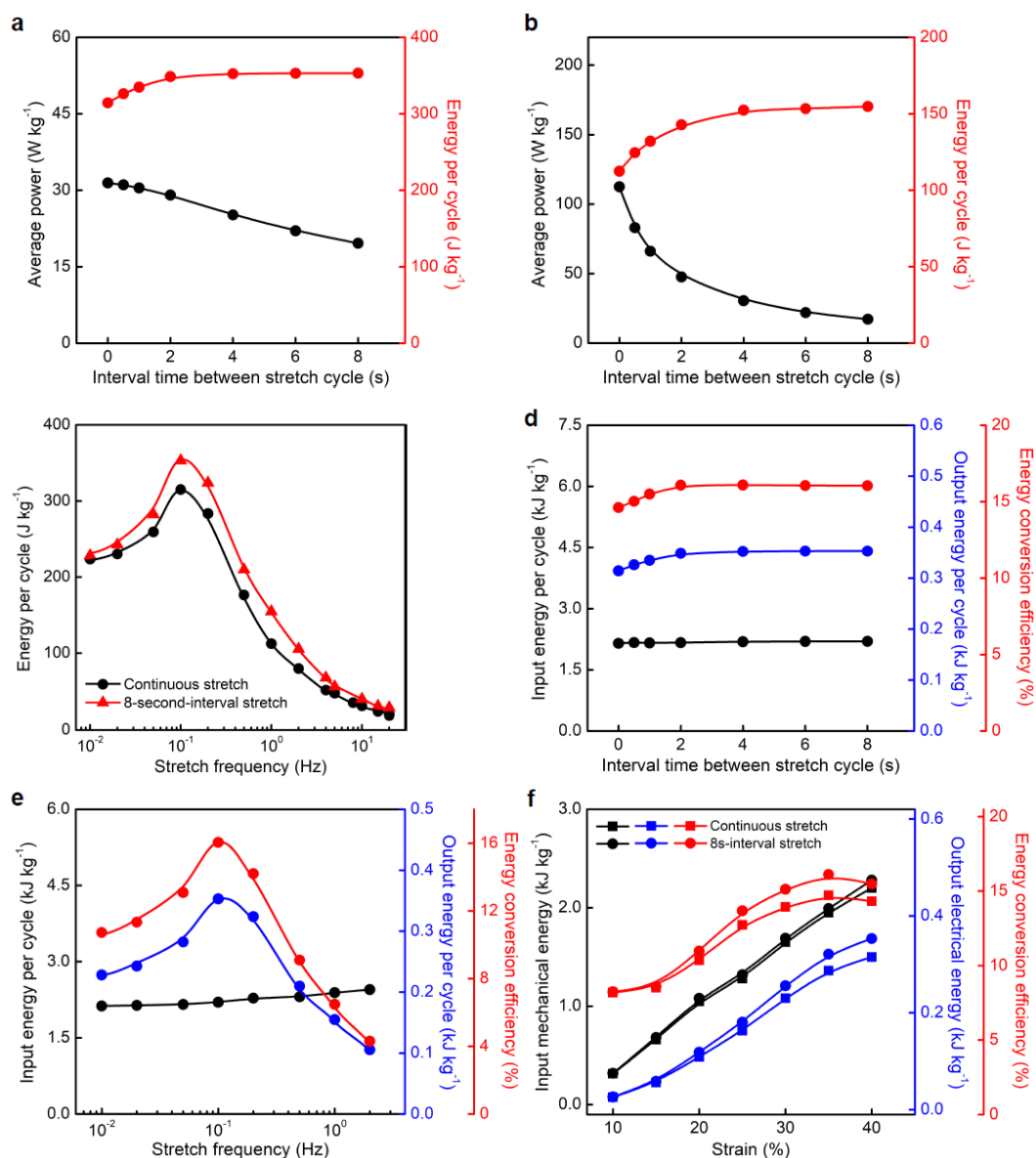
Supplementary Figure 32. Comparison of the harvesting performance of an OPS harvester under continuous and interrupted (IDH_{0m}) deformations. The time dependence of (a) tensile strain, (c) the generated voltage across an external load resistance, and (e) the output power for a Pt-wire-wrapped OPS harvester during continuous 0.1-Hz sinusoidal deformation and (b, d, f) during 15s-interrupted 0.1-Hz sinusoidal deformation (15s-IDH_{0m}). The load resistances used for maximizing average power were 196 Ω for continuous deformation and 180 Ω for interrupted deformation.



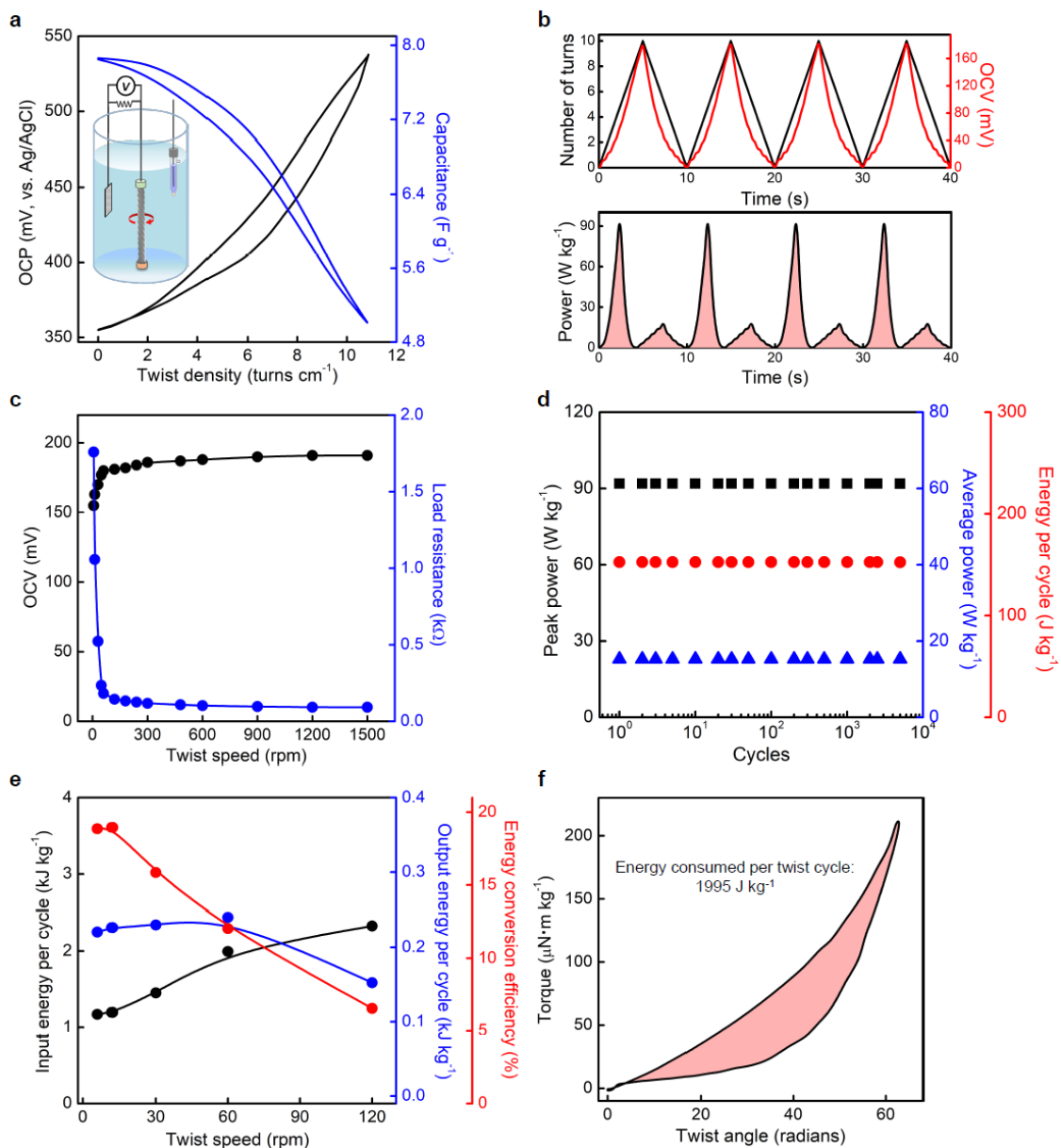
Supplementary Figure 33. Optimizing the time interval where energy is harvested but the twistrion is not deformed in order to maximize the energy conversion efficiency. For IDH_{0m} type interrupted deformation harvesting, the interval time dependencies of input mechanical energy per cycle, output electrical energy per cycle, and energy conversion efficiency for a 0.1 Hz, 40% strain of a Pt-wire-wrapped OPS harvester.



Supplementary Figure 34. Comparison of the harvesting performance of an OPS harvester under continuous and interrupted (IDH₀) deformations. The time dependence of the OCV, the voltage across an external load resistor, the output power, and the output energy for an OPS harvester during (a) a continuous 25%, 1 Hz sinusoidal stretch and (b) a 25%, 1 Hz, sinusoidal stretch that is interrupted by IDH₀ 4s intervals, where deformation is prohibited and harvesting is allowed. A 0.1 M aqueous HCl electrolyte was used.

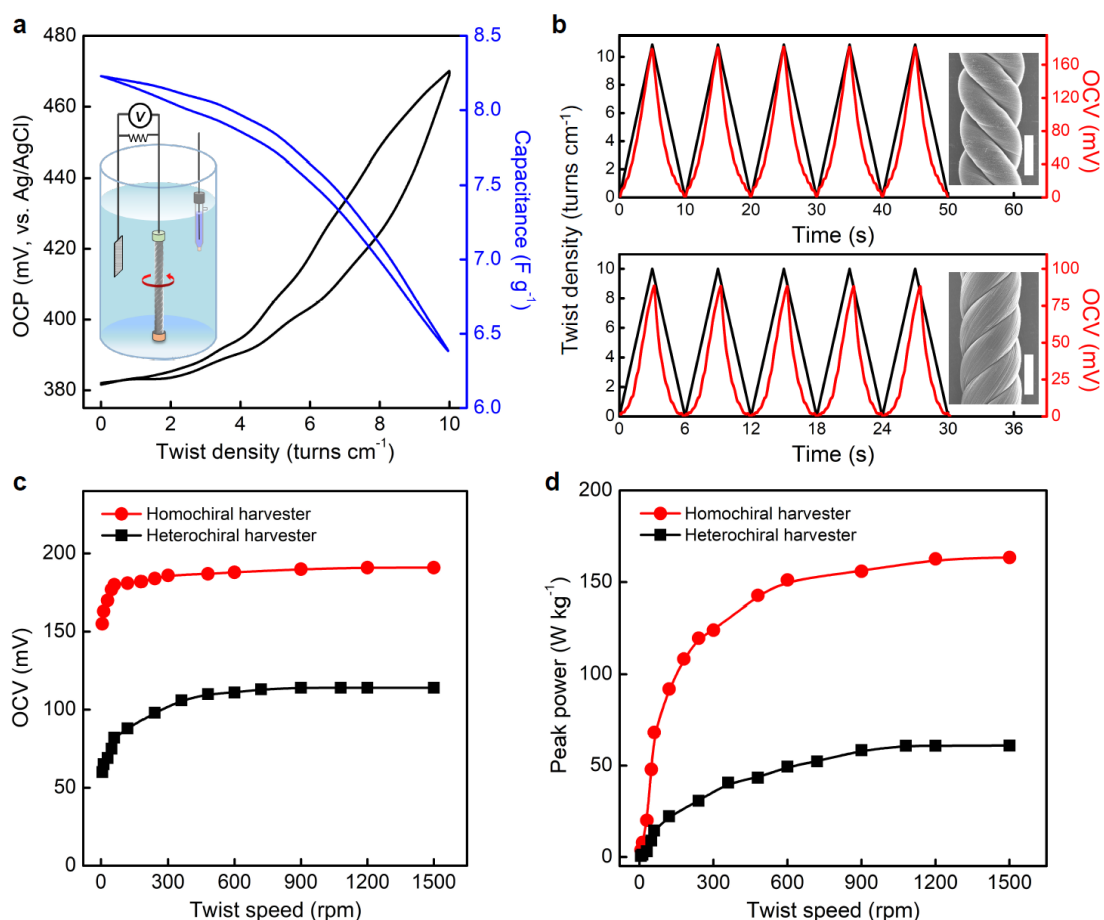


Supplementary Figure 35. The effect of inter-cycle harvesting time for IDH_0 on the average power and energy per cycle for 40% strain of a Pt-wire-wrapped OPS harvester in 0.1 M aqueous HCl. The dependence of average power on the inter-cycle harvesting time for (a) a 0.1 Hz sinusoidal deformation and (b) a 1 Hz sinusoidal deformation. c, Comparison of the stretch frequency dependence of energy per cycle for continuous sinusoidal deformation and an 8s-interrupted sinusoidal deformation (8s- IDH_0). The dependencies of input mechanical energy per cycle, output electrical energy per cycle, and energy conversion efficiency on (d) the deformation interruption time between 0.1 Hz sinusoidal deformation cycles, (e) the deformation frequency, and (f) the tensile strain for an 8s deformation interruption time.

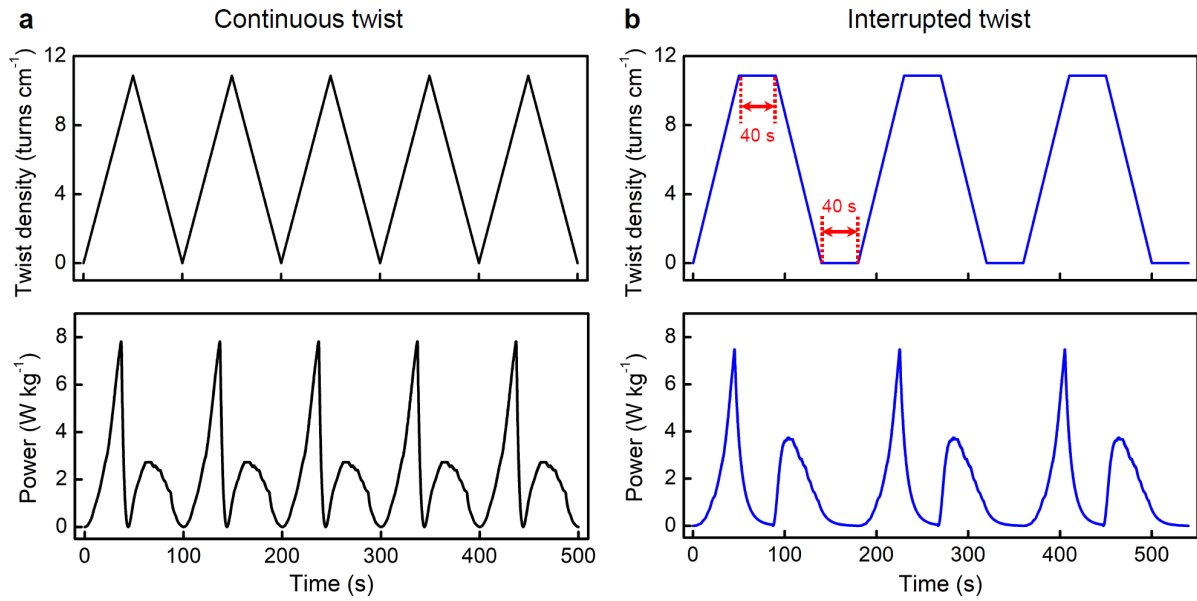


Supplementary Figure 36. Torsional mechanical energy harvesting by isometrically twisting and untwisting a 3-ply, 9.2-mm-long OPS harvester in 0.1 M aqueous HCl electrolyte. **a**, The OCP and capacitance for an OPS harvester as a function of the inserted twist density during harvesting using isometric twist and untwist at 60 rpm. Inset: Illustration of an OPS harvester during isometric (constant length) twist and untwist. **b**, The time dependence of the number of turns and resulting OCV (top) and the output power (bottom) for the OPS harvester during isometric twist and untwist at 120 rpm. The red areas under the power curves are the generated electrical energy. **c**, The OCV and corresponding output-energy-maximizing load resistance versus twist speed for the OPS harvester that is undergoing 10.8 turns cm^{-1} of isometric twist insertion and removal. **d**, The peak power, average power, and output energy per cycle for 10.8 turns cm^{-1} change in twist density as a function of cycles, showing that performance was maintained for the investigated 5,000 twist cycles at 120 rpm. **e**, The twist speed dependencies of per-cycle input mechanical energy, output energy per cycle, and energy conversion efficiency for a 3-ply yarn harvester. **f**, The dependence

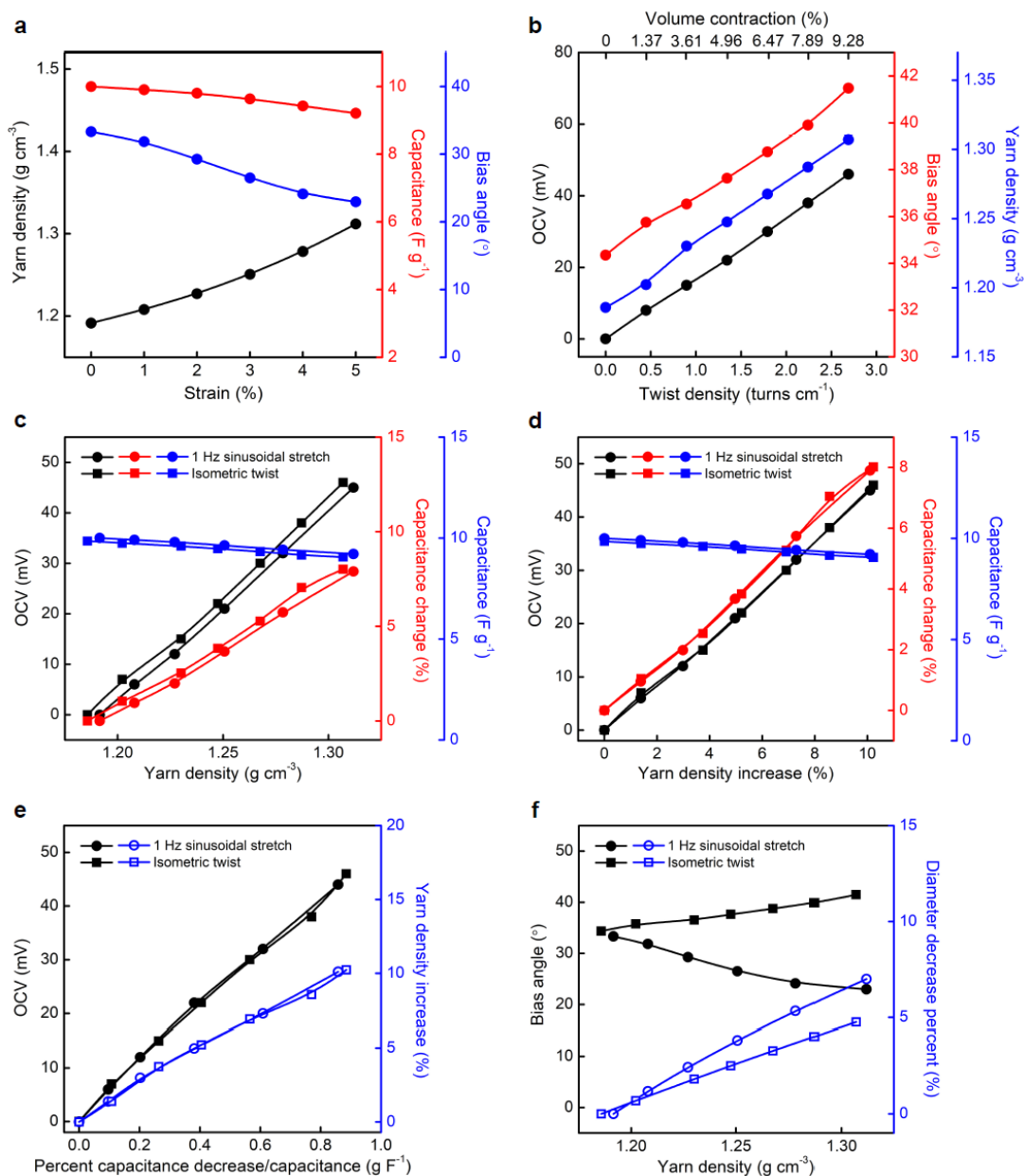
of torque on twist angle for the OPS harvester during twist insertion at 60 rpm. The consumed mechanical energy (indicated by the red area) during one twist cycle is 1995 J kg^{-1} .



Supplementary Figure 37. Torsional energy harvesting by isometrically up-twisting the plying twist for a homochiral and heterochiral 3-ply yarn harvesters in 0.1 M HCl electrolyte. **a**, The OCP and capacitance for a heterochiral 3-ply yarn harvester during isometric twist and untwist at $1.67 \text{ turns cm}^{-1} \text{ s}^{-1}$. **b**, The time dependencies of twist density and OCV for a 9.2-mm-long homochiral harvester (top) and a 6.0-mm-long heterochiral harvester (bottom) during torsional harvesting using a twist speed of 120 rpm. Since these harvesters are kept at constant length when up-twisted during torsional harvesting, they do not coil. Inset: SEM images of a homochiral 3-ply yarn harvester and a heterochiral 3-ply yarn harvester (scale bar: $100 \mu\text{m}$). The twist-speed dependence of (c) OCV and (d) peak power for the homochiral harvester and the heterochiral harvester during 10.8 and 10.0 turns cm^{-1} isometric twist.

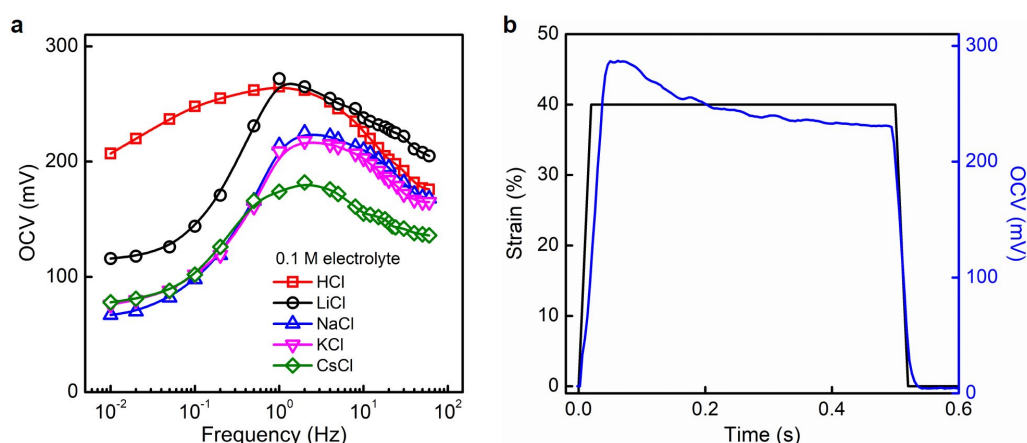


Supplementary Figure 38. Application of interrupted deformation harvesting ($\text{IDH}_{0\text{m}}$) for increasing the conversion of torsional mechanical energy to electricity during isometric twist and untwist. The time dependencies of twist density and output power for an OPS harvester during (a) continuous twist and untwist cycles and (b) for cycles having interrupted torsional deformation, where harvesting is conducted for 40 s after the maximum and minimum twist levels are reached. During harvesting, the OPS twistron was first up-twisted in the plying twist direction and then down-twisted by the same amount in the opposite direction. The harvester was 9.2-mm-long and the twist speed was 12 rpm.



Supplementary Figure 39. The dependencies of peak OCV, Poisson's ratio, bias angle, and yarn density on 1 Hz sinusoidal reversible tensile strain and on additionally-inserted twist density (at $161^{\circ} \text{ cm}^{-1} \text{ s}^{-1}$) for 28 turns cm^{-1} twisted yarns in 0.1 M aqueous HCl electrolyte. **a**, The dependencies of yarn density, capacitance, and bias angle on applied tensile strain for the twisted yarn. **b**, The dependencies of OCV, bias angle, and yarn density on isometrically inserted twist density for a 22.3-mm-long, 102- μm -diameter twisted yarn, having an initial twist of 28 turns cm^{-1} . The direction of isometric twist insertion (at 60 rpm) was the same as that for yarn twist and the added twist density is normalized to the initial length of the twisted yarn. The top x-axis shows the observed percent volume contraction for each of the twist densities shown on the bottom x-axis. The dependencies of OCV, capacitance change, and capacitance for the twisted yarn on (c) yarn density and on (d) the percent yarn density increase, when the yarn was either axially stretched or isometrically twisted. **e**, The dependencies of OCV and percent yarn density increase for the twisted yarns on the ratio of percent capacitance decrease to the capacitance for a given deformation. **f**, The dependencies

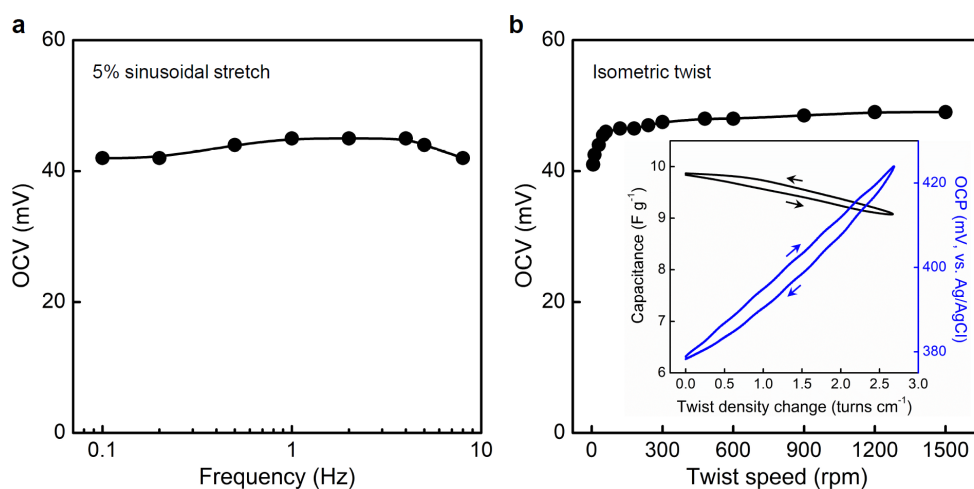
of bias angle and percent diameter decrease for the twisted yarns on yarn density. For investigating the effect of densification caused by the yarn's Poisson's ratio on harvesting, a non-coiled yarn with 28 turns cm^{-1} of twist was stretched to the maximum reversible strain. The average Poisson's ratio, for going between zero strain and the applied strain, increased from 1.18 for 1% strain to 1.40 for 5% strain. These tensile strains produced stretch-induced densification (of 1.4% and 9.2%, respectively) (Fig. 3a), rather than decreasing density like for most materials. As a result of this Poisson ratio effect, the yarn density increased from 1.19 g cm^{-3} at 0% strain to 1.31 g cm^{-3} at 5% strain, which produced a capacitance change of 8.0% and an OCV of 45 mV (Supplementary Fig. 39a). This tensile strain also decreased the yarn's bias angle from 33.3° to 22.9°, corresponding to a yarn diameter decrease of 7.0% (Supplementary Fig. 39f). As shown by Supplementary Fig. 39c, this tensile stretch provides an OCV that approximately linearly depends on the change in yarn density. A nearly identical dependence of OCV on percent change in yarn density is obtained for isometric twist insertion and for yarn stretch (Supplementary Fig. 39d). This nearly identical behavior does not result from similar changes in bias angle with twist insertion and stretch, since the OCV increases with increasing bias angle for isometric twist insertion and the OCV increases with decreasing bias angle for tensile deformation. Furthermore, this increasing bias angle during twist insertion increases yarn density, while this decreasing bias angle during stretch is associated with stretch densification. More specifically, when the twist in a 28 turns cm^{-1} non-coiled yarn was isometrically increased by 2.7 turns cm^{-1} , the bias angle of the yarn increased from 34.4° to 41.5° and the yarn density increased from 1.18 to 1.31 g cm^{-3} , corresponding to a volume contraction of 9.3% and a yarn diameter decrease of 4.8% (Supplementary Fig. 39f). As a result of this yarn densification at a twist speed of 60 rpm, the OCV of the twisted yarn increased by 46 mV. On the other hand, elongating a similar yarn by 5% decreased the yarn's bias angle from 33.3° to 22.9° and increased the yarn density from 1.19 to 1.31 g cm^{-3} , corresponding to a volume contraction of 9.2%, which produced an OCV of 45 mV.



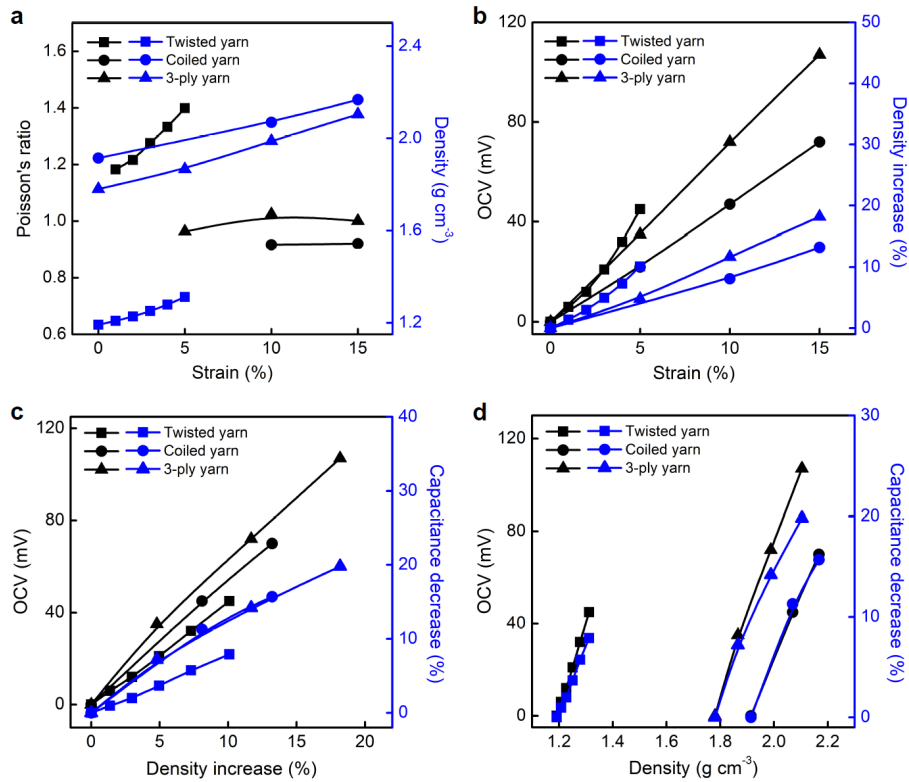
Supplementary Figure 40. The OCV as a function of frequency and time for a 3-ply yarn harvester. a,

The frequency dependence of OCV for the OPS harvesters when sinusoidally stretched to 40% tensile strain in 0.1 M aqueous electrolytes of HCl, LiCl, NaCl, KCl and CsCl. **b,** The time dependencies of tensile strain and OCV for the OPS harvester deformed by a square-wave stretch in 0.1 M HCl electrolyte. Since $OCV = Q/C_1 - Q/C_2 = (C_2 - C_1)Q/C_1C_2$, the initial increase of OCV at very low frequencies in Supplementary Fig. 40a

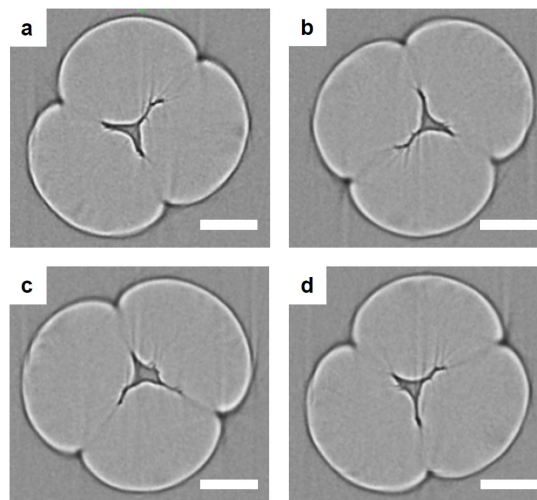
can be explained by an increased stretch-induced capacitance change at higher frequencies. This is because at higher frequencies, there is not sufficient time for charges to redistribute on the yarn to minimize the capacitance decrease caused by inter-bundle contact, so the stretch-induced capacitance change is larger. Consistent with this hypothesis, Supplementary Fig. 40b shows that the OCV for a square-wave stretch decreases with increasing post-stretch time. On the other hand, at very high frequencies, the capacitance decreases with increasing frequency and there is not sufficient time for electrolyte extrusion from the yarn. This latter dependence is basically due to the strain rate dependence of twistrion volume change, which can be rephrased as the effective frequency dependence of the Poisson's ratio of an electrolyte filled yarn in an electrolyte bath.



Supplementary Figure 41. The effect of stretch frequency and twist speed on the OCV for a twisted yarn that is in an aqueous HCl electrolyte. a, The frequency dependence of OCV for 5% sinusoidal reversible strain of a twisted CNT yarn. **b,** The twist speed dependence of OCV for an identically made 22.3-mm-long twisted yarn that is up twisted by 2.7 turns cm⁻¹. Inset: The capacitance and OCP for the twisted yarn during twist insertion and twist removal at 60 rpm. The electrolyte used was 0.1 M aqueous HCl.

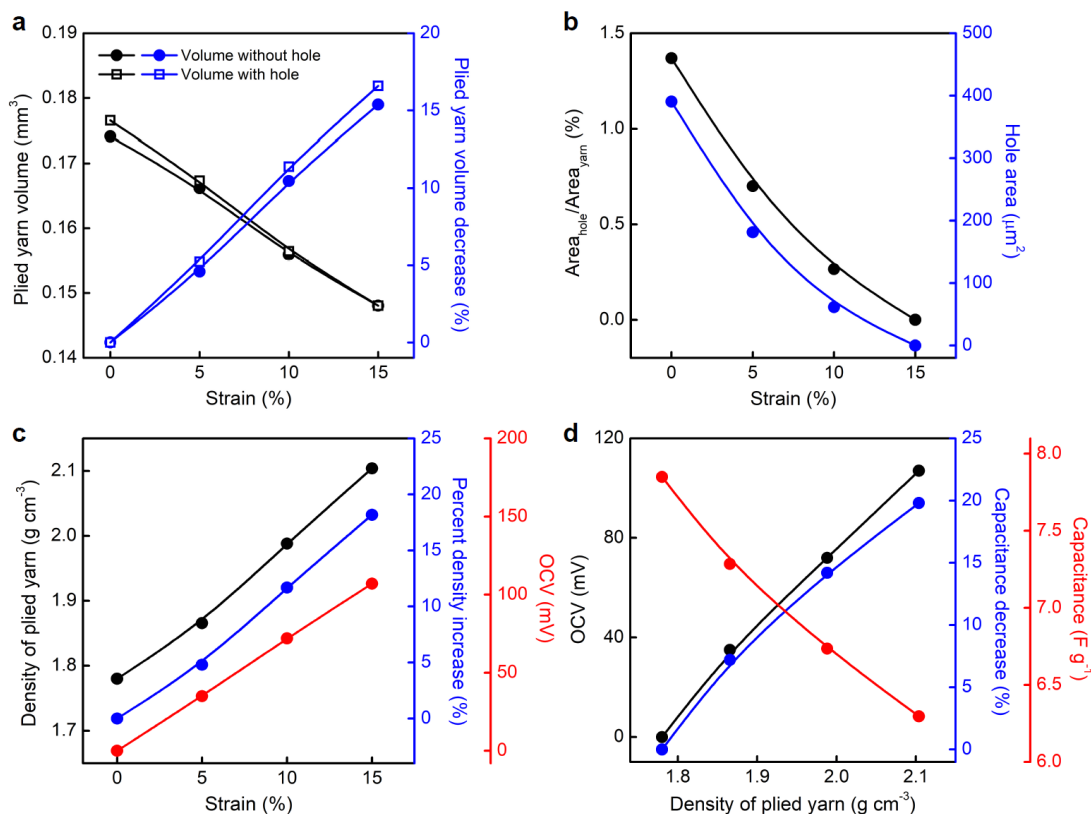


Supplementary Figure 42. The average Poisson's ratio, density, OCV, and capacitance of twisted, coiled, and 3-ply yarn harvesters when statically stretched. **a**, The dependence of average Poisson's ratio and density on tensile strain. The Poisson's ratios (ν) for 3-ply yarns and coiled yarns were calculated using the equation: $dV/V = (1-2\nu)dL/L$, where dV/V is the volume change for a given stretch of dL/L . The densities of 3-ply yarns and coiled yarns were calculated from the cross-sectional area of harvesters, obtained from X-ray tomography images. **b**, The dependence of OCV and percent density increase on tensile strain. **c**, The dependence of OCV and capacitance decrease (%) on percent density increase when harvesters were stretched. **d**, The dependence of OCV and capacitance decrease on density when harvesters were stretched.

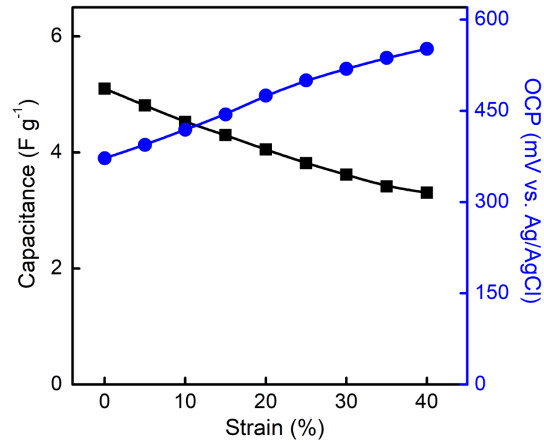


Supplementary Figure 43. Cross-sectional images along the length of a non-stretched 3-ply yarn harvester. (a, b, c, d) Typical X-ray tomography images (scale bar: $50 \mu\text{m}$) of yarn cross-section along the

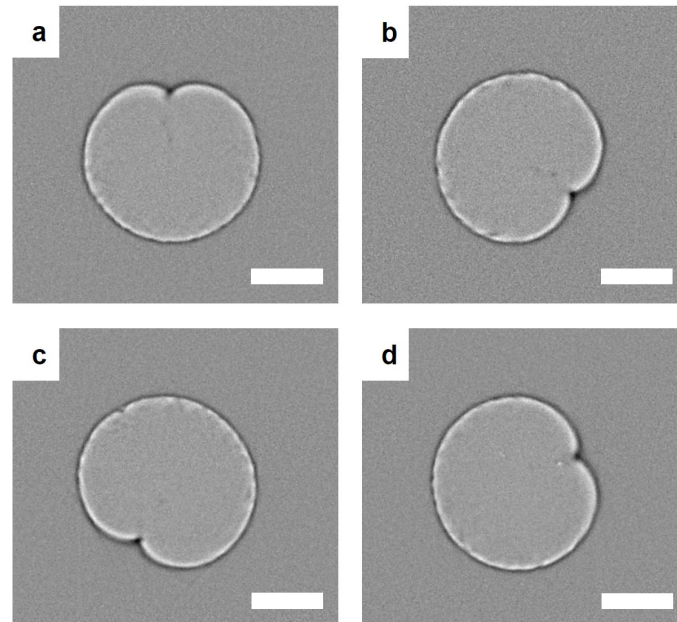
length of a torsionally-tethered, non-stretched 3-ply yarn harvester. The cross-sectional area of the 3-ply yarn harvester is about $2.85 \cdot 10^{-2} \text{ mm}^2$. The average density of the 3-ply non-stretched harvester is 1.76 g cm^{-3} when the inter-ply hole volume is included and 1.78 g cm^{-3} when this hole volume is excluded.



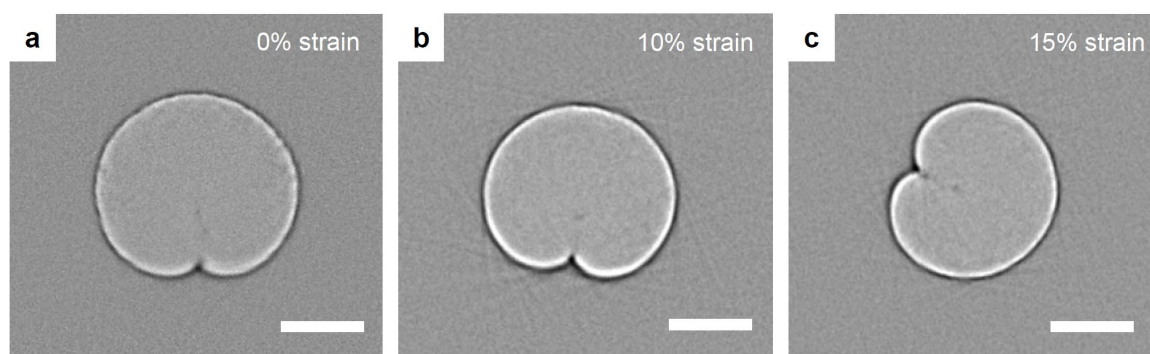
Supplementary Figure 44. The yarn volume, hole area, and yarn density of a 3-ply yarn harvester when stretched at different strains. a, The dependence of plied yarn volume and percent volume decrease on tensile strain for a 6.1-mm-long, 0.31-mg-weight 3-ply yarn harvester. **b,** The ratio of hole area to yarn area, and the hole area as a function of applied tensile strain for the plied harvester. **c,** The strain dependence in air of the static density and the static percent density increase, as well as the OCV (for a 1 Hz sinusoidal strain) for the plied yarn in 0.1 M HCl electrolyte. **d,** The dependence of OCV, capacitance decrease, and capacitance on the density of the plied yarn when stretched. The hole isn't considered in the calculation of plied yarn volume and density for (c, d).



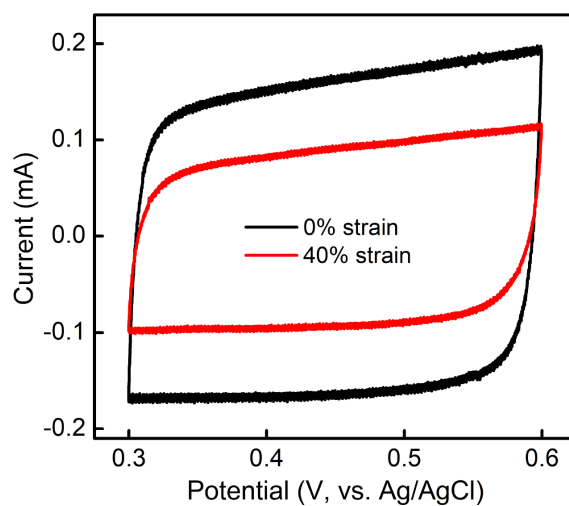
Supplementary Figure 45. The capacitance and OCP of a coiled yarn harvester in 0.1 M HCl electrolyte versus applied strain for 1 Hz sinusoidal stretch-release cycles to the indicated strains.



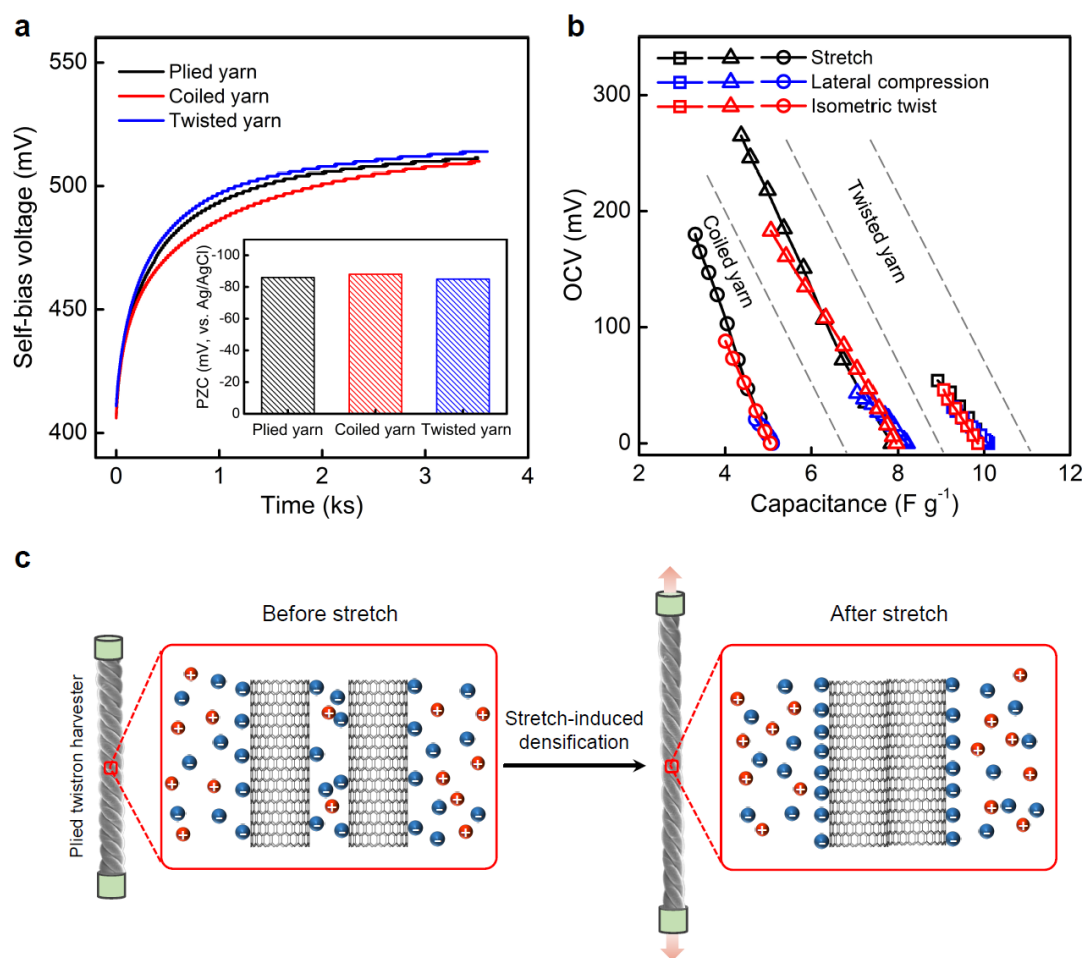
Supplementary Figure 46. Cross-sectional images along the length of a non-stretched coiled yarn. (a, b, c, d) Typical X-ray tomography images (scale bar: 50 μm) of yarn cross-section along the length of a torsionally-tethered, non-stretched coiled yarn harvester. The cross-sectional area of the coiled yarn harvester is about $1.13 \cdot 10^{-2} \text{ mm}^2$. The measured density of this 4.8-mm-long, 0.104-mg-weight coiled yarn is about 1.91 g cm^{-3} .



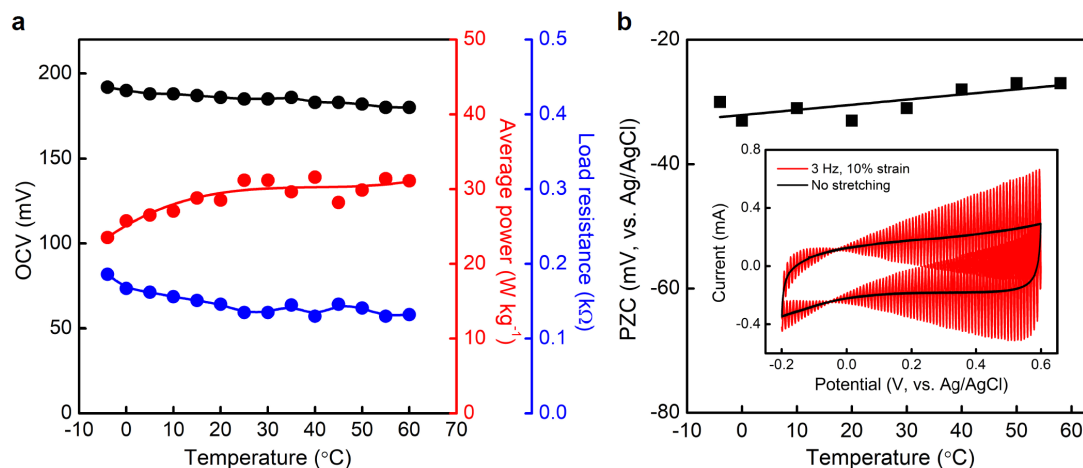
Supplementary Figure 47. Cross-sectional images of a coiled yarn when stretched to different strains. X-ray tomography images (scale bar: 50 μm) of the cross-sectional view of coiled yarn harvesters for 0% (a), 10% (b) and 15% (c) tensile stretch.



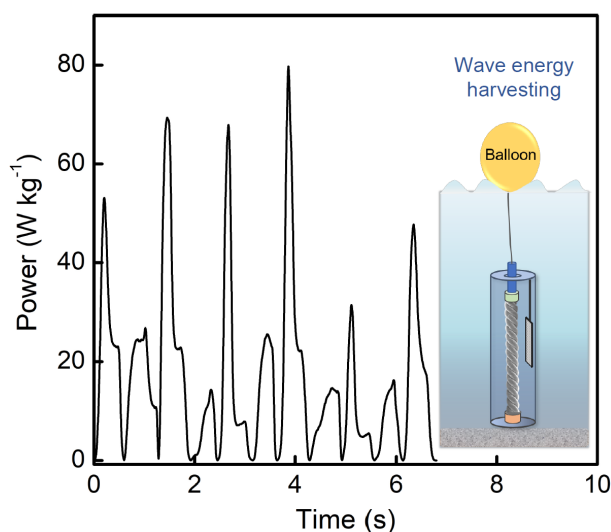
Supplementary Figure 48. Cyclic voltammety curves of an OPS harvester in 0.1 M aqueous HCl electrolyte for 0% strain and 40% strain when the potential scan rate is 50 mV s^{-1} .



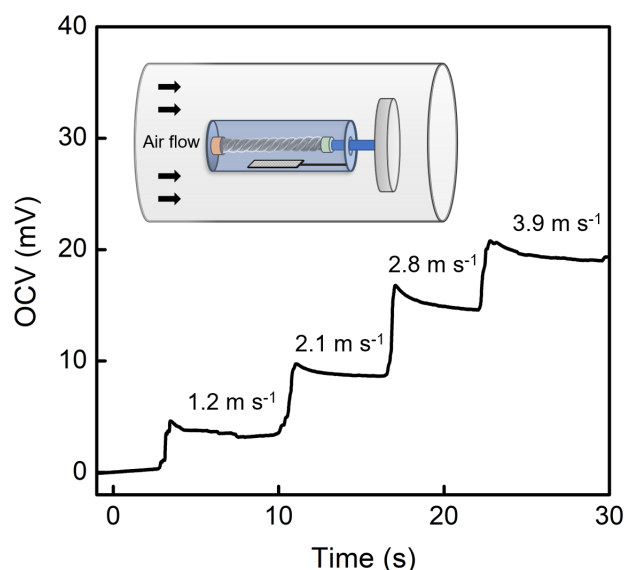
Supplementary Figure 49. The self-bias voltage at 0% tensile strain, the OCV as a function of capacitance for various deformations, and illustration of the electrochemical energy harvesting mechanism. a, The time dependence of self-bias voltage for plied, coiled, and non-coiled twisted yarns in 0.1 M HCl electrolyte. Inset: Result showing the negligible dependence of PZC on CNT twistrion geometry. **b,** The OCV for tensile, lateral compressive, and torsional deformation of plied, coiled, and non-coiled twisted yarns as a function of deformation-induced capacitance. **c,** Illustration of the energy harvesting mechanism for a plied twistrion harvester when stretched in the electrolyte. This shows the effect of yarn stretch on redistributing the charge from two nearby nanotubes to two nanotubes that are contacting. In this schematic illustration, we have kept the pictured net charge constant. Hence, if the net charge is constant, while the electrochemically accessible surface area is decreased (corresponding to a capacitance decrease), then the magnitude of the open-circuit electrode potential increases. This change is $-(Q/C_0) (\Delta C/(C_0-\Delta C))$, where Q is the injected charge from the electrolyte, C_0 and C_ϵ are the capacitances at zero and ϵ deformations, respectively, and where $\Delta C = C_0 - C_\epsilon$.



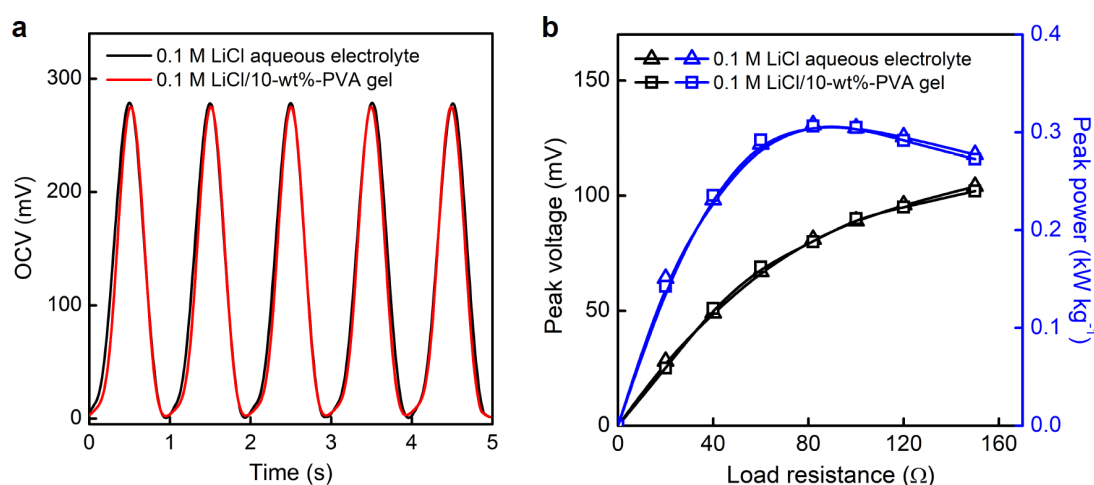
Supplementary Figure 50. The dependence of harvesting performance of an OPS harvester on temperature. **a**, The temperature dependencies of OCV, average power, and average-power-maximizing load resistance for a 40%, 1 Hz sinusoidal deformation of an OPS harvester in 0.6 M aqueous NaCl electrolyte. These results indicate that our OPS harvesters can operate over wide temperature ranges in oceans. **b**, The negligible dependence of PZC on temperature. Insert: Cyclic voltammograms (scan rate: 30 mV s⁻¹) for an OPS harvester in the above electrolyte (~25°C) either with or without a 3-Hz, 10% sinusoidal stretch. These results indicate that the PZC of the OPS harvester in 0.6 M NaCl electrolyte is -32 mV (relative to Ag/AgCl).



Supplementary Figure 51. The use of a ~10-cm-diameter balloon floating on the surface of salt water to harvest mechanical energy from the balloon's motion. The wave motion was artificially generated by periodically immersing at 0.8 Hz a foam plunger into the 0.6 M NaCl salt water bath. The pictured time dependence of output power is for a 0.15-mg-weight 3-ply yarn harvester.

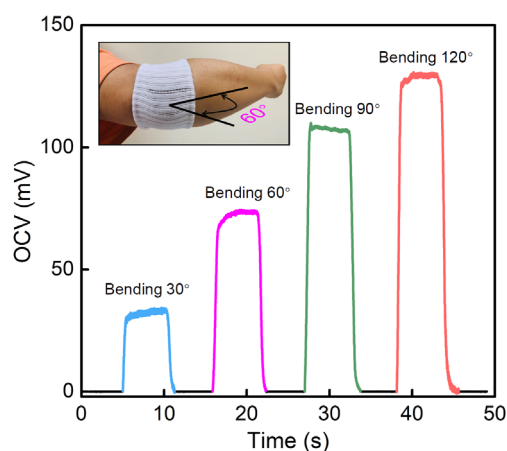


Supplementary Figure 52. The use of a 3-ply yarn harvester as a self-powered flow sensor for monitoring the velocity of air flow. Inset: a 31.6-mm-long 3-ply yarn harvester working electrode was connected to a piston rod, and mechanically limited to <20% strain. The flowing air contacts a 3.5-cm-diameter circular disk, whose movement stretches the twistron that is contained in a 1.5-cm-diameter electrolyte container. The electrolyte was a 0.6 M NaCl/10-wt%-PVA gel. The time dependence of generated OCV is plotted for different velocities of air flow.

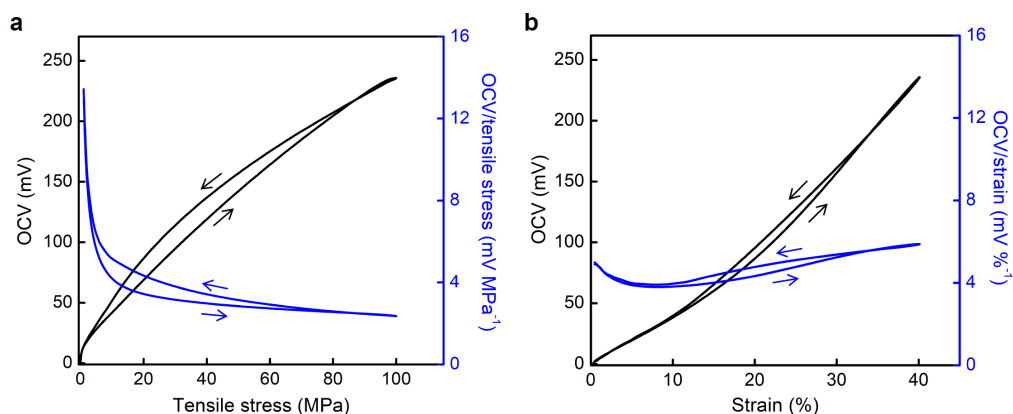


Supplementary Figure 53. The nearly identical OCV, peak voltage, and peak power for an OPS harvester stretched at 1 Hz in 0.1 M LiCl aqueous and gel electrolytes. **a**, The OCV for 40% strain of an OPS harvester stretched in 0.1 M aqueous LiCl electrolyte and 0.1 M LiCl-10-wt%-PVA gel electrolyte. **b**, The peak voltage and peak power as a function of the load resistance for an OPS harvester that was sinusoidally stretched to 40% strain. To eliminate the need for a liquid electrolyte bath, we fabricated an OPS harvester that used a polyvinyl alcohol (PVA) gel electrolyte (0.1 M LiCl/10 wt% PVA). A single twisted, non-coiled yarn (10 turns cm^{-1}) was used as the counter electrode and placed in parallel near the OPS harvester. The OPS harvester in 0.1 M LiCl/10-wt%-PVA solid gel provided an almost identical OCV and

output power as when operated in 0.1 M LiCl solution. This advance allows our harvesters to operate in air to convert various mechanical motions into electrical energy.

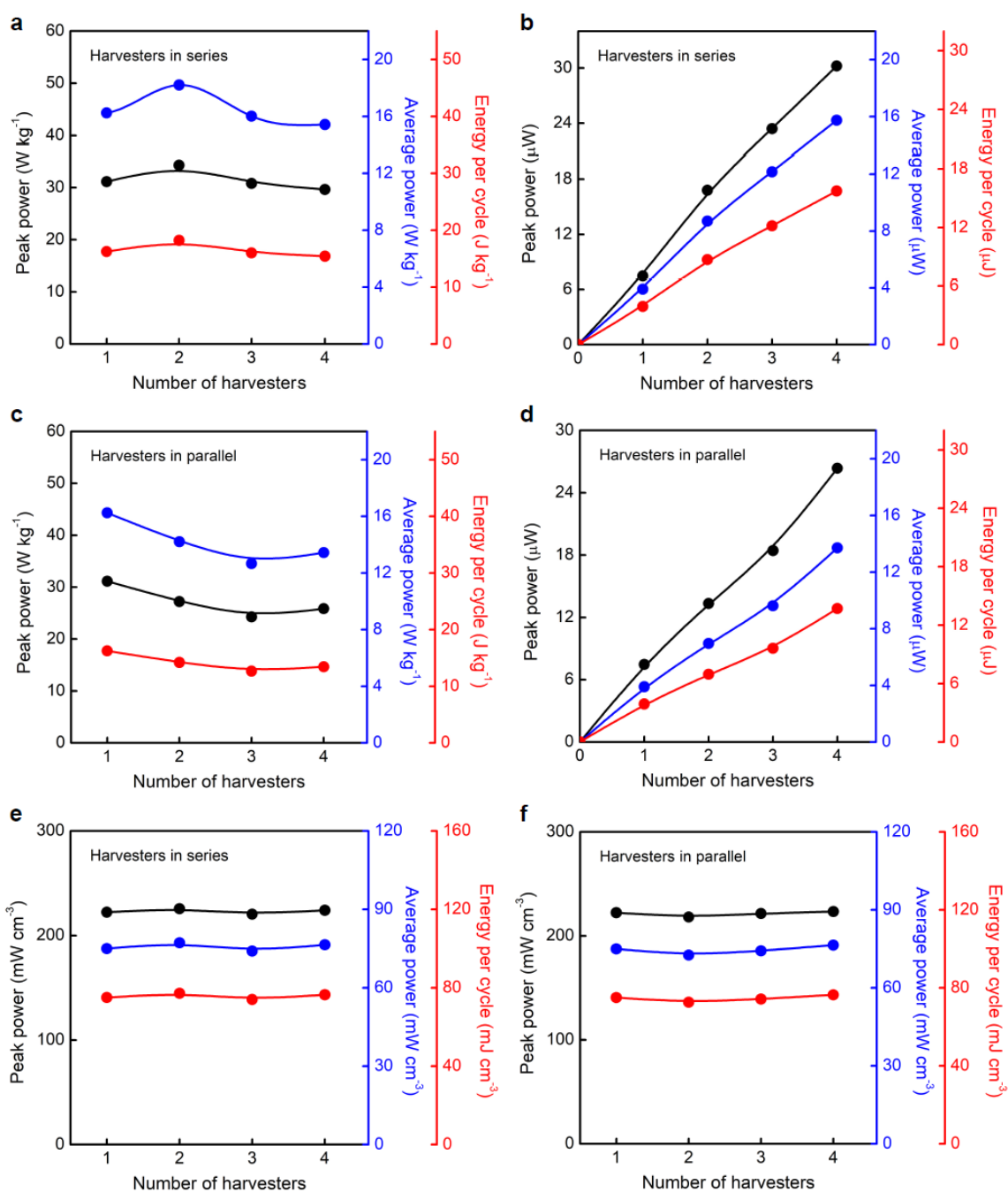


Supplementary Figure 54. The use of the OPS harvesters as wearable, self-powered strain sensors for monitoring human arm motion. A 35-mm-long 3-ply yarn harvester working electrode and a 40-mm-long counter electrode (10 turns cm^{-1}) were sewn into a cotton textile as an elbow support for arm bending. Both electrodes were overcoated with a solid electrolyte of 0.1 M LiCl/10-wt%-PVA gel, which connects the two electrodes. The time dependence of the generated OCV for different angles of arm bending. The insets show a photograph taken during arm bending by 60°. Figure 4d and Supplementary Fig. 54 show the application of the all-solid-state OPS harvester of Supplementary Fig. 53 as a harvester and a sensor of arm motion. Both the harvesting OPS electrode and a single twisted yarn (10 turns cm^{-1}) counter electrode were first hand sewn in-parallel along the arm direction of a cotton elbow brace, and then jointly overcoated with a solid electrolyte (0.1 M LiCl/10-wt%-PVA gel). While the harvesting electrode was sewn into the textile in a largely straight configuration, with firmly tethered ends, the non-harvesting counter electrode was sewn in a zigzag pattern with non-tethered ends, so that it was little deformed during arm bending. When the arm bent to 30°, the OPS harvester generated an OCV of ~30 mV. Upon further bending, the OCV monotonically increased to provide an OCV of 130 mV at an arm bending angle of 120°.



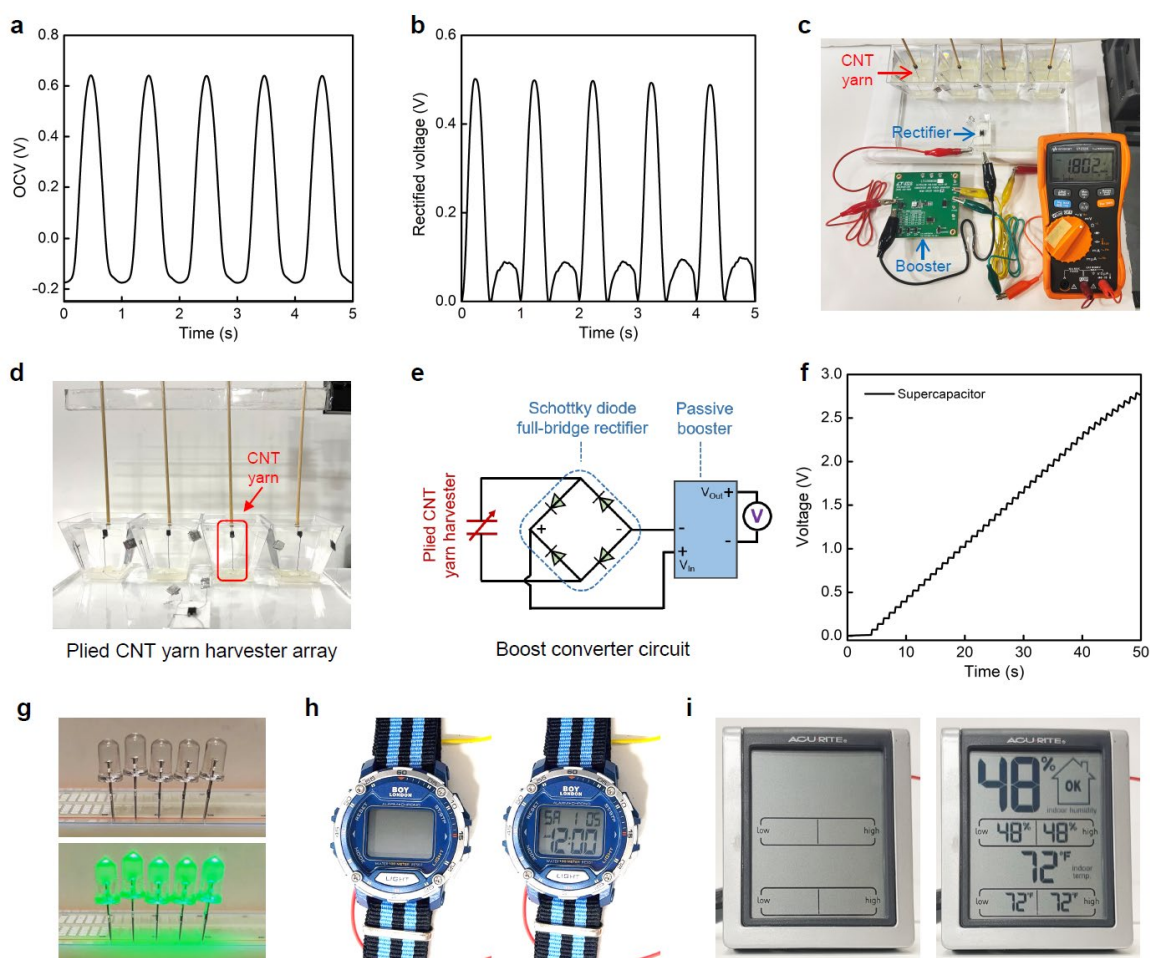
Supplementary Figure 55. The generated OCV of a 3-ply yarn harvester as a function of tensile stress and tensile strain. The dependencies of (a) the OCV and the ratio of OCV to tensile stress on tensile stress

and (b) the OCV and the ratio of OCV to tensile strain on tensile strain for a 0.05 Hz, 40% strain sinusoidal stretch-release cycle. The used electrolyte was 0.1 M aqueous HCl.



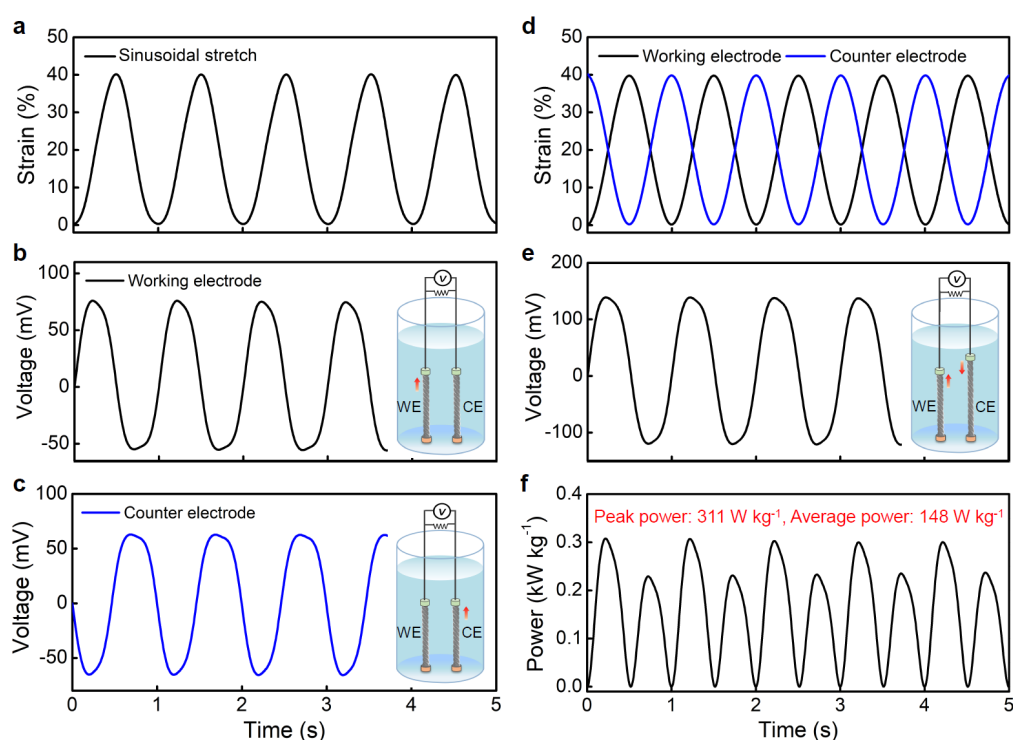
Supplementary Figure 56. The output power and energy per cycle for OPS harvesters connected in series and in parallel. The peak power, average power, and energy per cycle for a 1 Hz, 15% tensile strain of the OPS harvesters connected in series (a, b) and in parallel (c, d). Gravimetric and absolute performance for the OPS harvesters are shown in (a, c) and (b, d), respectively. The volumetric peak power, average power, and energy per cycle for a 1 Hz, 30% cyclic tensile strain of the OPS harvesters connected in series (e) and in parallel (f). Separate electrochemical cells were used for each OPS harvester. The electrolyte was 0.1 M aqueous LiCl electrolyte and applied stretch was sinusoidal. For twistron harvesters, the equivalent

internal impedance can be qualitatively described by a simple R - C model. The total electrical impedance of twistron harvesters is $Z_{\text{harvester}} = R_{\text{internal}} + 1/(j\omega C)$, where R_{internal} is internal resistance of the twistron yarn, j is $\sqrt{-1}$, ω is the angular frequency, and C is the electric double-layer capacitance. Connecting twistron harvesters in parallel will proportionally reduce the R_{internal} and proportionally increase the C in this R - C circuit, so the total electrical impedance of the system is proportionally decreased by increasing the number of twistron harvesters that are connected in parallel. Though the output voltage is not changed by connecting harvesters in parallel, the proportionally decreased total electrical impedance will proportionally increase the output current. Hence, the gravimetric power and energy output are little affected by upscaling the network by placing equivalent twistron harvesters in parallel.



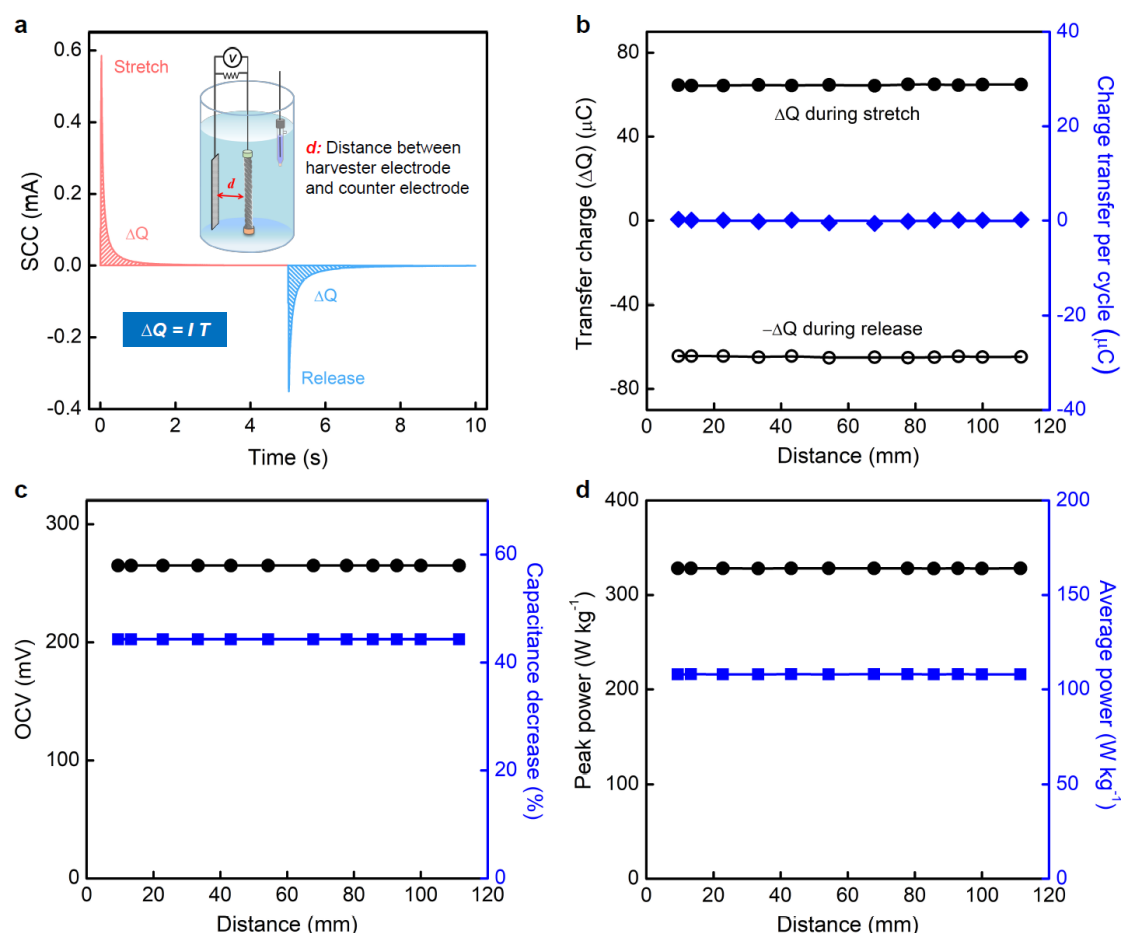
Supplementary Figure 57. The use of an integrated harvester array to charge a supercapacitor and power various electronic devices. **a**, The generated OCV for 1 Hz, 30% sinusoidal stretch of four 2.2-cm-long, 0.80-mg-weight 3-ply yarn harvesters connected in series. **b**, The time dependence of the rectified voltage obtained using a Schottky diode full-bridge rectifier. **c**, Photograph of the integrated booster converter circuit. **d**, Photograph of a plied CNT yarn harvester array that comprises four 0.80-mg, 2.2-cm-long, plied CNT yarn harvesters. Four twisted yarns with a twist density of 10 turns cm^{-1} were used as counter electrodes. **e**, Illustration of the integrated boost converter circuit. **f**, Supercapacitor voltage versus time during charging a $220\text{-}\mu\text{F}$ supercapacitor to 2.8 V by using the boost converter circuit of (c). The charged

supercapacitor (220 μF , 2.8 V) was used to power (g) five 2.7 V green LEDs, (h) a 2.5 V electronic watch, and (i) a 1.5 V digital temperature/humidity monitor having a 4.5 x 5.7 cm (2.8-inch) liquid-crystal display. We demonstrated the use of our plied CNT yarn harvesters to power larger devices, including an electronic watch, a digital temperature/humidity monitor, and simultaneously powering 5 LEDs. The above demonstrations were realized by connecting four 0.80-mg, 2.2-cm-long, plied CNT yarn harvesters in series (Supplementary Fig. 57a,d). Since the OCV is an AC output, a Schottky diode full-bridge rectifier was used to convert this AC output to DC. As a result, the maximum rectified voltage for these four harvesters was ~ 0.5 V (Supplementary Fig. 57b). To further increase the output voltage, we integrated a passive voltage booster (LTC3108EDE, Linear Technology Corporation) into the circuit, as shown in Supplementary Fig. 57c,e. Using this boost converter circuit, 45 stretch-release cycles for this 3.20-mg harvester array charged a 220- μF supercapacitor to 2.8 V (Supplementary Fig. 57f). The energy stored in the capacitor was used to power five 2.7 V green LEDs, a 2.5 V electronic watch, and a 1.5 V digital temperature/humidity monitor having a 4.5 x 5.7 cm (2.8-inch) liquid-crystal display (Supplementary Fig. 57g-i).

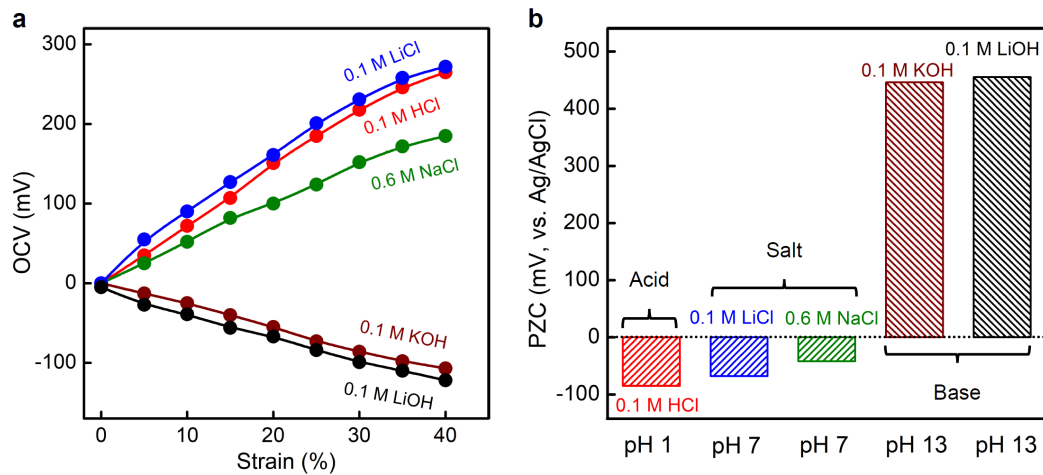


Supplementary Figure 58. Demonstration that the energy output per weight of the harvesting electrode or electrodes is nearly unchanged when a single 3-ply harvesting electrode and a static counter electrode is replaced by a 3-ply harvesting electrode and an identical 3-ply counter electrode that undergo oppositely directed deformations. The time dependence of (a) the applied strain, (b) the inter-electrode voltage generated by applying this strain only to the working electrode (WE), and (c) the inter-electrode voltage generated by applying this strain only to the counter electrode (CE) for an output-power-maximizing load resistance (112 Ω). The time dependence of (d) applied strain, (e) generated inter-electrode voltage for an output-power-maximizing load resistance of 98 Ω , and (f) gravimetric output power when working electrode and counter electrode were stretched 180° out-of-phase at 1 Hz. The peak power

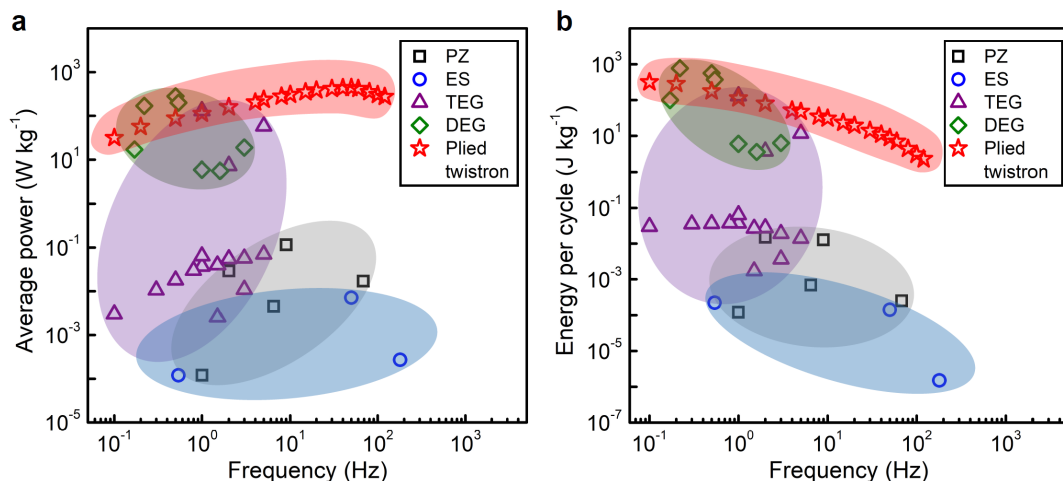
(311 W kg^{-1}) and average power (148 W kg^{-1}) for this seesaw-structure harvester were normalized to the total weight ($\sim 0.64 \text{ mg}$) of the two electrodes. For the one-electrode energy harvesting, the peak power and average power for a 1 Hz, 40% strain of a 3-ply yarn harvester were 328 W kg^{-1} and 108 W kg^{-1} , respectively, when normalized to the weight of single working electrode. Since the single harvesting electrode and the dual-harvesting electrode results approximately agree, we are justified in ignoring the counter electrodes weight. For all these measurements, the used electrolyte was 0.1 M aqueous HCl.



Supplementary Figure 59. The transferred charge (ΔQ) between shorted electrodes for 10% square-wave strain of an OPS harvester when stretched and stretch-released at 0.1 Hz in 0.1 M aqueous HCl electrolyte. a, The SCC versus time for the OPS harvester when stretched and stretch-released. The transferred charge (ΔQ) for stretch (red areas) and stretch-release (blue areas) are the areas under the SCC curves. Inset: Illustration of an OPS harvester in the electrolyte. The distance between harvester working electrode and counter electrode was $d = 50 \text{ mm}$. **b,** The dependence of transferred charge for the OPS harvester on the distance between the harvester working electrode and counter electrode. The inter-electrode separation dependence of **(c)** OCV and percent capacitance decrease and **(d)** peak power and average power (at 1 Hz) for the OPS harvester. These results show that harvester performance was negligibly affected by inter-electrode separations between 9.4 and 112 mm.



Supplementary Figure 60. The OCV and PZC for OPS harvesters operated in aqueous electrolytes having different pHs. a, The OCV versus tensile strain for an OPS harvester sinusoidally stretched at 1 Hz in 0.1 M HCl (pH 1), 0.1 M LiCl (pH 7), 0.6 M NaCl (pH 7), 0.1 M LiOH (pH 13), and 0.1 M KOH (pH 13) aqueous electrolytes. **b,** The PZC for the OPS harvester in the above electrolytes. We investigated the effect of the electrolyte's pH on the OCV and PZC for OPS harvesters. The sign of the generated OCV was opposite for high-pH electrolytes than for low-pH and neutral pH electrolytes, since electron injection occurs for a high-pH electrolyte (0.1 M LiOH and 0.1 M KOH, pH = 13) and hole injection occurs for a low-pH electrolyte (0.1 M HCl, pH = 1) and a neutral-pH electrolyte (0.1 M LiCl and 0.6 M NaCl, pH = 7)¹. These results indicate that our plied twistrans can be used in various corrosive chemical environments where strong acids or strong bases exist.



Supplementary Figure 61. Comparison of output average power and energy of our plied twistran harvesters and prior-art material-based MEHs over a wide frequency range. Comparison of (a) gravimetric average power and (b) energy per cycle versus frequency of our plied twistran harvesters and piezoelectric (PZ), electrostatic (ES), triboelectric (TEG), and dielectric elastomer (DEG) harvesters. Supplementary Table 1 provides the references and data values for literature reports. For frequencies between 2 and 120 Hz, the 3-ply OPS harvesters provide a higher average power and a higher energy per cycle than prior-art material-based harvesters. There are few reports in the literature for average

power and energy per cycle for prior-art harvesters. While giant average power gravimetric densities have been obtained for very large electromagnetic generators (13 kW kg^{-1})⁵, Zhonglin Wang's group has shown that the output power for electromagnetic generators dramatically decreases when the weight of the electromagnetic generator is decreased^{6,7}.

Supplementary Table 1. Comparison of average power and energy per cycle for our plied yarn harvesters and other previously reported, material-based harvesters.

Ref.	Harvester type	Harvester weight	Frequency	Average power	Energy per cycle	Energy conversion efficiency
		(kg)	(Hz)	(W kg ⁻¹)	(J kg ⁻¹ per cycle)	(%)
Our work	Plied twistron	2.50 10 ⁻⁷	0.1	31.5	315	14.3
	Plied twistron	2.50 10 ⁻⁷	1	112.5	112.5	5.0
	Plied twistron	2.50 10 ⁻⁷	10	305.9	30.59	--
	Plied twistron	2.50 10 ⁻⁷	30	417	13.9	--
	Plied twistron	2.50 10 ⁻⁷	50	438	8.76	--
	Plied twistron	2.50 10 ⁻⁷	120	196.8	1.64	--
8	Piezoelectric	7.71 10 ⁻²	9	0.115	1.28 10 ⁻²	--
9	Piezoelectric	3.39 10 ⁻³	68.1	1.7 10 ⁻²	2.49 10 ⁻⁴	--
10	Piezoelectric	3.53 10 ⁻¹⁶	1	1.21 10 ⁻⁴	1.21 10 ⁻⁴	5.58
11	Piezoelectric	4.0 10 ⁻²	6.5	4.5 10 ⁻³	6.92 10 ⁻⁴	--
12	Piezoelectric	3.6 10 ⁻²	2	2.9 10 ⁻²	1.5 10 ⁻²	
13	Electrostatic	5.00 10 ⁻³	50	0.71 10 ⁻²	1.42 10 ⁻⁴	--
14	Electrostatic	6.00 10 ⁻⁵	180	2.71 10 ⁻⁴	1.51 10 ⁻⁶	--
15	Electrostatic	1.92 10 ⁻⁶	0.54	1.20 10 ⁻⁴	2.22 10 ⁻⁴	~ 1.0
16	Triboelectric	8.80 10 ⁻⁴	1	130.55	130.55	4.30
17	Triboelectric-Piezoelectric Hybrid	1.58 10 ⁻³	5	58.48	11.70	--
7	Triboelectric	--	5	7.00 10 ⁻²	1.40 10 ⁻²	--
7	Triboelectric	--	3	5.70 10 ⁻²	1.90 10 ⁻²	--
7	Triboelectric	--	2	5.50 10 ⁻²	2.75 10 ⁻²	--
7	Triboelectric	--	1.5	4.00 10 ⁻²	2.67 10 ⁻²	--
7	Triboelectric	--	1	3.70 10 ⁻²	3.70 10 ⁻²	--

7	Triboelectric	--	0.8	$3.00 \cdot 10^{-2}$	$3.75 \cdot 10^{-2}$	--
7	Triboelectric	--	0.5	$1.8 \cdot 10^{-2}$	$3.60 \cdot 10^{-2}$	--
7	Triboelectric	--	0.3	$1.06 \cdot 10^{-2}$	$3.53 \cdot 10^{-2}$	--
7	Triboelectric	--	0.1	$3.00 \cdot 10^{-3}$	$3.00 \cdot 10^{-2}$	--
18	Triboelectric	$8.96 \cdot 10^{-3}$	1.5	$2.58 \cdot 10^{-3}$	$1.72 \cdot 10^{-3}$	--
19	Triboelectric	--	3	$1.1 \cdot 10^{-2}$	$3.67 \cdot 10^{-3}$	20
20	Triboelectric	$2.50 \cdot 10^{-5}$	2	7.41	3.71	--
21	Triboelectric	--	1	$6.4 \cdot 10^{-2}$	$6.4 \cdot 10^{-2}$	--
22	Dielectric Elastomer	$6.00 \cdot 10^{-4}$	0.5	280	560	27 (Bias voltage: 3 kV)
23	Dielectric Elastomer	$6.00 \cdot 10^{-4}$	0.22	170	772.73	--
24	Dielectric Elastomer	$3.50 \cdot 10^{-4}$	3	37.8	12.6	7.8
25	Dielectric Elastomer	$4.83 \cdot 10^{-5}$	1	6	6	--
26	Dielectric Elastomer	$3.20 \cdot 10^{-4}$	1.6	5.65	3.53	--
27	Dielectric Elastomer	$1.53 \cdot 10^{-3}$	0.17	17	102	7.5 (Bias voltage: 2.5 kV)
28	Dielectric Elastomer	--	0.54	200	369	14.9

Supplementary Table 2. Comparison of peak power and peak power/frequency for our plied yarn harvesters and other previously reported, material-based harvesters.

If the literature report did not indicate if the reported power was peak or average power, it was assumed to be peak power.

Ref.	Harvester type	Harvester weight	Frequency	Peak power	Peak power /frequency	Energy conversion efficiency
		(kg)	(Hz)	(W kg ⁻¹)	(J kg ⁻¹ per cycle)	(%)
Our work	Plied twistron	2.50 10 ⁻⁷	0.1	98.22	982.2	14.3
	Plied twistron	2.50 10 ⁻⁷	1	345	345	5.0
	Plied twistron	2.50 10 ⁻⁷	10	1095.5	109.55	--
	Plied twistron	2.50 10 ⁻⁷	30	1456.2	48.54	--
	Plied twistron	2.50 10 ⁻⁷	50	1475	29.5	--
	Plied twistron	2.50 10 ⁻⁷	120	788.45	6.57	--
29	Piezoelectric	1.95 10 ⁻⁵	0.3	60.9	203	--
30	Piezoelectric	1.27 10 ⁻¹⁴	0.5	4.37	8.74	5.08
31	Piezoelectric	2.71 10 ⁻²	30	1.94	6.46 10 ⁻²	2.08
31	Piezoelectric	1.30 10 ⁻²	30	1.18	3.93 10 ⁻²	6.34
32	Piezoelectric	5.00 10 ⁻⁴	0.4	0.5	1.25	3.04
33	Piezoelectric	4.00 10 ⁻³	600	0.23	3.83 10 ⁻⁴	--
34	Piezoelectric	9.52 10 ⁻³	30	9.5 10 ⁻²	3.15 10 ⁻³	--
35	Piezoelectric	9.56 10 ⁻⁴	0.3	1.5 10 ⁻²	5.00 10 ⁻²	--
36	Piezoelectric	1.98 10 ⁻¹⁶	0.7	1.25 10 ⁻²	1.78 10 ⁻²	--
37	Piezoelectric	4.00 10 ⁻³	147	1.42	9.63 10 ⁻³	--
38	Piezoelectric	5.92 10 ⁻⁷	3	11.4	3.80	--
39	Piezoelectric	2.60 10 ⁻⁵	263	5.77 10 ⁻³	2.19 10 ⁻⁵	--
40	Piezoelectric	1.0 10 ⁻⁶	461.2	2.15	4.66 10 ⁻³	--

41	Piezoelectric	$4.6 \cdot 10^{-3}$	10	$2.2 \cdot 10^{-2}$	$2.2 \cdot 10^{-3}$	--
42	Piezoelectric	$2.3 \cdot 10^{-5}$	36	$3.91 \cdot 10^{-3}$	$1.09 \cdot 10^{-4}$	--
43	Piezoelectric	$1.17 \cdot 10^{-2}$	398	$4.52 \cdot 10^{-3}$	$1.14 \cdot 10^{-5}$	--
44	Piezoelectric	$4.22 \cdot 10^{-4}$	1	33.18	33.18	--
45	Piezoelectric	$1.81 \cdot 10^{-4}$	60	53.6	0.89	--
46	Piezoelectric	--	13	$6.18 \cdot 10^{-2}$	$4.75 \cdot 10^{-3}$	--
12	Piezoelectric	$3.6 \cdot 10^{-2}$	2	0.43	0.22	--
47	Piezoelectric	$9.6 \cdot 10^{-6}$	1	0.18	0.18	--
48	Piezoelectric	$5.0 \cdot 10^{-4}$	0.35	$2.12 \cdot 10^{-2}$	$6.1 \cdot 10^{-2}$	--
49	Electrostatic	$1.04 \cdot 10^{-1}$	50	$1.01 \cdot 10^{-2}$	$2.02 \cdot 10^{-4}$	60% (peak power efficiency)
50	Electrostatic	$5.80 \cdot 10^{-3}$	2	$6.90 \cdot 10^{-3}$	$3.45 \cdot 10^{-3}$	--
15	Electrostatic	$1.92 \cdot 10^{-6}$	0.54	$2.82 \cdot 10^{-4}$	$5.22 \cdot 10^{-4}$	~ 1.0
51	Electrostatic	$6.6 \cdot 10^{-5}$	150	$3.3 \cdot 10^{-2}$	$2.22 \cdot 10^{-4}$	--
52	Electrostatic	$6.6 \cdot 10^{-5}$	109	$1.97 \cdot 10^{-2}$	$1.81 \cdot 10^{-4}$	--
53	Electrostatic	$1.0 \cdot 10^{-4}$	63	$1.0 \cdot 10^{-2}$	$1.59 \cdot 10^{-4}$	--
54	Electrostatic	$5.0 \cdot 10^{-4}$	28	$3.0 \cdot 10^{-3}$	$1.07 \cdot 10^{-4}$	--
55	Electrostatic	$2.0 \cdot 10^{-5}$	95	$4.75 \cdot 10^{-2}$	$5.0 \cdot 10^{-4}$	--
56	Electrostatic	$8.8 \cdot 10^{-5}$	139	0.61	$4.41 \cdot 10^{-3}$	--
57	Electrostatic	$1.04 \cdot 10^{-4}$	136	$5.35 \cdot 10^{-2}$	$3.93 \cdot 10^{-4}$	--
16	Triboelectric	$8.80 \cdot 10^{-4}$	1	265	265	4.30
58	Triboelectric	$2.60 \cdot 10^{-4}$	0.33	7.44	22.60	--
59	Triboelectric	$7.00 \cdot 10^{-3}$	10	0.6	0.06	--
60	Triboelectric	$6.51 \cdot 10^{-4}$	3	0.35	0.12	--
61	Triboelectric	$5.33 \cdot 10^{-2}$	10	$2.63 \cdot 10^{-3}$	$2.63 \cdot 10^{-4}$	--

62	Triboelectric	$1.0 \cdot 10^{-4}$	5	0.28	$5.60 \cdot 10^{-2}$	--
63	Triboelectric	$2.54 \cdot 10^{-2}$	4	1.86	0.47	--
64	Triboelectric	$5.59 \cdot 10^{-4}$	0.5	8.94	17.88	--
65	Triboelectric	$2.69 \cdot 10^{-4}$	1.5	0.16	0.11	--
66	Triboelectrification	$5.40 \cdot 10^{-4}$	0.8	$3.52 \cdot 10^{-3}$	$4.40 \cdot 10^{-3}$	--
67	Triboelectric	0.05	1.25	0.24	0.192	16.34
68	Triboelectric	--	3.3	2.21	0.67	--
69	Triboelectric	$3.85 \cdot 10^{-3}$	1.5	1.17	0.78	--
70	Triboelectric	$8.78 \cdot 10^{-5}$	4.5	42.02	9.34	--
71	Triboelectric	$1.27 \cdot 10^{-1}$	1	0.131	0.131	--
72	Triboelectric	$8.50 \cdot 10^{-2}$	3.83	$5.67 \cdot 10^{-2}$	$1.48 \cdot 10^{-2}$	--
73	Triboelectric	$1.44 \cdot 10^{-3}$	1.43	11.64	8.14	--
74	Triboelectric	$4.06 \cdot 10^{-1}$	30	$1.6 \cdot 10^{-2}$	$5.33 \cdot 10^{-4}$	--
75	Triboelectric	$1.29 \cdot 10^{-2}$	10	$1.55 \cdot 10^{-2}$	$1.55 \cdot 10^{-3}$	--
76	Triboelectric	$3.2 \cdot 10^{-3}$	34	0.84	$2.47 \cdot 10^{-2}$	--
77	Triboelectric	0.2	1	0.18	0.18	--
78	Triboelectric	$1.94 \cdot 10^{-3}$	6.67	8.08	1.21	--
79	Triboelectric	$6.02 \cdot 10^{-1}$	1	$1.83 \cdot 10^{-2}$	$1.83 \cdot 10^{-2}$	--
80	Triboelectric	$3.70 \cdot 10^{-2}$	2	$1.07 \cdot 10^{-2}$	$5.37 \cdot 10^{-3}$	--
81	Triboelectric	$1.57 \cdot 10^{-2}$	2.5	5.17	2.07	--
82	Triboelectric	$6.80 \cdot 10^{-7}$	2	895	447.5	--
83	Triboelectric	$2.30 \cdot 10^{-4}$	1	$4.24 \cdot 10^{-2}$	$4.24 \cdot 10^{-2}$	--
84	Triboelectric	$3.31 \cdot 10^{-2}$	2	0.21	0.11	--
85	Triboelectric	0.2	11.6	$1.3 \cdot 10^{-2}$	$1.12 \cdot 10^{-3}$	--

86	Triboelectric	$3.3 \cdot 10^{-2}$	0.5	0.17	0.34	--
87	Triboelectric	--	0.35	0.62	1.77	--
88	Dielectric Elastomer	$4.4 \cdot 10^{-3}$	0.7	197	281.43	18 (Bias voltage: 4 kV)
89	Dielectric Elastomer	--	0.1	13	130	40 (Bias voltage: 4 kV)
90	Dielectric Elastomer	--	0.25	16.3	65.2	5.7 (Bias voltage: 4 kV)

Supplementary References

1. Kim, S. H. et al. Harvesting electrical energy from carbon nanotube yarn twist. *Science* **357**, 773-778 (2017).
2. Inoue, H. et al. The critical role of the forest morphology for dry drawability of few-walled carbon nanotubes. *Carbon* **158**, 662-671 (2020).
3. Xu, M., Futaba, D. N., Yumura, M. & Hata, K. Alignment control of carbon nanotube forest from random to nearly perfectly aligned by utilizing the crowding effect. *ACS Nano* **6**, 5837-5844 (2012).
4. Zhang, M. et al. Self-powered, electrochemical carbon nanotube pressure sensors for wave monitoring. *Adv. Funct. Mater.* **30**, 2004564 (2020).
5. <https://www.calnetix.com/high-speed-electric-motor-generators>.
6. Lu, P. et al. Swing-structured triboelectric-electromagnetic hybridized nanogenerator for breeze wind energy harvesting. *Advanced Materials Technologies*, 2100496 (2021).
7. Zi, Y. et al. Harvesting low-frequency (<5 Hz) irregular mechanical energy: A possible killer application of triboelectric nanogenerator. *ACS Nano* **10**, 4797-4805 (2016).
8. Kim, K. et al. Performance of unimorph cantilever generator using Cr/Nb doped Pb(Zr_{0.54}Ti_{0.46})O₃ thick film for energy harvesting device applications. *J. Eur. Ceram. Soc.* **33**, 305-311 (2013).
9. Sharpes, N., Abdelkefi, A. & Priya, S. Two-dimensional concentrated-stress low-frequency piezoelectric vibration energy harvesters. *Appl. Phys. Lett.* **107**, 93901 (2015).
10. Hinchet, R. et al. Performance optimization of vertical nanowire-based piezoelectric nanogenerators. *Adv. Funct. Mater.* **24**, 971-977 (2014).
11. Wu, N., He, Y. & Fu, J. Bistable energy harvester using easy snap-through performance to increase output power. *Energy* **226**, 120414 (2021).
12. Wang, B. et al. Woodpecker-mimic two-layer band energy harvester with a piezoelectric array for powering wrist-worn wearables. *Nano Energy* **89**, 106385 (2021).
13. Boisseau, S., Despesse, G., Ricart, T., Defay, E. & Sylvestre, A. Cantilever-based electret energy harvesters. *Smart Mater. Struct.* **20**, 105013 (2011).
14. Crovetto, A., Wang, F. & Hansen, O. An electret-based energy harvesting device with a wafer-level fabrication process. *J. Micromech. Microeng.* **23**, 114010 (2013).
15. Yu, X. et al. A novel photoelectric conversion yarn by integrating photomechanical actuation and the electrostatic effect. *Adv. Mater.* **28**, 10744-10749 (2016).
16. Kim, D. et al. High-performance nanopattern triboelectric generator by block copolymer lithography. *Nano Energy* **12**, 331-338 (2015).
17. Jung, W. et al. High output piezo/triboelectric hybrid generator. *Sci. Rep.-UK* **5** (2015).
18. Guo, H. et al. Ultralight cut-paper-based self-charging power unit for self-powered portable electronic and medical systems. *ACS Nano* **11**, 4475-4482 (2017).
19. Dong, K. et al. Versatile core-sheath yarn for sustainable biomechanical energy harvesting and real-time human-interactive sensing. *Adv. Energy Mater.* **8**, 1801114 (2018).
20. Yan, W. et al. Flexible film-discharge-switch assisted universal power management system for the four operation modes of triboelectric nanogenerators. *Adv. Energy Mater.* **11**, 2103677 (2022).
21. Chen, X. et al. Electron trapping & blocking effect enabled by MXene/TiO₂ intermediate layer for charge regulation of triboelectric nanogenerators. *Nano Energy*, 107236 (2022).

22. Huang, J., Shian, S., Suo, Z. & Clarke, D. R. Maximizing the energy density of dielectric elastomer generators using equi-biaxial loading. *Adv. Funct. Mater.* **23**, 5056-5061 (2013).
23. Shian, S., Huang, J., Zhu, S. & Clarke, D. R. Optimizing the electrical energy conversion cycle of dielectric elastomer generators. *Adv. Mater.* **26**, 6617-6621 (2014).
24. McKay, T., O'Brien, B., Calius, E. & Anderson, I. An integrated, self-priming dielectric elastomer generator. *Appl. Phys. Lett.* **97**, 62911 (2010).
25. Jean-Mistral, C., Vu Cong, T. & Sylvestre, A. Advances for dielectric elastomer generators: Replacement of high voltage supply by electret. *Appl. Phys. Lett.* **101**, 162901 (2012).
26. McKay, T. G., Rosset, S., Anderson, I. A. & Shea, H. Dielectric elastomer generators that stack up. *Smart Mater. Struct.* **24**, 15014 (2014).
27. Kaltseis, R. et al. Method for measuring energy generation and efficiency of dielectric elastomer generators. *Appl. Phys. Lett.* **99**, 162904 (2011).
28. Kaltseis, R. et al. Natural rubber for sustainable high-power electrical energy generation. *RSC Adv.* **4**, 27905-27913 (2014).
29. Hwang, G. et al. Self-powered cardiac pacemaker enabled by flexible single crystalline PMN-PT piezoelectric energy harvester. *Adv. Mater.* **26**, 4880-4887 (2014).
30. Wu, W. et al. Piezoelectricity of single-atomic-layer MoS₂ for energy conversion and piezotronics. *Nature* **514**, 470-474 (2014).
31. Cho, K., Park, H., Heo, J. S. & Priya, S. Structure-performance relationships for cantilever-type piezoelectric energy harvesters. *J. Appl. Phys.* **115**, 204108 (2014).
32. Hwang, G. et al. Self-powered wireless sensor node enabled by an aerosol-deposited PZT flexible energy harvester. *Adv. Energy Mater.* **6**, 1600237 (2016).
33. <https://www.cornestech.co.jp/images/uploads/file/products/pdf/bolt.pdf>.
34. Sodano, H. A., Park, G. & Inman, D. J. Estimation of electric charge output for piezoelectric energy harvesting. *Strain* **40**, 49-58 (2004).
35. Jeong, C. K., Park, K., Ryu, J., Hwang, G. & Lee, K. J. Large-area and flexible lead-free nanocomposite generator using alkaline niobate particles and metal nanorod filler. *Adv. Funct. Mater.* **24**, 2620-2629 (2014).
36. Hu, Y. et al. A nanogenerator for energy harvesting from a rotating tire and its application as a self-powered pressure/speed sensor. *Adv. Mater.* **23**, 4068-4071 (2011).
37. <http://info.mide.com/piezo-products/download-piezo-products-datasheets>.
38. Siddiqui, S. et al. High-performance flexible lead-free nanocomposite piezoelectric nanogenerator for biomechanical energy harvesting and storage. *Nano Energy* **15**, 177-185 (2015).
39. Aktakka, E. E., Peterson, R. L. & Najafi, K. (IEEE, 2010), pp. 31-35.
40. Shen, D. et al. The design, fabrication and evaluation of a MEMS PZT cantilever with an integrated Si proof mass for vibration energy harvesting. *J. Micromech. Microeng.* **18**, 55017 (2008).
41. Tang, Q. C., Yang, Y. L. & Li, X. Bi-stable frequency up-conversion piezoelectric energy harvester driven by non-contact magnetic repulsion. *Smart Mater. Struct.* **20**, 125011 (2011).
42. Liu, H., Tay, C. J., Quan, C., Kobayashi, T. & Lee, C. Piezoelectric MEMS energy harvester for low-frequency vibrations with wideband operation range and steadily increased output power. *J. Microelectromech. S.* **20**, 1131-1142 (2011).
43. Aktakka, E. E. & Najafi, K. Three-axis piezoelectric vibration energy harvester. *in 2015*

- 28th IEEE International Conference on Micro Electro Mechanical Systems (MEMS) (2015).
44. Gao, X. et al. Giant piezoelectric coefficients in relaxor piezoelectric ceramic PNN-PZT for vibration energy harvesting. *Adv. Funct. Mater.* **28**, 1706895 (2018).
 45. Kang, M. G. et al. High power magnetic field energy harvesting through amplified magneto-mechanical vibration. *Adv. Energy Mater.* **8**, 1703313 (2018).
 46. Fu, J., Hou, Y., Zheng, M. & Zhu, M. Flexible piezoelectric energy harvester with extremely high power generation capability by sandwich structure design strategy. *ACS Appl. Mater. Inter.* **12**, 9766-9774 (2020).
 47. Jin, D. W. et al. Polarization- and electrode-optimized polyvinylidene fluoride films for harsh environmental piezoelectric nanogenerator applications. *Small* **14**, 2007289 (2021).
 48. Raj, N. P. M. J., KS, A., Khandelwal, G. & Kim, S. Method for fabricating highly crystalline polyvinylidene fluoride for piezoelectric energy harvesting and vibration sensor applications. *Sustainable Energy & Fuels* **6**, 674-681 (2022).
 49. Despesse, G. et al. Fabrication and characterization of high damping electrostatic micro devices for vibration energy scavenging. in *Symposium on Design, Test, Integration and Packaging of MEMS/MOEMS (DTIP 2005), June 1-3* (2005).
 50. Naruse, Y., Matsubara, N., Mabuchi, K., Izumi, M. & Suzuki, S. Electrostatic micro power generation from low-frequency vibration such as human motion. *J. Micromech. Microeng.* **19**, 94002 (2009).
 51. Guillemet, R. et al. Wideband MEMS electrostatic vibration energy harvesters based on gap-closing interdigitated combs with a trapezoidal cross section. in *2013 IEEE 26th International Conference on Micro Electro Mechanical Systems (MEMS)*, 817-820 (2013).
 52. Cottone, F. et al. Non-linear MEMS electrostatic kinetic energy harvester with a tunable multistable potential for stochastic vibrations. in *2013 Transducers & Eurosensors XXVII: The 17th International Conference on Solid-State Sensors, Actuators and Microsystems (TRANSDUCERS & EUROSENSORS XXVII)* (2013).
 53. Suzuki, Y., Miki, D., Edamoto, M. & Honzumi, M. A MEMS electret generator with electrostatic levitation for vibration-driven energy-harvesting applications. *J. Micromech. Microeng.* **20**, 104002 (2010).
 54. Minakawa, Y., Chen, R. & Suzuki, Y. X-shaped-spring enhanced MEMS electret generator for energy harvesting. in *2013 Transducers & Eurosensors XXVII: The 17th International Conference on Solid-State Sensors, Actuators and Microsystems (TRANSDUCERS & EUROSENSORS XXVII)* (2013).
 55. Tao, K., Lye, S. W., Miao, J., Tang, L. & Hu, X. Out-of-plane electret-based MEMS energy harvester with the combined nonlinear effect from electrostatic force and a mechanical elastic stopper. *J. Micromech. Microeng.* **25**, 104014 (2015).
 56. Asanuma, H., Hara, M., Oguchi, H. & Kuwano, H. Nonlinear restoring force of spring with stopper for ferroelectric dipole electret-based electrostatic vibration energy harvesters. *AIP Adv.* **6**, 75206 (2016).
 57. Zhang, Y. et al. Micro electrostatic energy harvester with both broad bandwidth and high normalized power density. *Appl. Energ.* **212**, 362-371 (2018).
 58. Fan, F., Tian, Z. & Lin Wang, Z. Flexible triboelectric generator. *Nano Energy* **1**, 328-334 (2012).
 59. Bai, P. et al. Integrated multilayered triboelectric nanogenerator for harvesting

- biomechanical energy from human motions. *ACS Nano* **7**, 3713-3719 (2013).
60. Zhong, J. et al. Finger typing driven triboelectric nanogenerator and its use for instantaneously lighting up LEDs. *Nano Energy* **2**, 491-497 (2013).
 61. Zhang, C., Tang, W., Han, C., Fan, F. & Wang, Z. L. Theoretical comparison, equivalent transformation, and conjunction operations of electromagnetic induction generator and triboelectric nanogenerator for harvesting mechanical energy. *Adv. Mater.* **26**, 3580-3591 (2014).
 62. Li, T. et al. Lightweight triboelectric nanogenerator for energy harvesting and sensing tiny mechanical motion. *Adv. Funct. Mater.* **26**, 4370-4376 (2016).
 63. Gao, S. et al. Triboelectric nanogenerator powered electrochemical degradation of organic pollutant using pt-free carbon materials. *ACS Nano* **11**, 3965-3972 (2017).
 64. Guo, H. et al. Self-sterilized flexible single-electrode triboelectric nanogenerator for energy harvesting and dynamic force sensing. *ACS Nano* **11**, 856-864 (2017).
 65. Pu, X. et al. Ultrastretchable, transparent triboelectric nanogenerator as electronic skin for biomechanical energy harvesting and tactile sensing. *Sci Adv* **3**, e1700015 (2017).
 66. Kwak, S. S. et al. Triboelectrification-induced large electric power generation from a single moving droplet on graphene/polytetrafluoroethylene. *ACS Nano* **10**, 7297-7302 (2016).
 67. Zhang, Z., Chen, Y., Debeli, D. K. & Guo, J. S. Facile method and novel dielectric material using a nanoparticle-doped thermoplastic elastomer composite fabric for triboelectric nanogenerator applications. *ACS Appl. Mater. Inter.* **10**, 13082-13091 (2017).
 68. Gong, J. et al. Towards truly wearable energy harvesters with full structural integrity of fiber materials. *Nano Energy* **58**, 365-374 (2019).
 69. Zhang, Z., Sun, X., Chen, Y., Debeli, D. K. & Guo, J. Comprehensive dependence of triboelectric nanogenerator on dielectric thickness and external impact for high electric outputs. *J. Appl. Phys.* **124**, 45106 (2018).
 70. Salauddin, M. et al. A novel MXene/Ecoflex nanocomposite-coated fabric as a highly negative and stable friction layer for high-output triboelectric nanogenerators. *Adv. Energy Mater.* **11**, 2002832 (2021).
 71. Liang, X. et al. Spherical triboelectric nanogenerator based on spring-assisted swing structure for effective water wave energy harvesting. *Nano Energy* **83**, 105836 (2021).
 72. Liu, S. et al. Magnetic switch structured triboelectric nanogenerator for continuous and regular harvesting of wind energy. *Nano Energy* **83**, 105851 (2021).
 73. Wang, H. L., Guo, Z. H., Zhu, G., Pu, X. & Wang, Z. L. Boosting the power and lowering the impedance of triboelectric nanogenerators through manipulating the permittivity for wearable energy harvesting. *ACS Nano* **15**, 7513-7521 (2021).
 74. Wang, Y. et al. Gravity triboelectric nanogenerator for the steady harvesting of natural wind energy. *Nano Energy* **82**, 105740 (2021).
 75. Gao, Y. et al. A robust rolling-mode direct-current triboelectric nanogenerator arising from electrostatic breakdown effect. *Nano Energy* **85**, 106014 (2021).
 76. Ye, C. et al. A triboelectric-electromagnetic hybrid nanogenerator with broadband working range for wind energy harvesting and a self-powered wind speed sensor. *ACS Energy Letters*, 1443-1452 (2021).
 77. Zhang, C. et al. Bifilar-pendulum-assisted multilayer-structured triboelectric nanogenerators for wave energy harvesting. *Adv. Energy Mater.* **11**, 2003616 (2021).

78. Jin, L. et al. Free-fixed rotational triboelectric nanogenerator for self-powered real-time wheel monitoring. *Advanced Materials Technologies* **6**, 2000918 (2021).
79. Yang, Y. et al. Triboelectric nanogenerator with double rocker structure design for ultra-low-frequency wave full-stroke energy harvesting. *Extreme Mechanics Letters* **46**, 101338 (2021).
80. Jiang, B., Long, Y., Pu, X., Hu, W. & Wang, Z. L. A stretchable, harsh condition-resistant and ambient-stable hydrogel and its applications in triboelectric nanogenerator. *Nano Energy* **86**, 106086 (2021).
81. Li, Y. et al. Improved output performance of triboelectric nanogenerator by fast accumulation process of surface charges. *Adv. Energy Mater.* **11**, 2100050 (2021).
82. Wang, H., Guo, Z., Pu, X. & Wang, Z. Ultralight iontronic triboelectric mechanoreceptor with high specific outputs for epidermal electronics. *Nano-Micro Letters* **14**, 1-14 (2022).
83. Jiang, Y. et al. Stretchable, washable, and ultrathin triboelectric nanogenerators as skin-like highly sensitive self-powered haptic sensors. *Adv. Funct. Mater.* **31**, 2005584 (2021).
84. Liu, L., Shi, Q., Sun, Z. & Lee, C. Magnetic-interaction assisted hybridized triboelectric-electromagnetic nanogenerator for advanced human-machine interfaces. *Nano Energy* **86**, 106154 (2021).
85. Yun, Y. et al. Exo-shoe triboelectric nanogenerator: Toward high-performance wearable biomechanical energy harvester. *Nano Energy* **80**, 105525 (2021).
86. Wu, Z. et al. Highly durable and easily integrable triboelectric foam for active sensing and energy harvesting applications. *Advanced Materials Technologies* **6**, 2000737 (2021).
87. Zhu, J. et al. A self-healing triboelectric nanogenerator based on feathers for sensing and energy harvesting. *Adv. Funct. Mater.*, 2100039 (2021).
88. Moretti, G. et al. Resonant wave energy harvester based on dielectric elastomer generator. *Smart Mater. Struct.* **27**, 35015 (2018).
89. Jiang, Y. et al. Optimizing energy harvesting performance of cone dielectric elastomer generator based on VHB elastomer. *Nano Energy* **71**, 104606 (2020).
90. Song, Z., Sathin, S., Li, W., Ohyama, K. & Zhu, S. Dielectric elastomer generator with diaphragm configuration. *MATEC Web of Conferences* **192**, 1032 (2018).